8-5-2014

Non-Destructive Evaluation and Maintenance of Thermal Barrier Coatings

Martin P. Hawron
University of Connecticut - Storrs, mphawron@gmail.com

Non-Destructive Evaluation and Maintenance of Thermal Barrier Coatings

Martin Per Hawron B.S.

B.S., Southern Arkansas University 2011

A Thesis

Submitted in Partial Fulfillment of the

Requirements for the Degree of

Master of Science

at the

University of Connecticut

2014

APPROVAL PAGE

Master of Science Thesis

Non-Destructive Evaluation and Maintenance of Thermal Barrier Coatings

Presented by:

Martin Per Hawron B.S.

Major Advisor:_____
Michael W. Renfro

Associate Advisor:_____
Eric H. Jordan

Associate Advisor:_____
Maury Gell

University of Connecticut

2014

Acknowledgements

Everywhere life has taken me, many have gone out of their way to help me along, and this university has been no exception. I am grateful to Mike Renfro for guiding my academic growth over the past two years, being an ever-approachable laser guru, and for convincing me to come to UConn in the first place. I am much indebted to Eric Jordan for the conversations in which he would communicate more knowledge about TBC's than you could look up in a week. Thanks to Maury Gell for bringing his extensive knowledge on the subject to my thesis committee. I would have been lost without Jerod's efforts in familiarizing me with the methodology and programming required for this work. To my lab-mates Kathryn, Chris, Marc and Stephen; Jason, George and Bikram: bouncing ideas off of you has been as useful as drinking with you has been, at times, necessary. I would like to thank Nick for his valuable assistance in developing software, as well as meticulous tinkering. Jonny is much appreciated for his contributions with POD and collection of LIBS references. Nirav deserves recognition as a veritable champion of IMS, and has been great to work with. My thanks go out to Tom Mealy for improving upon and fabricating a plethora of half-baked designs, Roger Ristau for allowing me to exploit his SEM expertise, to Jack Gromek for his instruction in XRD, and of course to Gary Lavigne for training and advice concerning the Ramascope. Finally, I would like to thank my family, who have been patient, supportive, and loving throughout the years I've been away.

This research was funded by the Rolls Royce Corporation.

Table of Contents

Table of Figures

Abstract

Thermal Barrier Coatings (TBC) composed of Yttria-stabilized Zirconia (YSZ) ceramic are widely employed in gas turbine engines to insulate nickel-based components from the extreme temperatures of the gas stream. Over the course of extensive operation, these coatings delaminate and eventually succumb to spallation failure. Photoluminescence Piezospectroscopy (PLPS) is employed as a non-destructive evaluation (NDE) technique for the predictive determination of the operational lifetime of these coating systems. A mobile analysis unit has been developed to provide remaining life analysis for EB-PVD applied TBCs of engine-run turbine blades. This technology includes a Laser-Induced Breakdown Spectroscopy (LIBS) capability utilized for precision removal of oxide formations on the coating surface.

Expansions to this technology were undertaken to explore its fuller potential, including a performance optimization of the LIBS and PLPS subroutines, and evaluated during field demonstrations. Mobile analysis capability removes the necessity of an off-site laboratory, but the savings in labor and time would compound quickly if *in-situ* measurements on a mounted engine were enabled. Ground work was laid for a borescope adaptation of the NDE technique, involving the integration of optical fiber components into the laser ablation and lifetime analysis processes. When coating systems reach the end of service life, removal of the topcoat becomes desirable, so that it can be replaced. A prospective laser-ablation TBC removal method was tested to acquire evidence concerning its utility for coated systems.

1 Introduction

Commercial airlines are continually searching for ways to improve the efficiency of the gas-turbine engines which power the aerial transportation industry. The modern gas-turbine engine is modeled as a Brayton Cycle, an open power cycle with constant-pressure combustion. As there exists a direct relationship between the quality of energy and temperature, the thermal efficiency of these power cycles is tied to the maximum turbine inlet temperature. To maximize operation temperature, ceramic coatings are applied to the metallic engine components which experience the most drastic temperatures, particularly components in the turbine section where the gas temperature may exceed the melting point of the superalloys typically employed. The single-crystal, nickel-based superalloy material used for engine components may operate safely in an environment of up to 1050 °C. (Pollock, 2006) Engine operation at high temperatures is facilitated by internal airfoil cooling channels which cool the nickel superalloy from within. Nevertheless, operation at temperatures higher than the maximum average temperature for nickel superalloys is ultimately allowed by the protective thermal resistance of ceramic coatings.

These coatings are known as Thermal Barrier Coatings (TBC's) and have high thermal resistance, capable of providing a thermal gradient of several hundred degrees Celsius. Eventually though, standard operation will cause the spallation failure of these TBC's as a result of thermal cycling. Spallation failure is caused by delamination of the TBC from the bond coat by uneven growth and rumpling of a developing oxide layer beneath the TBC (Wen, 2005). This growth occurs in heating and cooling cycles corresponding to engine operation and standby, respectively. The stepwise nature of the growth of this oxide layer, known as the Thermally Grown Oxide (TGO) leads to a description of coating lifespan in terms of thermal cycles. Current industry standard practices for evaluating the service duration of TBC-coated

components is to place a hard limit on the allowable number of thermal cycles. It is desirable to more accurately predict the failure of TBC's to minimize the wasteful, premature replacement of engine components while establishing a reliable and safe thermal cycling limit.

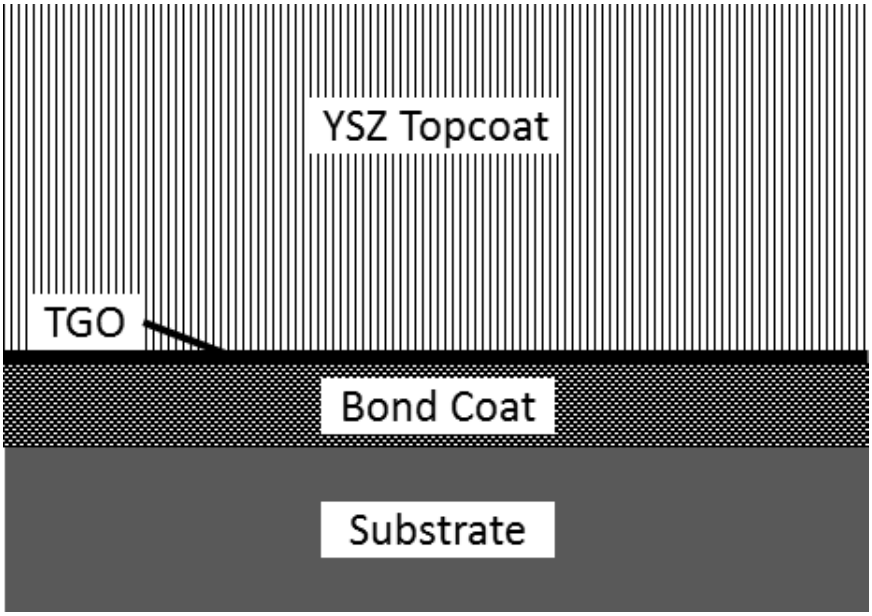

Figure 1: Schematic of cross section of thermal barrier coating system: The 7YSZ topcoat is applied by electron-beam physical vapor deposition onto a 40% platinum-substituted nickel-aluminide bond coat, which secures it to the nickel-based superalloy substrate. An aluminum oxide layer grows between the bond coat and topcoat with thermal cycling.

Because of the structural characteristics of TBC's applied via electron-beam physical vapor deposition (EB-PVD), diagnostic techniques are possible which can quantify the TBC's remaining life in such a way that testing does not negatively impact the coated components. An example of such a non-destructive evaluation technique (NDE) is photo-luminescence piezospectroscopy (PLPS) successfully demonstrated for use on EB-PVD TBC's (Christensen et al, 1996). By exciting trace Chromium ions in the TGO via a laser, it is possible to calculate the biaxial residual stress in the TGO via the frequency shift of emission spectral peaks from R-line

transitions of the trace Chromium. This residual stress is directly correlated to strength of the bond securing the TBC, and hence to the coating's remaining life (Clarke, 1997).

During the course of engine operation, deposits of metal oxides develop on the surface of engine components. These compounds are dominated by calcium oxide (CaO) magnesium oxide (MgO), aluminum oxide (Al_2O_3) and silica (SiO_2) and are collectively known as CMAS. This cocktail of oxides adheres to the TBC at high temperatures, forming structures of uneven thickness and heterogeneous composition. CMAS deposits can clog cooling holes and negatively impacting blade cooling by trapping thermal energy in the TBC which can contribute to TBC delamination (Chen, 2006). In addition to adverse effects to TBC integrity, CMAS obstructs the PLPS technique for TBC life analysis. The interference is twofold: CMAS physically blocks the excitation laser from reaching the TGO, and it also provides a false signal, due to its alumina component. To effectively implement the NDE for TBC life analysis, the CMAS must be cleared from any areas to be probed.

To address the interference from CMAS, a pulsed Nd:YAG laser is used to ablate away the offending contaminants from the TBC using a technique termed Laser-Induced Breakdown Spectroscopy (LIBS). The laser ablation is complemented with a real-time analysis of emission spectra which can pinpoint the interface between TBC and CMAS, preventing any undesirable damage to the TBC (Majewski, et al., 2011). This is made possible by a reference spectrum of pure a TBC sample, which is cross-correlated with the spectrum obtained per laser pulse. A discriminating threshold signals the completion of CMAS ablation, for which the overshoot damage has been shown to affect less than one micron of the TBC. With successful contaminant removal, the TGO stress is readily obtained by PLPS measurements (Majewski, et al., 2012).

To maximize the advantage of the NDE application, a mobile unit capable of delivering the full diagnostic procedure to engines in the field has been developed (Lake, 2012). The unit houses all the necessary equipment to carry out the CMAS removal and PLPS measurement, including compact, rugged lasers and instruments. A comprehensive collection of custom software written in LabVIEW coordinates and calibrates the system hardware. The stress measurement routine itself is automated, from CMAS cleaning to remaining lifetime prediction. As part of the work presented in this thesis, the mobile unit has been successfully put into service at an engine testing and maintenance facility, performing stress measurements and remaining life analysis on engine-run turbine blades.

The advantage of the mobile unit lies largely in the elimination of lengthy lead times for transport of components for testing to and from a third-party laboratory. The labor and cost for transportation is greatly reduced, along with the concern for security involved with transport. To compound upon the benefits of this technology, an additional and significantly advantageous development would remove the necessity of disassembling the engine for turbine blade analysis, an extremely costly and lengthy process. This modification involves the implementation of fiber optics for the LIBS and PLPS routines. By combining fiber optic cables for both processes into a borescope device, it would be possible to probe within the fully mounted engine to assess the general health of turbine blades and stator vanes in their respective stages. To this end, developments have been made for integrating fiber optics into the existing technology as described in this thesis.

In addition to the optical diagnostic NDE application, the existing mobile device has the potential to provide CMAS removal and even TBC removal capabilities for smaller turbine blades. Laser ablation is employed to remove CMAS from a large area of the TBC to extend its

service life and prevent accelerated damage from obstructed cooling holes. Proper Orthogonal Decomposition (POD) modes created from species reference spectra enable a threshold signal for ablation completion that is robust and versatile. As described in this thesis, this POD technique has been put into practice to remove relatively large areas of CMAS from the TBC-coated blades. In addition, by identifying reference spectra of species beneath the TBC, it is possible to utilize the same laser ablation to remove the TBC entirely from the substrate when it has reached the end of its service life.

This thesis describes the advancements made to the optical diagnostic NDE, including proposed extensions of the technology into other applications. A summary of the results of the mobile analysis unit's operation at a maintenance facility is provided in context of the performance before and after system improvements. Background information for the LIBS and PLPS procedures, as well as laser ablation and proper orthogonal decomposition is given as pertains to the NDE technology. Demonstration of the most recent successful developments follows by delineating the effects of the more promising aspects and projecting immediate steps for future venues of exploration.

2 Background

2.1 Thermal Barrier Coatings

Thermal barrier coatings are protective layers applied to materials which will suffer exposure to extreme temperatures. This is especially applicable in gas-turbine engines where the working fluid reaches temperatures of over 1500 °C. The very low thermal conductivity of ceramic thermal barrier coatings, e.g. 2.12 W/mK for YSZ (Vaßen, 2010), can provide a temperature drop of several hundred degrees Celcius. This thermal resistance facilitates much higher operating temperatures and the associated rise in engine efficiency desired in a constantly improving field. Fully functional TBC systems have finite operational lifetimes, often expressed as a function of thermal cycles. These thermal cycles, corresponding to the heating of the engine during full load and subsequent cooling , contribute to the roughening of the bondcoat/TGO interface which eventually causes spallation failure of the TBC (Zhao, et al., 2006)

2.2.1 TBC Composition and Properties

TBC systems are composed of four layers, as shown in Fig. 1. First is the substrate material; in the case of the turbine blades studied in this thesis, the substrate is a single-crystal nickel superalloy. Second is a nickel-aluminide bond coat, necessary for topcoat adhesion. Third, a layer of aluminum oxide, termed the Thermally Grown Oxide (TGO), develops over time between the bond coat and topcoat as a result of oxidation of aluminum in the bond coat. Fourth, the topcoat synthesized from a Yttria-Stabilized Zirconia (YSZ) powder with an optimumYttria

dopant concentration of 6 to 8% (Lu 2013). The TBC is usually several hundred microns thick, depending on the structural type and the needs of the application.

Many ceramic compounds are utilized to develop TBC topcoats with low thermal conductivity and high thermal stability, such as pyroclores, hexaaluminates, and perovskites. (Vaßen 2010). However, the industry standard for TBC material is 7% Yttria-stabilized Zirconia, or 7YSZ. In order to form TBC's, the YSZ ceramic powder is typically applied to substrates by one of two methods: Atmospheric Plasma Spraying (APS), or Electron-Beam Physical Vapor-Deposition (EB-PVD). The latter method out-performs the former in terms of longevity, making EB-PVD style TBCs the focus for non-destructive investigation of coating lifetime in extreme-temperature applications (Padture 2002).

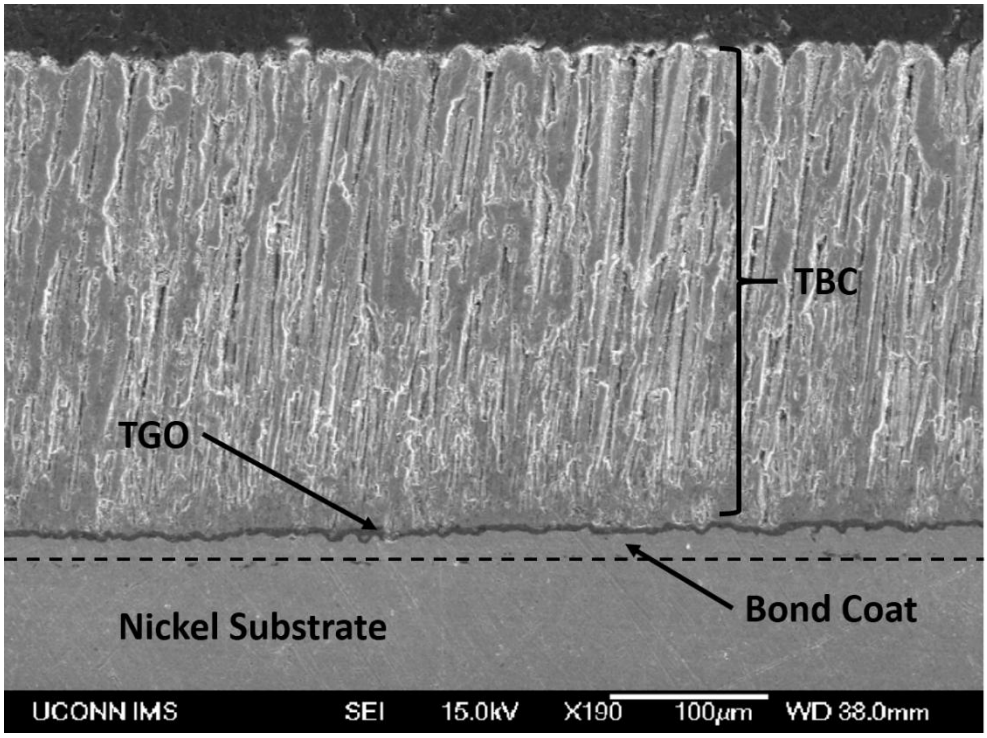

Figure 2: SEM micrograph of engine- run turbine vane cross-section illustrating the metallic and ceramic layers of a coating system with EB-PVD applied TBC. The bond coat is outlined by the sharp line of the TGO above, and a line of pores below.

EB-PVD application of YSZ powder yields a TBC with distinct, columnar microstructures extending from the bond coat to the topcoat surface, as can be seen in the cross section of Fig. 2. The arrangment of these columns has the advantage of improving the TBC's thermal resistance as a result of increased porosity due to void fraction between columns. It also lends to the TBC the properties of a waveguide for visible light, a characteristic well exploited by diagnostic techniques such as photo-luminescence piezospectroscopy (Zhao, 2007).

The typical bond coat is a nickel-aluminide (NiAl) compound, and promotes adhesion of the TBC to the superalloy substrate, which the bond coat additionally protects from oxidation. Application methods for bond coats include APS, Low-Pressure Plasma Spray (LPPS) and High Velocity Oxygen Fuel (HVOF). The blades studied herein utilize an APS applied, 40% platinum-substituted nickel-aluminide, or (Ni,Pt)Al, bond coat. The bond coat material, as well as the application method and any accompanying treatment, such as grit blasting (Xie, 2003), has an effect on the longevity of the TBC in the coating system. The bond coat and its imperfections determine not only the maximum topcoat lifetime, but also the failure mode (Wen 2005).

The bond coat acts as an aluminum reservior for the TGO which develops as oxygen diffuses through the TBC at high temperature and oxidizes the aluminum in the bond coat, forming an aluminum scale (Bose, 2007). TGO is aluminum oxide Al_2O_3, mostly in the alpha phase. During thermal cycling, meta-stable theta-phase alumina forms, and then transitions to alpha-phase alumina as the TGO cools to ambient temperature (Wen, 2006). The interdiffusion zone where penetrating oxygen ions, and to a lesser extent, outwardly diffusing aluminum ions interact defines the boundaries of the TGO. This layer reaches a thickness of a few microns, limited by the permissivity of TGO to oxygen. A maximum thickness of ten microns or less is reached only upon topcoat spallation (Bose, 2007).

2.1.2 TBC Spallation Causes and Prediction

Topcoat spallation is a direct result of the strain energy stored in the TGO. Imperfections in the bond coat cause the TGO to initially develop a oscillatory profile, with crests and troughs that experience compressive and tensile stresses, respectively (Sniezewski, 2008). With thermal cycling, the mismatch in thermal conductivity between the TBC, TGO and bondcoat cause the direction of the stresses in the TGO crests and troughs to reverse. This process is known as roughening, buckling, ratcheting or rumpling, and is responsible for instigating micro-cracks in the TBC (Wen, 2006) As TGO rumpling becomes more pronounced, the micro-cracks propogate throughout the TBC, until eventually large areas of TBC delaminate from the bond coat in a process known as spallation. It is known that spallation is the predominant mode of EB-PVD TBC failure (Zhang & Chen, 2011), which would place high priority on predicting TBC spallation and identifying the corresponding indicators of delamination approach.

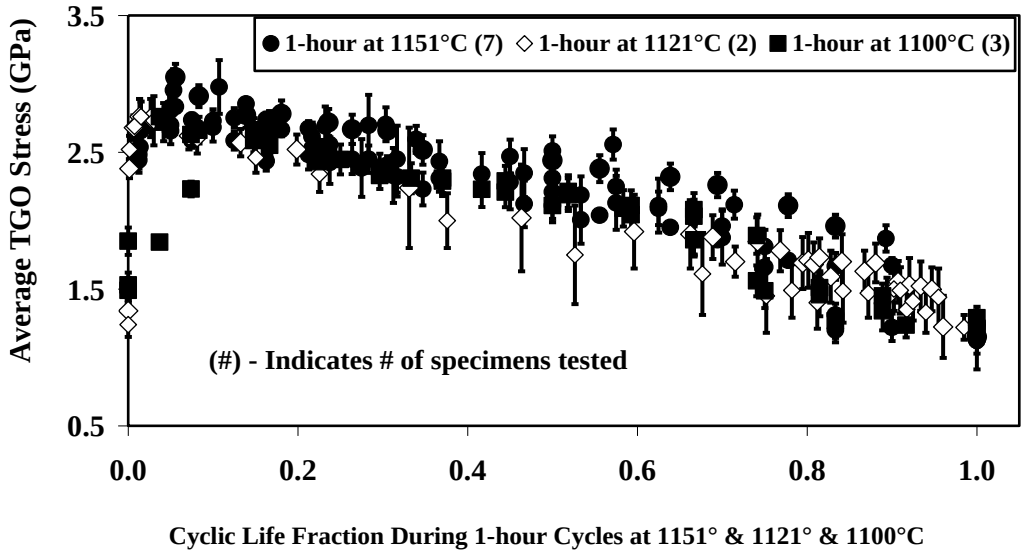

Figure 3: Trend-line for biaxial stress measured in TGO volume as a function of life-fraction, normalized to spallation failure. The trend-line and figure are provided by Mei Wen (2006)

In a previous experiment shown in Fig. 3, a correlation was found between the lifetime of the TBC with the biaxial stress measured in the TGO (Wen, 2006). Stress measurements were taken on TBC-coated button samples of single-crystal nickel superalloy over the course of repetitive thermal cycling in a furnace. The thermal cycling was performed at several temperatures which approximate the ambient conditions for the gas-turbine engines where such TBC's would be employed. The duration and temperature ramp were designed to simulate typical thermal loading that would result from routine engine operation. Coating life-fraction was normalized to 1 at the point of spallation. The trendline obtained has been found to be valid for EB-PVD applied TBC with an APS (Ni,Pt)Al bond coat. Given these findings, it is possible to determine the current life-fraction of a given TBC-coated specimen, and apply the stress-life fraction curve to predict failure.

2.2 Remaining Life Non-Destructive Evaluation Method

Non-destructive evaluation (NDE) techniques for coating health assessment and failure prediction aim to collect information about the subject component without altering its condition or inflicting any significant damage. Several techniques, such as Mid-Infrared Reflectance, Thermal Wave Imaging, and Photo-Luminescence Piezospectroscopy, are capable of analysing TBC coatings on blades which can then be returned into service upon passing inspection. Of these, PLPS is particularly promising, due to the waveguide property of EB-PVD style TBC for visible light (Gell, 2004). A novel NDE technology has been developed (Majewski, Lake) which utilizes local PLPS measurements to predict spallation failure of EB-PVD style TBC systems. Coating remaining life analysis can be performed on TBC-coated components such as turbine blades and stator vanes utilizing PLPS coupled with a stress-life regression correlation.

2.2.1 Photo-Luminescence Piezospectroscopy

PLPS is a visible-domain optical technique wherein the residual stress in α-Al_2O_3 can be determined utilizing the fluoresence spectra from trace Chromium, as shown in Fig. 4. Within every sample of naturally-occurring α-Al_2O_3, there is the unavoidable presence of Cr^{3+} ions, which replace the Al^{3+} ions in the crystal lattice structure. The R-line transition emission spectra of Chromia are shifted to higher frequency by increased compressive stress induced from the neighboring lattice elements. The R1 and R2 transitions are well suited for displaying this effect, and since the R2 peak shifts linearly in frequency with respect to compressive stress, it is the object of PLPS stress measurements (Zhao, 2006) . Since the alumina in the TGO of TBC systems is primarily α-Al_2O_3, frequency shift measurements of the R2 Chromium transition peak can be used to determine TGO stress.

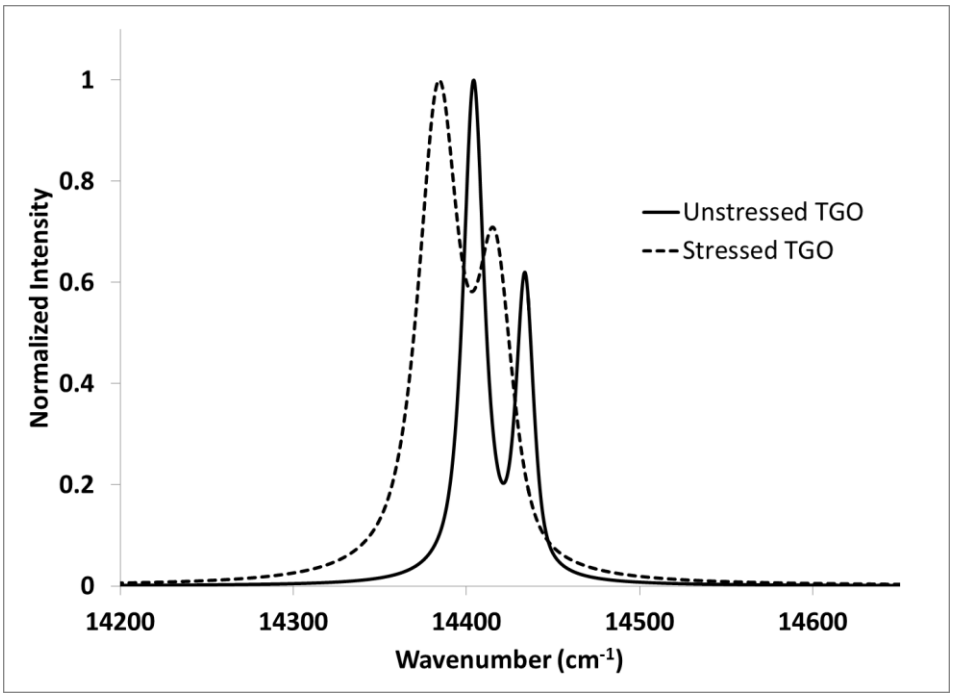

Figure 4: Laser-stimulated emission of Chromium ions from two sources: The first is a thermally cycled turbine blade with EB-PVD coating of 7YSZ, and the second is a disk of α-Al203, used to determine the zero-stress fluorescence signal. The frequency shift between the R2 peaks (Shorter peak on the right) of these two waveforms is used to calculate the TGO stress.

Neglecting the effects of temperature and chromium concentration in the TGO, the frequency shift of R2 transition fluorescence is modeled as a linear function of stress over an experimentally determined domain. The frequency shift of Chromium R-line transitions from TGO measurements is determined by comparing the specimen's fluorescence signal to that of an unstressed reference disc of pure α-Al_2O_3. To obtain the peak locations, the collected spectral signal is deconvoluted into two separate peaks, which can be characterized using a specialized fitting algorithm (Selcuk, 2002). The frequency shift $\Delta\nu$ is the differential between the fitted R2 peak location and of the unstressed reference, which displays an R2 peak location at 14,433 cm^{-1}. To control against temperature effects on frequency shift, the zero-stress measurement is taken under the same conditions as any TGO measurements in a controlled environment.

In measurements on specimens with EB-PVD applied topcoats, the TGO is excited by laser light of a higher energy than its R1 and R2 peak, around 694 nm. The excitation laser is focused into a small spot on the TBC surface, and thus channeled through its depth to excite a small volume of the TGO. The fluorescence emission from the TGO probe volume will be partially captured by the same waveguide effect, and returned to a confocal collection apparatus. A dichroic beamsplitter separates back-reflected laser light from fluorescence signal, and couples to a spectrometer for signal analysis. The quality and intensity of the PLPS signal depends partially on the thickness of the TGO, and partially on surface conditions of the topcoat. The experimental setup is described in Fig. 5.

Spreading of the laser in the TBC due to the index of refraction differential between YSZ and air occupying the void fraction is complemented by interface effects and the influence of

irregularities in the column microstructure, which are visible in the micrograph in Fig. 6, to cause the probe volume to be larger than the initial beam focus might suggest (Atkinson, 2000). Because of the increased size in probe volume, it is very possible that a measurement will encompass a portion of TGO which contains several regions of discrete topologies, such as the vicinity of a microcrack. In these situations, the collected waveform will suffer from the convolution of multiple sets of R1 and R2 peaks, obfuscating the R2 location, and hindering the calculation of TGO stress. To handle waveforms which are likely the aggregation of several sets of peaks, a bimodal deconvolution scheme is employed to decompose the waveform into the most probable R1 and R2 locations (Wen, 2006).

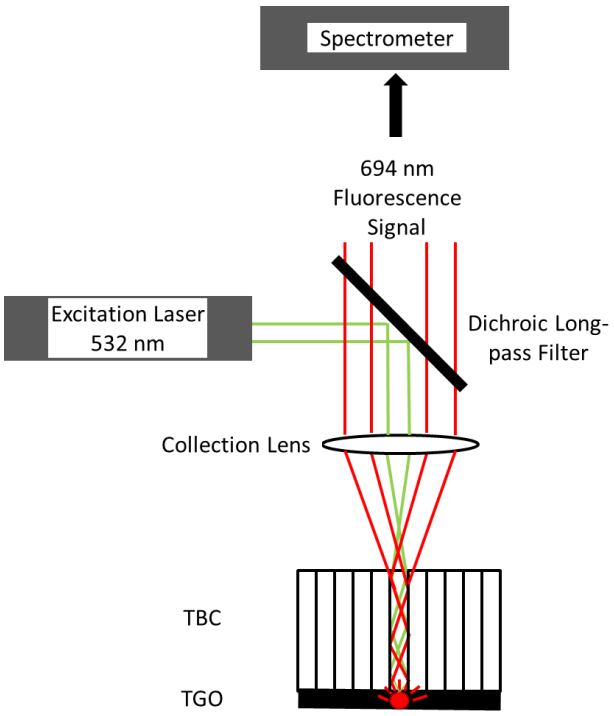

Figure 5: Schematic for typical PLPS experimental setup used in this study. The long-pass filter has a cutoff wavelength of 685 nm, and the collection lens is a microscope objective of 10x or 20x magnification.

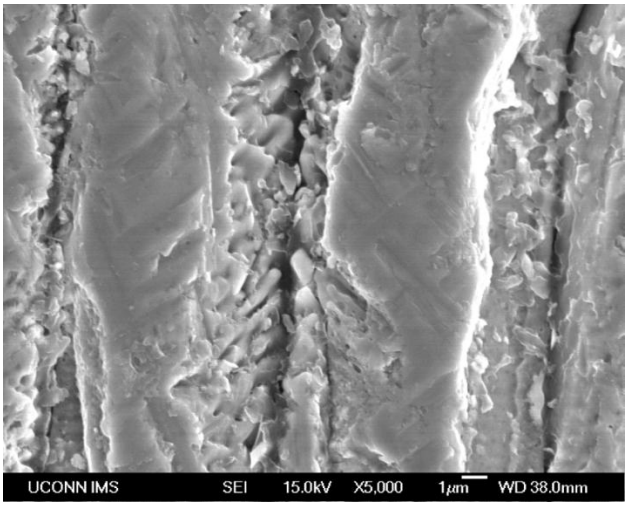

Figure 6: SEM micrograph highlighting irregularities in the columnar microstructures in EB-PVD topcoats. Protruding features along the micro-columns create variability in the waveguide efficiency of the TBC for visible light.

2.2.2 CMAS and Interference with TBC Life Analysis

During the course of standard engine operation, which involves flying through a range of atmospheric environments, an accumulation of metal oxides occurs on the surface of engine components, including the TBC. These compounds, mostly Calcium Oxide, Magnesia, Alumina and Silica are known collectively as CMAS, a term for any combination of these species found naturally as a result of trace elements in the atmosphere. At high temperature, these species will melt on the TBC surface and congeal into irregular structures, as shown in Fig. 7. CMAS deposits can be damaging to the engine components they attatch to, clogging cooling holes and channels, such as found in helicopters operating in desert conditions (Braue, 2009). CMAS can also infiltrate the TBC columnar structure at high temperatures, building thermal stress and inducing thermal shock (Kramer, et al., 2006). It has been shown to cause TBC delamination via development of strong tensile stresses upon its cooling on a TBC surface (Mercer, et. al. 2005).

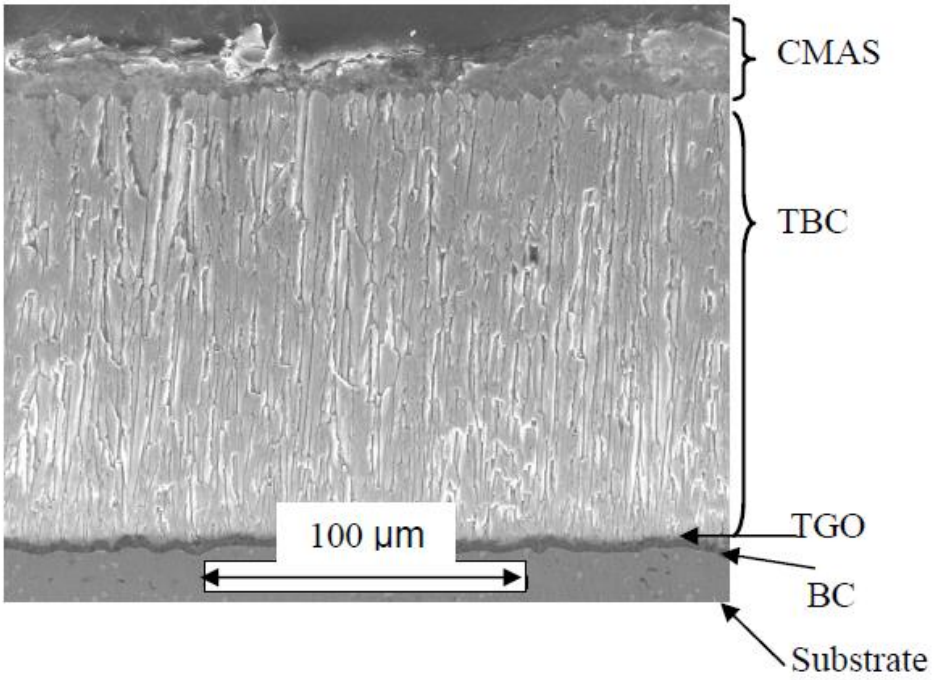

Figure 7: SEM micrograph of a TBC system cross-section showing the layers from superalloy substrate to YSZ topcoat. The top layer is a deposition of CMAS. The thickness of the contaminant layer varies significantly. Photo credit to Majewski.

Another complication caused by CMAS deposits is the interference with piezospectroscopic measurements. CMAS is not transparent to visible light, hence fluorescence from the excited TGO, and the excitation laser are both impeded. In addition, the alumina constituent in typical CMAS samples is alpha-phase, which will contain Cr^{3+} ions in the proper configuration to provide its own R-line fluorescence signal, similar to that originating from the TGO. Because the CMAS is a partially free surface, the out-of-plane stress will be lower than a fully intact TGO layer. If a PLPS measurement is taken over an area with CMAS contamination, the average stress will be shifted towards around 1 GPa, compared to the typical TGO stress range of 1.5 to 3.5 GPa for operational TBCs. This interference causes a bimodal waveform if the intensity of signal from CMAS alumina is comparable to that from the TGO.

Successful PLPS measurements are dependent on the effective removal of CMAS. The alumina which provides a false signal is in a zero-stress state, and the shifted R2 peak location may be selected against, utilizing bimodal deconvolution of fluorescence waveforms. However, since the composition of CMAS is unpredictable, the magnitude of false PLPS signal cannot be accounted for *a priori*. Laser ablation has been shown to be useful in cleaning contaminants from surfaces whose structural integrity must remain intact. The variable composition and thickness of CMAS samples, even across a small area, necessitates an adaptive ablation scheme. To address the interference posed to the measurement technique by CMAS, Laser-Induced Breakdown Spectroscopy (LIBS) is performed to remove the offending oxide formations via laser ablation.

2.2.3 Laser-Induced Breakdown Spectroscopy

LIBS is an optical technique by which qualitative and quantitative information on the chemical composition of a sample is obtained through the destructive instigation of stimulated atomic emission. The fundamental process underlying LIBS is laser ablation, by which small amounts of material are vaporized and ejected from a target surface. It is particularly well-suited to analysis of solid samples of transition and rare-earth metals, as emphasized by its application for soil sample chemical analysis (Barbini, et al., 2000). In addition, the very precise laser ablation involved allows for selective removal of contaminants from a substrate surface which must be preserved, such as artwork (Lentjes, 2005). This is also pertinent for cleaning of archaelogical finds where more invasive methods are not viable (Anglos, 2001). The inclusion of LIBS as a component of this NDE technology facilitates diagnosis of engine-run components.

LIBS requires a high-intensity pulse of laser energy greater than the breakdown energy for the target molecules (Pasquini, 2007) causing an avalanche ionization of surrounding

molecules. A plasma is initiated by the intense energy these ionized molecules experience from the focused laser pulse. Absorption via inverse Bremmstrahlung of the laser pulse by free electrons energizes the plasma, and feeds its growth over several nanoseconds. During this period, the constituent molecules of the target material dissociate as the plasma's free electrons emit a continous background of Bremmstrahlung radiation. At the end of the laser pulse, the plasma cools and the atoms and molecules recombine with the free electrons in the plasma, emmitting atomic and molecular spectra with discrete spectral lines. It is from the locations of these spectral lines that qualitative compositional information is extracted, by comparison to energy level charts, or to compiled emperical data. In addition, quantitative information may be drawn from the relative intensities of the atomic emission peaks.

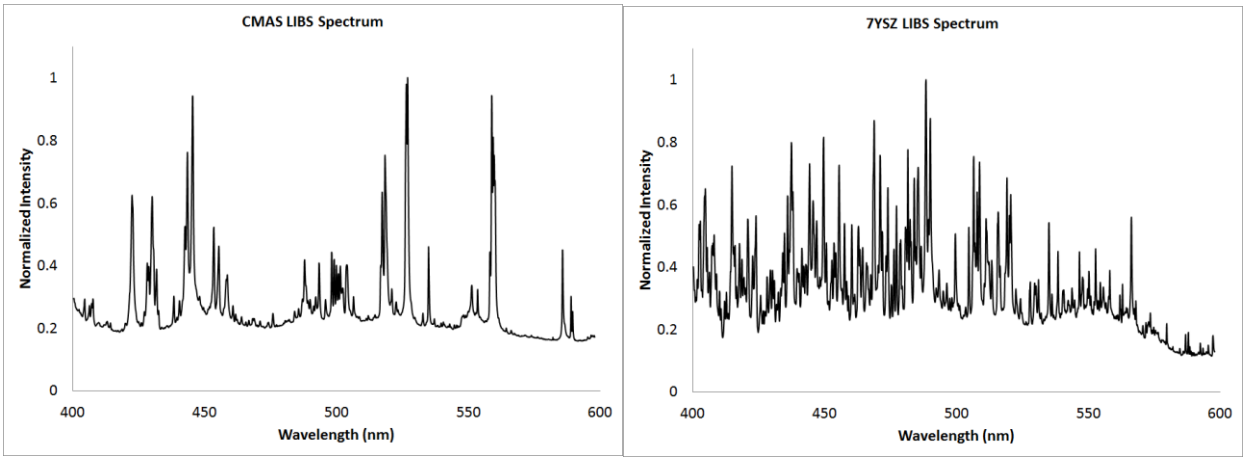

Figure 8: Typical LIBS spectra of CMAS and 7YSZ emission in the range of 400-600 nm using a 355 nm pulsed Nd:YAG laser. The CMAS spectrum (Left) is obtained from averaging samples from multiple engine-run blades.

To satisfy the non-destructive nature of this NDE technology, laser ablation must be controlled to a fine resolution which prevents any serious damage to the TBC when clearing an area of CMAS from an interrogation point. Reference LIBS spectra are kept for the species of interest, which for TBC cleaning involve CMAS and YSZ, as shown in Fig. 8. By comparing

LIBS spectra to an experimentally obtained reference spectrum of pure TBC, it is possible to track the progression of CMAS removal in real time, demonstrated in Fig. 9. A standard Pearson's cross-correlation serves as a metric of the relative composition of the ablated material, as a function of CMAS and YSZ. By placing a threshold on the maximum YSZ correlation value for the LIBS spectrum from a laser pulse, it is possible to cease ablation at near complete removal of CMAS, with TBC damage on the order of 1 micron. Damages of such magnitude have no bearing on the blade's structural integrity, and are considered negligible.

The stepwise calculation of covariance between a LIBS spectrum from a single ablation shot and that of a reference material requires that the same system be used for sample and reference. Then the two spectra can be compared as one-to-one functions in the pixel domain. The cross correlation coefficient between the LIBS spectrum and a reference species is given by:

$$r = \frac{\sum_i^n (S_i - \bar{S})(R_i - \bar{R})}{\sqrt{\sum_i^n (S_i - \bar{S})^2} \sqrt{\sum_i^n (R_i - \bar{R})^2}}$$

Where S denotes the sampled LIBS spectrum, and R is the reference LIBS spectrum. The number of pixels in the spectrometer is given by n. The result of CMAS ablation is a crater of exposed TBC, the diameter of which can be controlled to fit application requirements, typically between 0.4 mm and 0.8 mm for our system. An example of sucessfully executed CMAS removal is shown in Fig. 10, for an engine-run turbine blade with oxide deposits.

This CMAS removal LIBS system was first implemented by Majewski as a necessary measure for PLPS measurements on the real-life application to engine-run turbine blades. The CMAS ablation via pulsed laser was optimized for a 355 nm Lotis Tii Nd:YAG laser, and adaptive ablation control using spectra correlation was implemented. SEM micrographs and

Raman Spectroscopy were used to complement PLPS as a confirmation method for effective CMAS removal. Lake operationalized this technology by developing a mobile unit capable of automated lifetime analysis for engine-run TBC-coated components, refered to as TBC Remaining Life Analysis Technology, or TRLAT. This compact unit included an autofocus subroutine for PLPS measurements, as well as a "holefind" algorithm which would center fluorescence measurements to the LIBS crater. The system was equipped to provide rudimentary quantitative analysis of CMAS species.

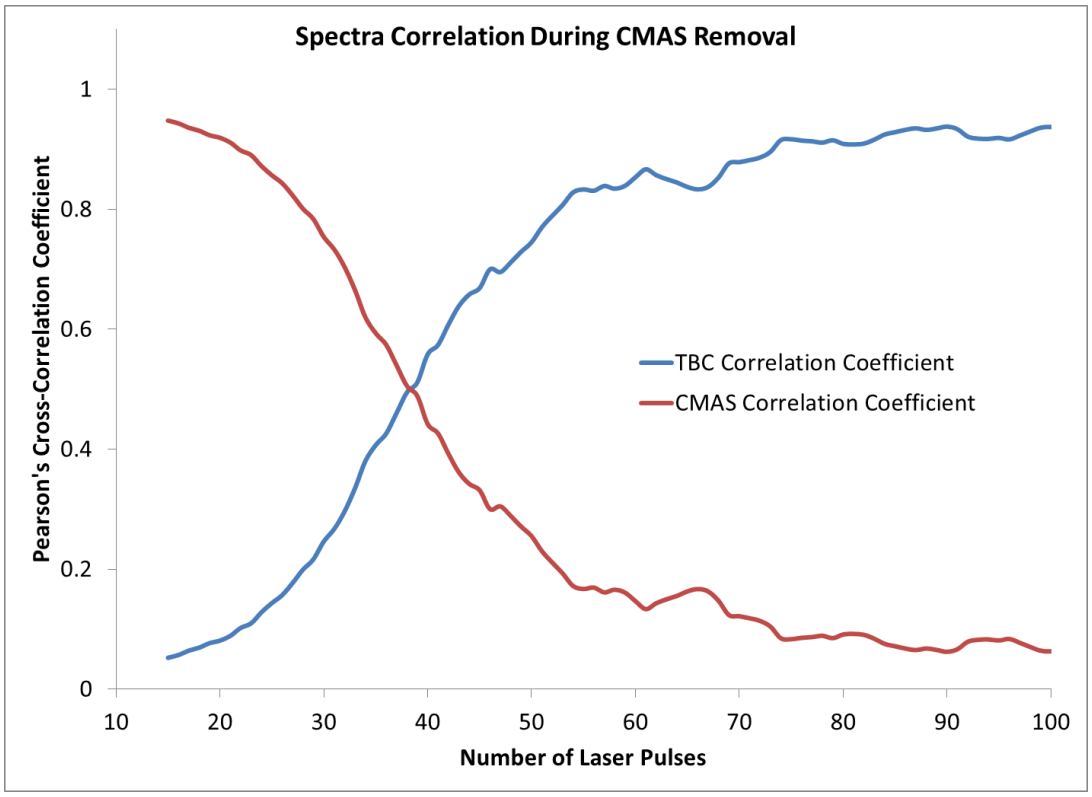

Figure 9: Example of the development of the Pearson's cross-correlation between the LIBS spectrum and the CMAS and YSZ reference spectra over the course of CMAS ablation from a single crater. After the intersection, or at a YSZ r-value of 0.5, the progression approximates a logarithmic curve.

Figure 10: Site for LIBS ablation of CMAS from TBC, clearing an interrogation area of 400-500 micron diameter. PLPS measurements taken from within the crater are unobstructed, with exception to those which fall upon the isolated remnants of CMAS, known as 'CMAS islands'. In a case such as this, these islands make a negligible impact on measurement fidelity.

The analysis technology proved robust for CMAS removal and stress measurements and the automated mobile unit met all requirements for user-friendliness and reliability. However, a new "ruggedized" Quantel Nd:YAG laser was purchased to reduce the overall system size and increase durability. The addition of this laser highlighted stability issues in the optics mount and incomplete CMAS removal. The dense structures of remnant CMAS, known affectionately as "islands" were too numerous and large to allow proper PLPS measurements. Part of this thesis describes measures taken to overcome these system instabilities after the laser upgrade, and alterations made to the PLPS measurement apparatus and procedure.

2.3 Expansion to Mobile NDE System

The potential of the LIBS-PLPS based NDE technology can be expanded by addressing additional exploitations of existing capabilities in terms of the maintenance demands in the aeronautics industry. Already in existence is a robust and automated mobile analysis unit capable of CMAS spot cleaning, and TBC lifetime analysis. This unit requires, however, that an engine be dismounted and disassembled before its components can be analysed. However, with a borescope apparatus for the mobile device, analysis could be performed on components within a mounted engine, effecting sizable savings in turnaround time and labor costs. A second venue for expansion adresses the end-of-life regime for TBC, where it is desireable to remove the spent TBC before complete failure occurs, preserving the underlying substrate and bond coating. The existing ability to precisely position a turbine blade for analysis can be converted into a continuous ablation of wide-area targets using the same translation stages. Complete removal of the TBC topcoat from engine components is contingent upon spectral recognition of the topcoat/bondcoat interface.

2.3.1 Borescope NDE Concept

In order to realize the borescope diagnostic probe concept, the processes of LIBS spot cleaning and PLPS measurements must be converted to fiber-based techniques. The more significant challenge of the two is achieving ablation through a fiber optic cable. To maximize power delivery while avoiding breakdown of the fiber/cladding interface, a large, single-core fiber is utilized to transmit the laser pulse energy necessary for LIBS. In addition to a fused silica fiber optic cable, other large-diameter waveguides have been demonstrated for power transmission, including fused silica rods, and hollow waveguides with dielectric coated inner walls. Emission spectra from the ablation target would be collected confocally through the same

waveguide, and extracted using a shortpass dichroic beamsplitter. Keeping instantaneous laser power density below the damage threshold of the waveguide material is crucial due to the nanosecond-order pulse duration.

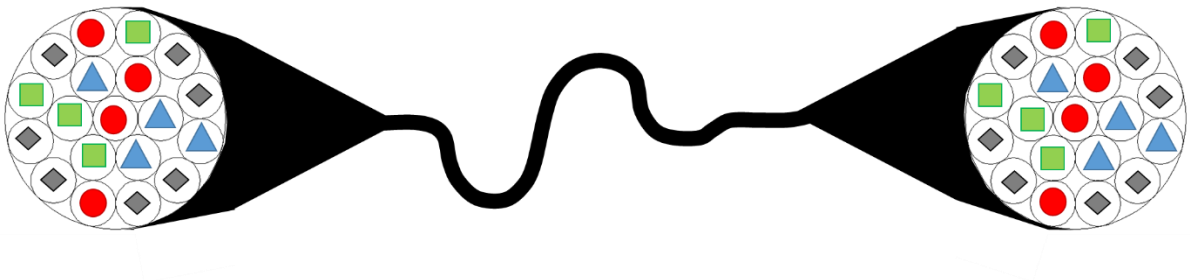

Figure 11: Illustration of the operation of a coherent fiber bundle. The light collected by each fiber on one end of the bundle is transmitted to a point on the distal end which retains its relative position among the surrounding fibers. In this manner, spatial information is preserved, a feature which is useful for imaging, or mapping spectral measurements.

The laser energy considerations for adapting PLPS into a fiber-based technique are not as extensive. Sufficient transmission for laser excitation of TGO through the TBC can be achieved easily with less than 200 mW, allowing for beam attenuation and distortion at TBC interface. The crucial feature of PLPS which must be preserved is the averaging of multiple stress values taken over the span of a small interrogation area. To achieve this, a coherent fiber bundle, described in Fig. 11, is employed for simultaneous excitation and signal capturing. Translating the laser focus across the proximal bundle face causes a corresponding spatial shift in the excitation point on the target plane. The diameter of the target area is proportionate to the bundle diameter, which can be manipulated to fill but not exceed the bounds of a LIBS crater. Fluorescence signal is collected simultaneously from the entire bundle, and collected via longpass beamsplitter.

2.3.2 Laser Ablation for TBC Removal

When the end of service life is reached for a TBC system on a given part, it is desirable to remove the topcoat without damaging the underlying superalloy, in order to apply a fresh coat and return the component into service. Laser ablation of TBC is proposed as an alternative to chemical TBC removal, which carries the disadvantage of requiring a re-application of the bond coat. In theory, laser ablation utilized for TBC stripping could eliminate the necessity of bond coat re-application by fine depth control. Since TBC depth is non-uniform across the surface of a blade or vane, the laser ablation scheme must be adaptive. If an interface between TBC and bond coat can be successfully located in real-time via analysis of LIBS spectra, it would be possible to entirely remove the TBC without incurring bond coat damage. Recognition of the TBC-bond coat interface is achieved through orthogonalizing reference spectra for both species, allowing a clearer distinction in the spectral contribution each makes to LIBS signal.

2.4 Optical Fiber Components for NDE Borescope Device

The development of a borescope device adaptation for the mobile NDE unit is made possible through the use of optical fibers and fiber optic bundles. Because of the sensitivity of the accuracy of both the PLPS and LIBS techniques used in this application to signal intensity, multi-mode fibers are preferred for their maximum light-capturing properties. In cases wherein there are relatively low requirements for time-resolution and optical path is short with respect to the fiber diameter, modal dispersion typical of multimode fibers is not a concern. Fused silica as a waveguide material is necessary for UV transmission, as found in silica-cladded optical fibers or fused silica tubes and rods. The high damage threshold of fused silica makes it suitable for applications which experience high laser intensity, such as from a focused, short-pulsed laser.

2.4.1 Coherent Fiber Bundles for LIF Scanning

Spatial coherence in a fiber bundle is a property which denotes the preservation of relative positioning for every optical fiber in the bundle. This feature is important to imaging applications where a pixel-by-pixel representation of the object image must be replicated accurately. Step index fibers of diameter ranging from several microns to hundreds of microns are arranged in tight formations to maximize the packing efficiency of the bundle, and thus its resolution. Coherent bundles are widely used in medical imaging applications, where high-resolution images of internal tissues and organs are difficult to obtain. Applications such as fluorescence microendoscopy (Cha, et al. 2012), optical coherence tomography, infrared thermal imaging (Matsuura, 2010), endocytoscopy (Hughes, 2013), and even anti-Stokes Raman scattering microscopy (Gao, et al., 2006) illustrate the diverse range of exploitations for spatially coherent fiber bundles.

2.4.2 Large-Core Optical Waveguides for Pulsed UV Laser

Optical fibers for high power transmission are in demand for various cutting and drilling applications where flexibility is desired, or where the environment forbids the use of standard equipment, as in certain welding scenarios. The higher harmonics of pulsed Nd:YAG lasers are popular options for a number of these applications, including medical applications, such as dental and ocular surgeries (Miller, 2011). Successful fiber power delivery is contingent on maximizing transmission while maintaining the exposure of laser intensity to the fiber face below its damage threshold. Large-core, silica-cladded fused silica optical fibers are a good candidate for a high-power flexible transmission device. Fused silica can also be drawn into rods or hollow tubes to create different styles of waveguides (Matsuura, 2007). In addition, bundles of

fibers and hollow fibers have been successfully employed in high power transmission (Yilmaz, 2006; Parry, et al., 2007).

Methods of maximizing transmission are largely case-dependent and the choice of material or configuration depends on the requirements of a given application. Waveguides which attenuate the transmitted beam over their length are known as lossy, or leaky waveguides (Ulrich & Prettl, 1972). Examples are waveguides dependent on the silica-air index step for multimode light propogation and waveguides coated with a doped dielectric coating. Beam attenuation is generally to be avoided for transmission applications, but if traditionally cladded waveguides such as the silica-silica fiber incurr damages due to the cladding dopant, the exchange of attenuation for damage offered by lossy waveguides may be acceptable. An argon gas buffer cell has been employed by Galt et al. to prevent optical breakdown of silica rods. Another method for maximizing transmission involves raising the damage threshold by surface treatment. Fine polishing using diamond, silicon-carbide or aluminum-oxide abrasives can greatly increase the transmission and durability of fiber faces (Kuhn, et al., 2000). Other methods involve terminations such as an air-gap copper ferrule for maximum heat dissipation, or a silica endcap to act as a protective buffer (Hélie 2010; Mohri et al., 2002).

2.5 Proper Orthogonal Decomposition for LIBS Spectra

The ability of the laser-induced breakdown drilling technique to adaptively adjust ablation depth is due to species identification. The real-time analysis of LIBS spectra as convolutions of multiple species' signals contributing to a collective waveform allows for the locating of interface regions. The premise for TBC removal via laser ablation is the same NDE premise for CMAS cleaning, and this depends on fine ablation control at interface regions. LIBS

spectra obtained from pure samples of the constituent species for a given interface provide references that determine the stop condition for ablation.

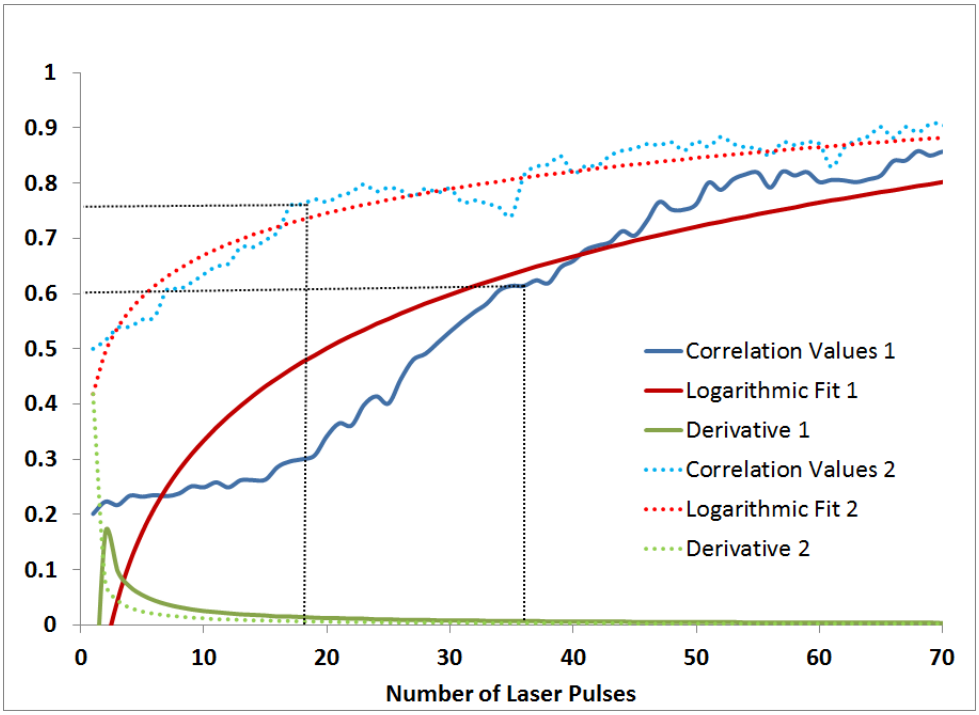

Figure 12: Comparison of performances of a logarithmic fitting for cross-correlation values between LIBS spectra and a reference spectrum. When the fitting begins at a value near 0.5, the agreement is good.

Previously, this has been done by comparing the progression of the Pearson's correlation coefficient of the LIBS spectra with the end condition reference spectrum (Majewski, Lake). A nonzero correlation between these reference spectra requires that an arbitrary tracking algorithm be employed, and while this algorithm is generally robust, it is offset by fluctuations in the signal intensity and initial composition. Via single-value decomposition methods, it is possible to develop independent reference modes which have a one-to-one correspondence to presence of their respective species. This offset error is highlighted in Fig. 12.

2.5.1 LIBS Spectra for Coating Species Discrimination

For each species in the thermal barrier coating system there exists a unique spectral profile from atomic and molecular emission spectra resulting from laser-induced breakdown. The transition peak locations and peak broadening, as well as the relative peak intensities are characteristic of each species, and contain information about its composition. In addition, the tail end of what Bremmstrahlung radiation background is not filtered out fully, compounded with system noise, creates a spectrum which is specific to the LIBS system, and also representative of each species observed using the system. Pure samples of the constituent species for the coating system are readily obtained in their solid crystalline states, and reference spectra are composed by performing LIBS acquisition on a large sample set of each compound to account for statistical variations. Some species share chemical composition, e.g. bond coat and substrate, and even without common chemistry, transition peaks from one species may also be present in another. For this reason, the LIBS reference spectra for coating species are partially dependent.

2.5.2 Proper Orthogonal Decomposition

Proper Orthogonal Decomposition (POD) is a data analysis technique which represents a high-dimensional data set with a low-dimensional solution set. It differs from the Legendre polynomial series or the Fourier series in that the POD solution matrix is composed of a set orthonormal functions (Chatterjee, 2000). One advantage of the POD method over the eigenvalue problem is that it is not necessary for POD that the data set form a square matrix, allowing a solution space with fewer elements than the size of the data set. Its applications are versatile, and is widely implemented in image processing, turbulent fluid flows, and microelectromechanical systems (Liang, et al., 2001) as well as structural vibration analysis (Han & Feeny, 2002).

POD is an adaptation of the single value decomposition problem. The finite solution set of real functions, known as Proper Orthogonal Modes (POM), are determined from the real factorization of a real (m x n) data set matrix A given by

$$A = U\Sigma V^T$$

Where U is the (n x n) matrix containing the left singular vectors, V is the (n x n) matrix containing the right singular vectors, which are the POMs, and Σ is an (m x m) matrix containing the singular values. These values σ_k, ordered in decreasing value along the diagonal of Σ, determine the significance of each POM in the solution matrix, indicating the corresponding levels of signal power (Feeny, 2002). The energy of a vector set A is equal to the sum of vector energies, defined by:

$$E(A) = \sum_{k=1}^{n} \sigma_k^2 \implies \chi_k = \frac{\sigma_k^2}{\sum_{k=1}^{n} \sigma_k^2} = \frac{E(\phi_k)}{E(A)}$$

Which means that for a given POM ϕ_k, the mode stoichiometry χ_k can be expressed as the mode energy normalized to the total vector set energy, allowing for modal behavior to be interpreted physically, as in the undampened systems analysed by Kerschen and Golinval.

For the laser ablation technique described in this thesis, the advantage to this method is twofold, when applied to the analysis of LIBS emission spectra. The first lies in the stability of mode energy progression in a dataset obtained from LIBS ablation through a target of evolving composition. This can improve stop criterion consistency in CMAS ablation, as per the example in Fig. 20, by permitting a static, physical threshold for mode contribution. The second pertains to low-signal situations where the cross-correlation value for one species may be suppressed by higher-contribution species. TBC removal, for example, is contingent on real-time bond coat

identification. Normalizing the mode energies for the orthogonal species vectors allows the identification of small changes in the chemical contribution of LIBS ejecta, which is crucial for recognizing a minute rise in the bond coat mode profile during a TBC removal drilling test.

3 Experimental Setup

The mobile NDE technology, shown schematically in Fig. 13, is a self-contained apparatus which has capabilities of performing local stress measurements on TBC-coated engine components as well as CMAS ablation for both spot measurements and large-area cleaning. It consists of two lasers: a pulsed Nd:YAG for ablation and a continuous diode laser for piezospectroscopy. Two combinations of stepper motors allow fine positioning of the target blade, as well as the collection optics, to a precision of within ten microns. Two compact fiber-coupled spectrometers process the spectral signals from LIBS and PLPS, respectively. A custom software developed in LabVIEW coordinates and monitors every aspect of the remaining lifetime analysis process, including stepper motors for positioning the target and sensors, timing the laser and spectrometer synchronization, and complete data analysis.

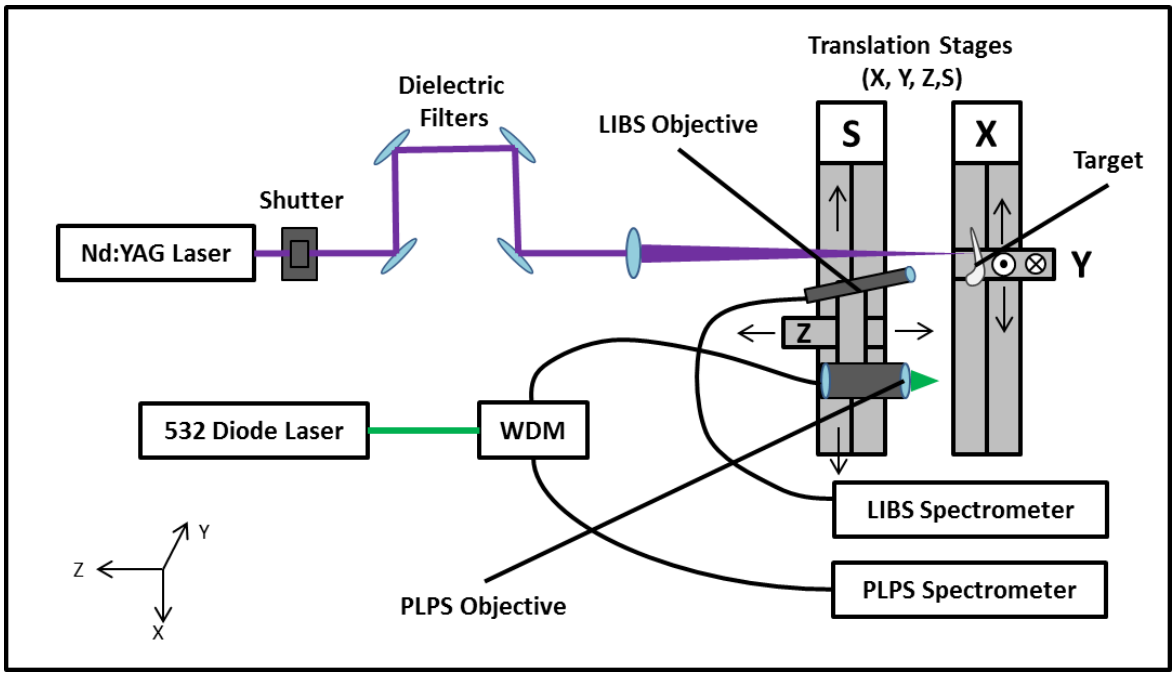

Figure 13: Diagram of LIBS/PLPS experimental setup. Stepper motors X and Y translate the target blade in a plane about the fixed ablation crater location, while the S and Z motors align the sensors' collection optics in the X and Y dimensions, respectively.

3.1 Laser Ablation and LIBS Setup

A Quantel ULTRA Nd:YAG laser frequency-tripled to 355 nm is employed for simultaneous ablation and spectroscopy. It delivers a 5.22 ns pulse with energy up to 33 mJ. A series of four broadband dielectric mirrors remove any residual 532 nm light from the YAG output beam. A 1.0 meter focal length plano-convex lens focuses the pulsed beam onto the ablation target which is mounted on a 2-D translation stage assembly, allowing movement in the X-Y plane normal to the incident focused laser beam. An 8 mm focal length collection lens is aligned to the ablation target by means of another 2-D translation stage assembly with movement in the X-Z plane. An Ocean Optics USB 2000+ spectrometer calibrated to the wavelength domain of 400 – 600 nm is fiber-coupled to the LIBS collection lens using a 600 μm core-diameter multimode step-index fiber optic patch cable. The spectrometer collection is triggered by the YAG laser's Q-Switch output TTL pulse, with integration time set to 50 ms, to match the YAG laser's output frequency of 20 Hz.

For proper laser ablation of CMAS, the power density of the laser pulse must be within a range such that the CMAS is completely removed, and the TBC remains undamaged. At lower pulse energies, the incident laser heating causes incomplete CMAS removal and re-deposition within the ablation crater (Majewski 2011). At higher pulse energies, the combined thermal shock and pressure wave from ablation causes fractures in the TBC structure. An optimized value of roughly 26.0 MW/mm^2 effects expedient CMAS removal without risk of damage to the underlying TBC. To achieve the proper power density, the laser is defocused such that the spot diameter is of a sufficient size for local stress measurements, and the laser pulse energy is

adjusted to the spot diameter. The spot diameter is modeled as a linear function of displacement from the focal lens as per thin lens calculations, as shown in Fig. 14.

As mentioned before, the typical spectral emission from laser-induced plasma displays a broad, continuous spectrum caused largely by Bremsstrahlung radiation followed by discrete peaks representing corresponding to the various electronic transitions of the ablation target's constituent atoms. Since the qualitative analysis that distinguishes between species is only possible through the discrete spectral lines, there must be a filter that separates the continuous spectrum from the discrete.

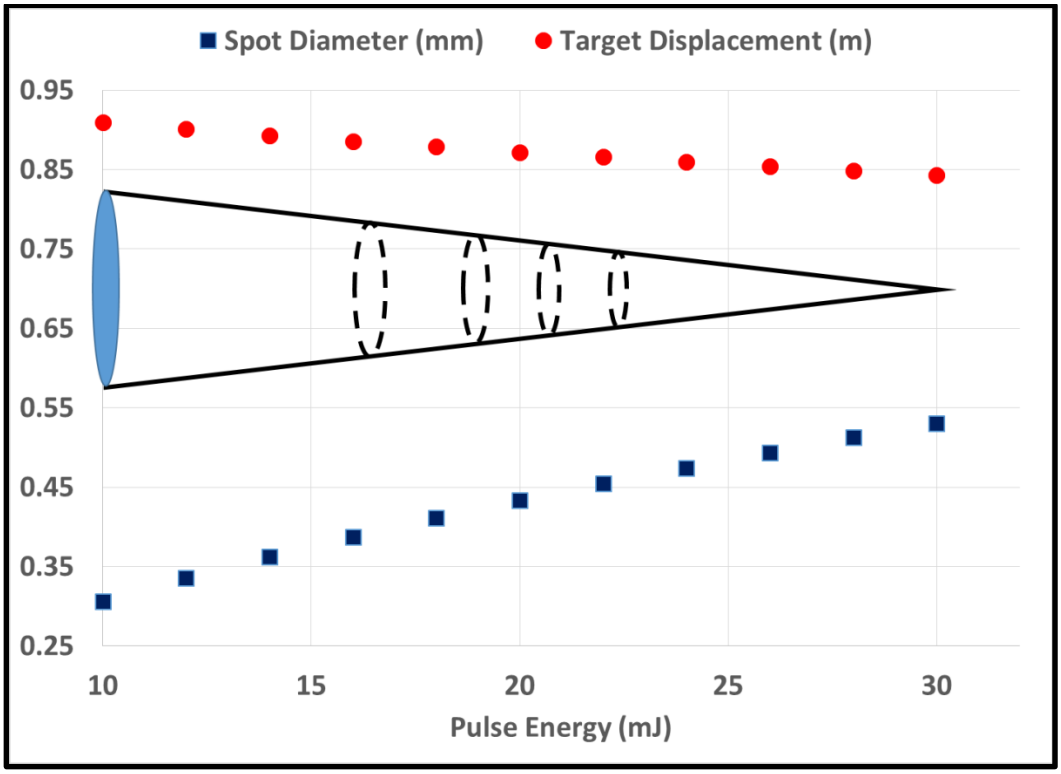

Figure 14: Relationship between pulse energy and spot diameter. For a given spot diameter, say 400 microns, the laser's pulse energy is adjusted (in this case to 17 mJ) such that the power density remains at 26.0 MW/mm^2. This necessitates that the focal lens be placed at a distance of roughly 0.9 meters from the target.

Two methods of achieving this separation are spatial and temporal filtration. Since there is already a temporal separation on the order of milliseconds between the two regimes of signal, by placing a delay on the spectrometer trigger, it is possible to discriminate towards the discrete spectra, while taking advantage of a confocal collection apparatus. Another method takes advantage of the geometry of the laser-induced plasma, wherein the light from de-excitation of the energized constituent ions originates. By aiming the focus of the collection optic at the plasma center, rather than the ablation crater itself, the same desired discrimination is achieved. In this experiment, the spatial filtering is implemented by means of an offset collection lens mounted at an angle relative to the incident beam such that the focus rests on the projected center of the laser-induced plasma.

For continuous ablation applications, the stepper motors that translate the target blade in the X-Y plane are coordinated through a custom software in LabVIEW to run continuously in a set pattern (Appendix). The velocity can be adjusted to match the ablation rate of the target material. For typical CMAS removal operation, the motor velocities are set to 0.7 mm/sec. In one example of a pattern for ablation, the y coordinate is held constant as the x position oscillates over prescribed bounds during constant laser ablation. Over-burn at the edges is accounted for by a mechanical shutter which engages when the target nears the edges of its range of motion.

3.2 PLPS Setup and Raman Spectroscopy

For the piezospectroscopy application, a 250 mW continuous diode laser provides the excitation frequency at 532 nm. This is channeled into a fiber-coupled wave-division multiplexer (WDM) equipped with a long-pass filter with a threshold of 685 nm. The output from the 600-micron diameter multimode fiber is collimated before focusing onto the interrogation point

through a long working-distance Miyutoyo objective lens. Due to the analogous relationship of the TBC columnar structure to a waveguide, it is necessary that both the excitation and collection beam paths are normal to the TBC surface, to maximize the transmission of light in the forward and reverse directions. Chromium fluorescence in the vicinity of 695 nm is collected and channeled through the WDM into a fiber-coupled Ocean Optics USB4000 spectrometer calibrated for 665-720 nm.

Previously, a 20x Olympus microscope objective was employed for focusing of excitation laser onto the target and signal collection. The resolution for PLPS was very fine using this objective, with a spot size on the order of a few microns. However, since the working distance of this objective is 1.5 mm, the curved geometry of the blade severely limits the area from which stress measurements can be taken. This causes problems with engine components other than 1st stage turbine blades, especially stator vanes. A long working-distance microscope objective replaced the 20x objective with intent to increase the versatility of the system. The 35 mm working distance allows for investigation of nearly the whole geometry for each engine component tested for this study.

The drawback of a longer working distance is reduced magnification of the lens combination, and hence a larger interrogation spot than with the shorter focal length objective. The point of concern is the resolving power of the PLPS system. Too large an interrogation volume might lead to integrating multiple stress values together, or disable the ability to distinguish between CMAS-originating signal and that from the TGO. To test the PLPS resolution with the larger spot size, a fluorescing turbine blade was coated with a material which is opaque to both the excitation frequency and the fluorescence frequency of the TGO. A spot of

roughly 0.6 mm diameter was cleared with laser ablation, and a fine PLPS scan, shown in Fig. 15, was taken to envelop the crater and local area.

The fluorescence measurement scan gave the estimated interrogation spot diameter as 180 microns. At this resolution, no adverse effects to stress measurement were observed, and the R-line waveforms for PLPS are of a high quality consistent with other objective lenses. Confounded signals resulting from CMAS island interference are easily recognized by their reduced figure of merit and frequently bimodal shape. TGO stress is usually minimally variant over the 180 micron diameter, meaning that local measurements with the larger laser spot are equally valid for TBC remaining life analysis.

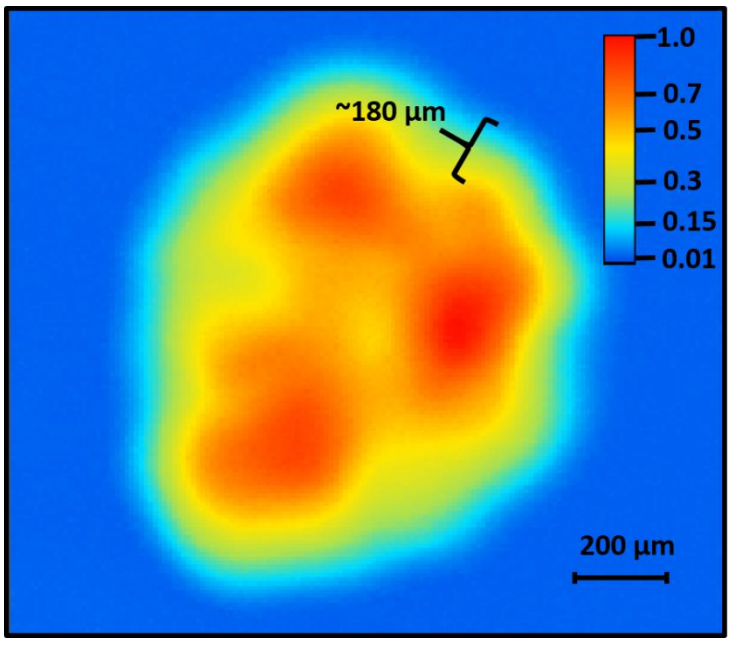

Figure 15 : Intensity map of a fine scan fluorescence test over a LIBS-ablated portion of a turbine blade coated in an opaque material. Signal normalized to 1 is displayed as the maximum intensity per measurement point. The gradient between the baseline opaque material signal and the quasi-steady center high signal illustrates the resolution of the objective lens.

To confirm PLPS measurements, a Richter Ramascope is used to excite the trace Chromia in the TGO in the same manner as our NDE technology. The Ramascope has an

excitation wavelength of 514 nm, which yields the same result expected from our 532 nm diode laser. A 50x objective gives a spot size of one micron, allowing for high-resolution scanning, as well as selective excitation of topological features, such as micro-cracks or CMAS islands.

3.3 Optical Fiber Implementation Setup

The two components of the NDE technology which allow remaining life analysis on CMAS-covered engine components, LIBS and PLPS, are being converted from a table-top scheme into a fiber-optic based apparatus. Ideally, a borescope-like device would house the optical cables for the pulsed Nd:YAG laser and the 532 nm diode laser and direct them onto an analysis site on a turbine blade or stator vane within the engine, without the need to disassemble the engine. A coherent fiber bundle would be utilized for PLPS, so that for a given location of the borescope, multiple measurement points could be taken to maintain statistical fidelity and to protect against contaminated data. In addition, a large-diameter single-core optical fiber with silica cladding is employed for transmitting the pulsed laser energy for CMAS ablation.

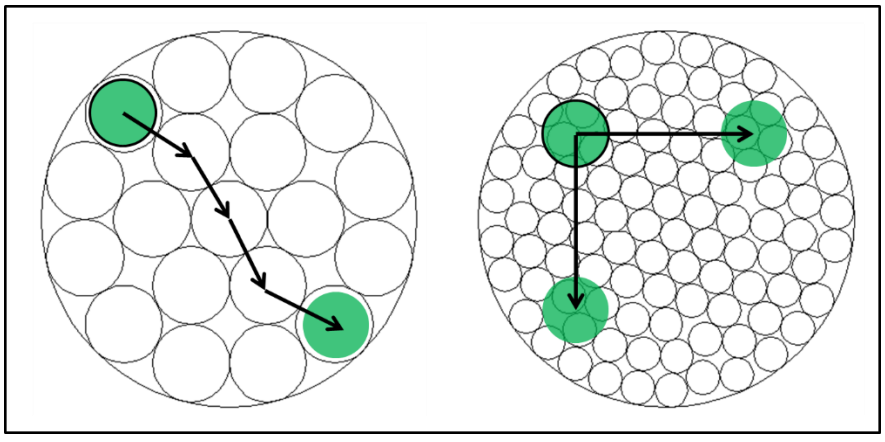

Figure 16: Diagram illustrating movement of the analysis spot over the diameter of the bundle in the 'discrete' and ‘continuous' cases. In the 19 fiber-bundle case, the analysis point travels one point at a time whereas the ‘continuous’ fiber bundle experiences nearly full freedom of motion across the bundle diameter, with a potential data point for any coordinate pair.

For PLPS scanning, two coherent fiber bundle types were chosen, as shown in Fig. 16, to explore the balance of signal collection and freedom of positioning for the interrogation point. One fiber bundle, composed of 19 fibers of 200 μm diameter, spans a circular area of 1.10 mm, the maximum for a SMA 905 style fiber cable termination. In this case, it is possible to channel the entire excitation laser beam into a single fiber, which divides the target area into 19 discrete interrogation points. For the other fiber bundle, with 30,000 pixels, movement of the interrogation point across the target area is nearly continuous over the 790 μm diameter bundle area.

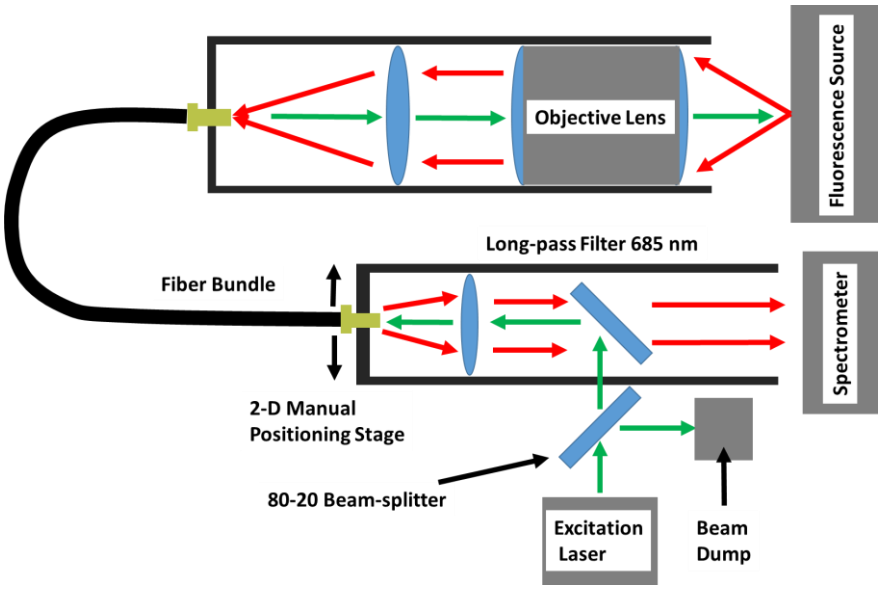

Figure 17: Schematic of the fiber-bundle based PLPS experimental setup: Translation of the fiber bundle determines which optical fiber carries the excitation laser, which displaces the excitation point by an amount proportionate to the magnification of the objective lens. A beam-splitter reduces the power such as to avoid damage to the silica fibers.

A 2-dimensional manual positioning stage is used to position the SMA-terminated fiber bundles near the focal point of a 35 mm plano-convex lens used to couple the collimated diode laser beam to the fiber bundle. Rails position the plane of the stage at the desired distance from the focal lens. The bundle's face is placed ahead of the focal plane such that the spot diameter is

within 200 microns. In the ‘discrete’ case this means a single fiber will carry the full energy of the excitation beam, and in the ‘continuous’ case, a few hundred pixels. To avoid damage to the fibers through light lost to the void fraction, the beam is reduced in power from 250 mW to 200 mW via an 80/20 beam-splitter. This reduction brings the power density below the damage threshold for the fiber optic bundle. For LIBS adaptation to fiber optic cables, a three-axis flexure stage is used to position the fiber or waveguide at the center of the focused pulsed laser beam. A plano-convex lens of 400 mm focal length is used to reduce the beam diameter to fill the energy carrying fiber. The fiber is placed after the focal plane in order to prevent a concentration of laser energy within the fiber, and thus avoid thermal shock to the fused silica. The fiber is held in place by an SMA connector for terminated patch cables, and for bare fibers, a strain-relief clamp is sufficient to provide reliable and stable positioning. The schematic for this setup is given in Fig. 17.

Several candidates for a waveguide for transmitting the high-intensity laser pulse are employed for the fiber LIBS application. A 1000 μm core-diameter fused silica fiber optic cable with silica cladding is SMA-terminated, and coupled using a SMA connector mounted to the flexure stage. This cable is equipped with copper ferrules to dissipate heat from coupling, as well as an air-gap connector to minimize the direct exposure of the silica core to laser energy. Other candidates include hollow silica tubes and solid fused silica rods. The hollow waveguides have inner diameters ranging from 0.5 mm to 2 mm, and outer diameters ranging from 1mm to 3 mm. Solid fused silica rods of 1mm and 2mm diameters are positioned on the flexure stage with a strain-relief clamp, in the same way that the hollow waveguides are mounted.

Short focal-length fused silica ball lenses focus the UV light from the distal end of the fiber onto the ablation target. This same lens configuration is used to capture the LIBS signal and

channel it back through the fiber or waveguide where a dichroic mirror separates the signal from back-reflected laser light and a 600 micron diameter multimode patch cable transmits the signal to a USB spectrometer. The ball lenses have a diameter of 2 mm and 0.5 mm, resulting in a fine demagnification, with some intrinsic signal loss. Other configurations of lens combinations are possible in order to increase signal retention while providing the necessary energy density.

4 Improvements to NDE System

The mobile LIBS-PLPS NDE instrument was tested at an engine overhaul facility (Standard Aero) in Maryville, TN during July 2012. Several targets for improvement were identified and have been implemented into the instrument, as described in this Chapter. First, jarring or vibration resulting from long-distance transportation of the mobile system resulted in inconsistency in the alignment configuration. For example, the supports for the UV mirrors would loosen, requiring meticulous realignment to consistently obtain accurate data. Since that visit, optical mounts have been stabilized, and once aligned a semi-permanent glue has been used to secure their orientations. This measure increased the reliability of the alignment system, including after extended transportation. The time for assembly, alignment and calibration of the mobile system after transportation can be reduced to 2 hours.

The second issue was the incomplete ablation of the target plane across the beam area. The beam profile with spatially-varying peaks and troughs as a function of radius rendered the final CMAS pattern on the target spot unacceptable for PLPS upon ceasing ablation. Efforts to address this problem are described subsequently in this chapter. The large CMAS islands remaining after ablation cause two sorts of PLPS errors: Bimodal deconvolution of the spectral waveform in cases wherein both exposed TBC and CMAS islands were encompassed within the

PLPS interrogation point, and entirely low stresses in the case that the entire interrogation point landed on a CMAS island. To address this topic, the beam profile and energy has been characterized by observing ablation performance over a range of operation parameters. Optimal values were chosen such that CMAS interference is reduced to a manageable level and the adverse effects of the somewhat sporadic YAG beam profile are minimized.

The third issue was that of inconsistent PLPS measurements, including drastically higher stress measurements. This issue may be related to the second, but some doubts remained as to the source. The average stress values for PLPS measurements taken from ablation craters were outside the domain for the Stress-Remaining life correlation currently employed, as shown in Fig. 3. Specifically, stress values in the vicinity of 3.5 GPa were measured alongside values as low as 1 GPa on the same blade. Several plausible sources of the variability of stress values were investiaged, including bimodal deconvolution of spectral waveform and the temperature-dependence of the frequency shift for R-line fluorescence of Cr^{3+} ions. A series of tests described in Section 4.3 found evidence for higher stresses as a normal condition for early-life TGO in certain blades, and disproved the possibility of laser heating as a cause for the frequency shift.

PLPS fluorescence collection efficiency was improved significantly by changing the optics used in the collection apparatus, alongside with the additional benefit of increased versatility of the target geometry that could be interrogated by the raster-scanning routine. Tests were performed to investigate any significant dependence of stress measurement on the possible heating of the TGO as a result of increased laser fluence. The effects of bimodal distributions and CMAS islands were taken into account, and weighed against the observed results to ascertain the source of error. These parametric studies are presented in detail in section 4.3.

4.1 Orthogonal Spectral Modes for LIBS Analysis

The initial method for ablation control for CMAS removal via LIBS was based on the cross-correlation of reference spectra. A reference mode for TBC had been taken from a representative sample of 7YSZ. The Pearson's cross correlation coefficient was computed in real time between this reference mode and the current spectrum collected from the spectral emission during LIBS of the target surface. However, because the cross-correlation of CMAS and the TBC reference spectra was not zero, there was an arbitrary starting point for the correlation. The stop criteria was therefore also an arbitrary fit for the expected trajectory of cross-correlation with depth. A logarithmic fit was placed on the TBC cross-correlation after a threshold value of 0.5 had been reached, as shown in Fig. 18. When the derivative of this logarithmic curve descended below the cut-off value of 0.007, ablation would cease. The issue with this method lies in its lack of versatility and physical meaningfulness.

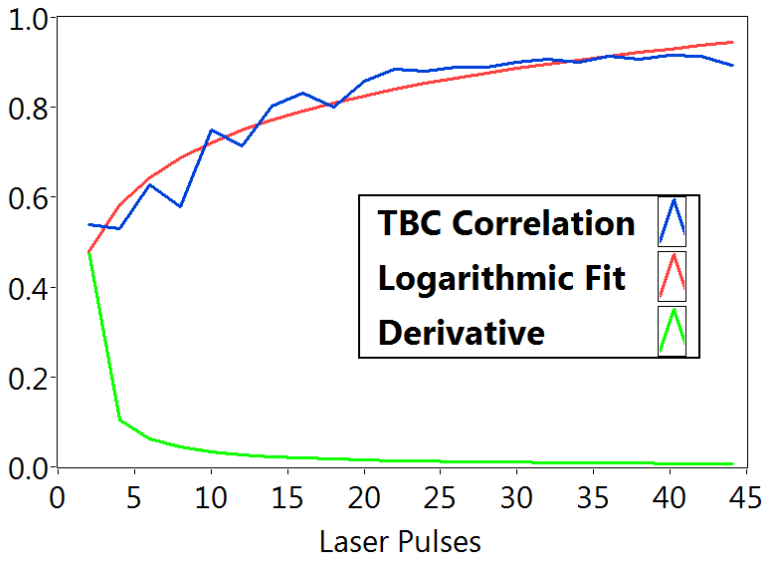

Figure 18: Example of the development of the cross correlation coefficient for LIBS spectrum with a TBC reference during a CMAS removal laser drill. A logarithmic curve is fitted to the correlation values, and the derivative of that logarithmic fit is taken in real time. When the value of the derivative falls below 0.007, ablation ceases.

4.1.1 POD for CMAS and TBC LIBS Spectral Ortho-modes

To address this non-zero correlation between CMAS and TBC, the cross-correlation fitting was replaced with a proper-orthogonal-decomposition (POD) based method. To compare this method's effectiveness, a more robust reference data set was compiled. An average LIBS spectrum for TBC was obtained from averaging thousands of individual spectral samples from un-cycled turbine blades, as shown in Fig. 19. For CMAS, six samples of ~450 spectra were taken from different areas of each of 15 engine-run turbine blades. By averaging these shots together, a representative sample of CMAS was obtained, also shown in Fig. 19. Even still, these reference spectra shared some cross-correlation, a quality which makes quantitative analysis between different species difficult.

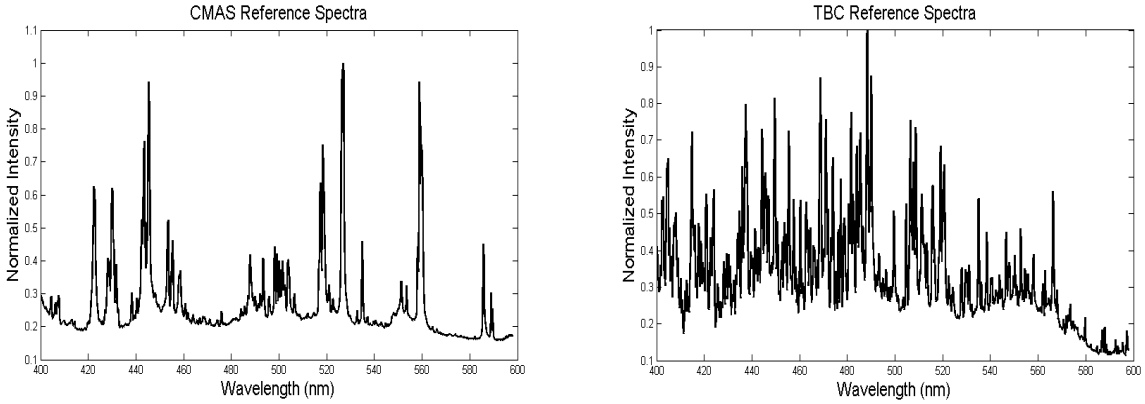

Figure 19: CMAS reference spectrum averaged over thousands of unique CMAS samples from engine-run blades (Left) and TBC reference spectrum (Right) taken from a set of turbine blades which had not been put in service.

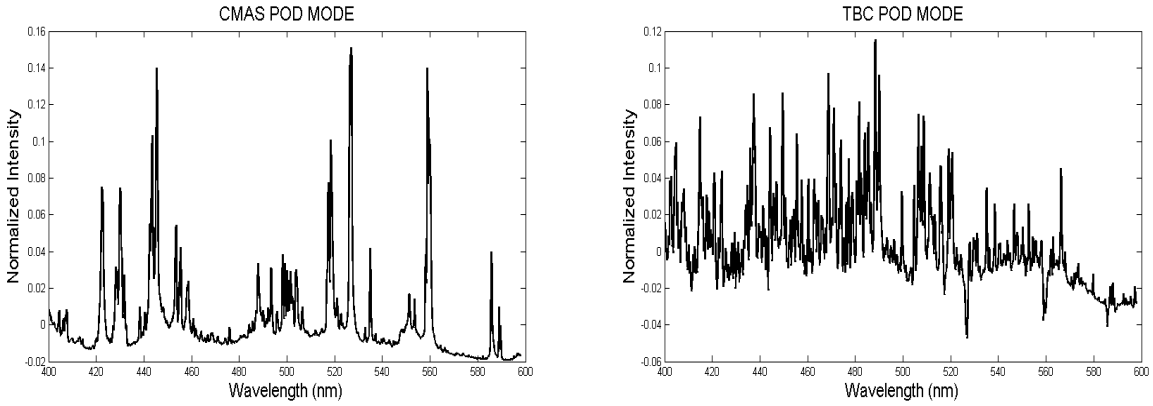

Figure 20: : POD Mode for CMAS (Left) and POD mode for TBC (Right) obtained from same data set as used to compile reference spectrum, despite a strong resemblance to the reference spectra, these POD modes are orthogonal.

This large data set of CMAS and TBC spectra were then analyzed using a singular-value decomposition routine which decomposed the spectral set into orthogonal modes. The modes which contributed the most significantly to the total variance of the data set were retained as principal modes. The two modes which contributed the most to the total variance, shown in Fig. 20, also correspond physically to the TBC reference spectrum and the CMAS reference spectrum. The orthogonal modes necessarily have a cross-correlation of 0 with respect to each other, implying that a concrete value for the presence of one species can be determined. With these orthogonal modes, it is possible to determine in real-time the total percentage contribution of each species to the collected spectra from LIBS. Thus the arbitrary logarithmic curve fitting with derivative cut-off value is replaced with a direct comparison of the species concentration with an acceptable physical quantity.

4.1.2 Improved Laser Ablation Control

By orthogonalizing the reference spectra for CMAS and TBC, ablation control for CMAS removal is made far more robust and reliable. CMAS deposits which are thicker, less

homogeneous, or subject to different conditions during deposition will have much less of an effect on the system's ability to stop ablation at the CMAS-TBC interface without damaging the TBC surface, or allowing large islands of CMAS to remain. More significantly, the stop threshold is easily modified to handle situations wherein a less or more rigorous discrimination is desired for ablation. For example, by changing the threshold from the somewhat strict expectation of 95.0% TBC to a more lenient value of 92.5% TBC, damage to the TBC may be avoided in situations where CMAS is very thin in some regions of the blade's surface. Conversely, stricter thresholds may be placed on areas which have thicker depositions.

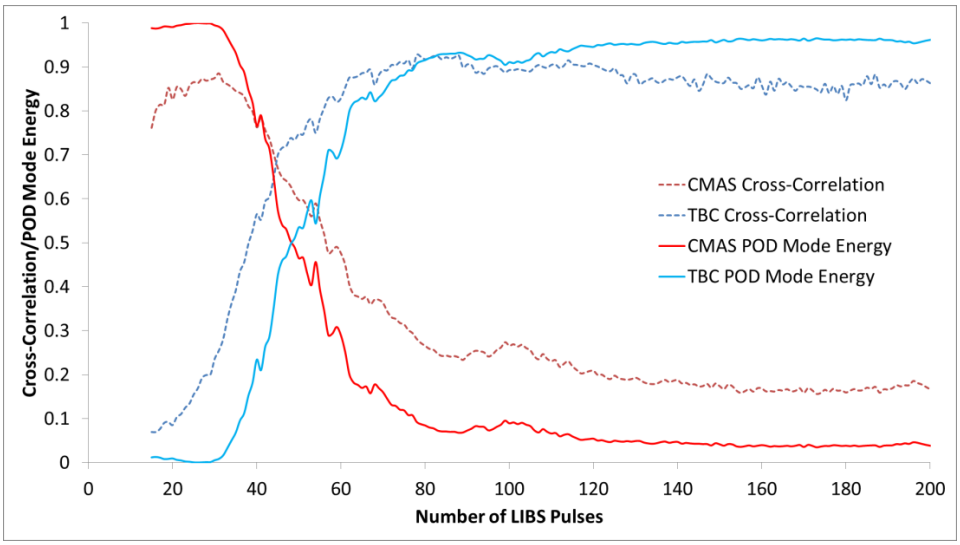

Figure 21: Comparison of the performance of reference spectra to POD modes on a sample CMAS ablation data set. Important features are the extremely intuitive initial POD values for CMAS and TBC, at 1 and 0 respectively, and the near-zero final POD value for CMAS, which reflects reality much better than the ~20% cross-correlation value.

The performance of orthogonal modes for coating species LIBS spectra were compared to the covariance method using reference spectra, as shown in Fig. 21. For this trial run, the correlation values with reference spectra (dotted lines) provided excellent ablation control, but there are two caveats. The first is that this behavior is inconsistent, especially across different

CMAS compositions and thicknesses. The second is that it is difficult to draw a physical meaning from the correlation values at any given point, such as the intersection of the two trends at 45 shots with a correlation value of ~0.7. Using the POD modes, it is possible to assign concentration values to the CMAS and TBC area coverage of the ablation crater. Thus the YSZ concentration should, and does, approach 1 at the end of ablation, as CMAS approaches 0.

4.2 Beam Profile of Pulsed Quantel Nd:YAG Laser

Two weeks prior to the July 2012 test at Standard Aero, a new Nd:YAG laser was acquired for the mobile system. This new laser is smaller and more robust than the laboratory-scale system originally used to develop the NDE Life-Analysis portable unit at UConn. However, the new laser had sufficiently different beam properties, as shown in Fig. 22, that when used in place of the previous laser, inconsistent removal of CMAS was observed, to the extent of effecting the stress measurements. A ring pattern in the CMAS removal was observed, as shown in Fig. 23, and this was found to be due to power distribution in the laser. To ensure that the proper energy density per shot was delivered on target, the energy and width of the beam were measured and optimal values were chosen for the most complete removal of CMAS.

4.2.1 Non-Homogeneous Beam Energy Density

The near-field beam energy profile demonstrates iso-energetic concentric arcs which cause higher ablation rates at some points on an ablation target than others, in a manner aptly described by a peak-trough relationship. This becomes significant when the characteristic signal of the target substance is used to determine ablation control. When the control substrate is reached by the peak arcs across the beam, ablation will be incomplete in the regions covered by the trough arcs. Typical operation of the laser for ablation purposes puts the working plane at

roughly ¾ of the focal distance, giving the beam profile characteristics a combination of the near-field and far-field profiles.

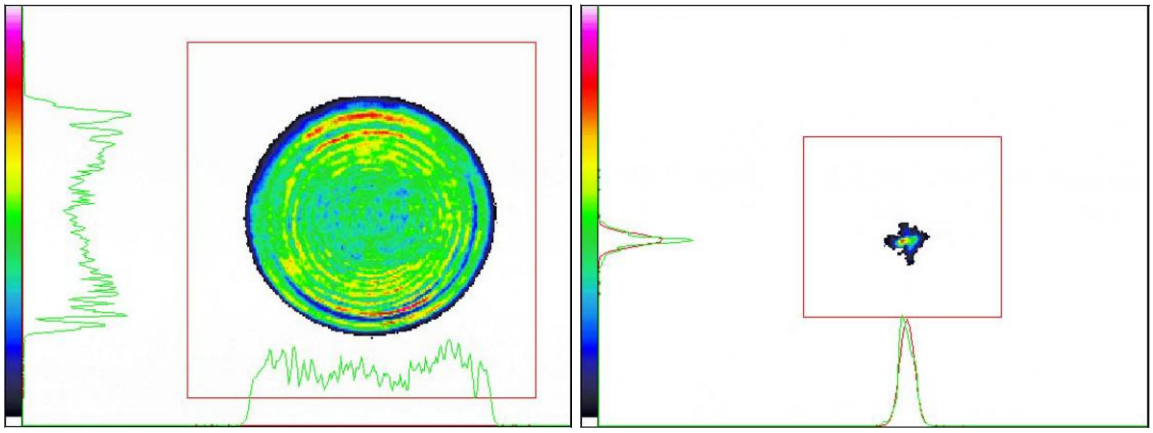

Figure 22: Beam Profile for Quantel Nd:YAG at 355 nm. The near-field beam profile (Left) clearly demonstrates patterns of high and low energy in the form of concentric rings, meanwhile, the far-field beam profile (Right) demonstrates the off-center location of a high concentration of energy. Plots provided by Quantel retailer.

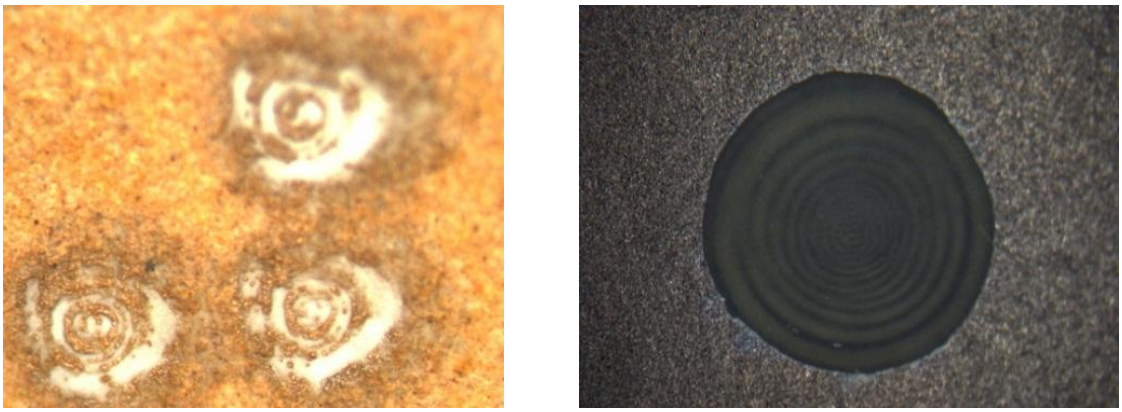

Figure 23: Uneven removal of CMAS observed during July 2012 tests on engine-run blades freshly dismounted at an engine-testing facility (left) displaying concentric rings of CMAS as a result of the beam intensity profile demonstrated by burn pattern on photo-sensitive paper (right).

4.2.2 Optimization of Laser Operation Parameters

This profile harms the effectiveness of CMAS removal process by instituting the development of defined CMAS structures within the ablation target which are too large to select against during data analysis of PLPS measurements. In order to minimize the effects of this profile, the energy density was optimized for best TBC cleaning. To this end, the laser's energy output and beam profile were characterized, in particular, the output pulse energy as a function of Q-switch delay, as shown in Fig. 24, and beam area as a function of displacement from the focal length were determined. For these tests, the instantaneous energy density of the laser pulses needed careful attention, since an instantaneous power density of 80 MW/cm^2 is sufficient to induce optical breakdown of many materials. The Thor Labs ES120C energy sensor used for this test, similar to many microscope objectives, fiber optics and mirrors, was not rated for such power, and incurred damage to its coating, necessitating a scale factor for measurement.

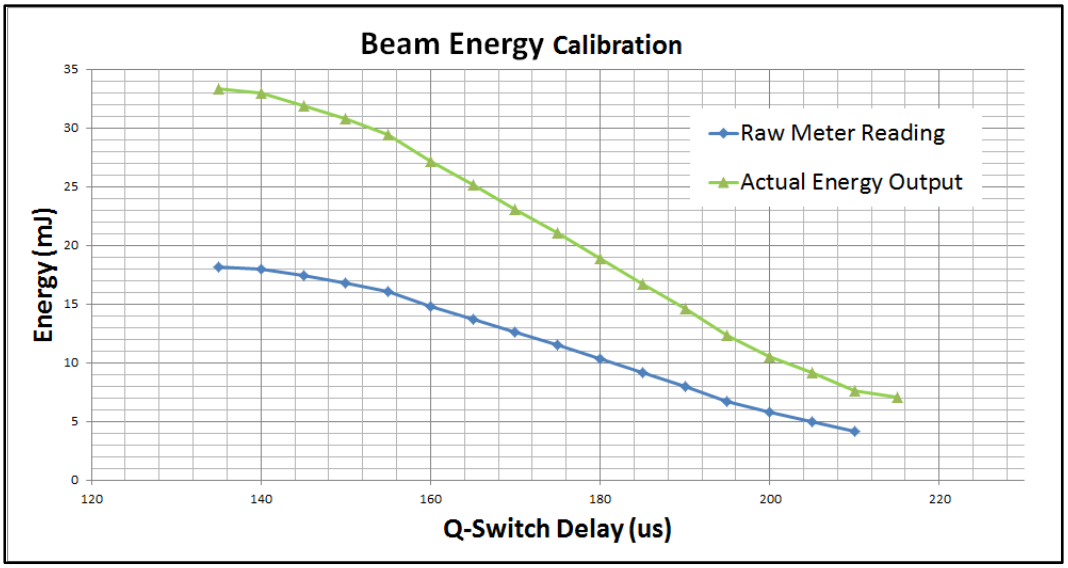

Figure 24: Calibration of laser pulse energy versus Q-Switch, necessitated by damage to energy sensor.

By expanding the Nd:YAG beam to the diameter of the energy meter it was possible to avoid damage on the coating of the energy sensor. Scaling the measured pulse energy to the maximum pulse energy specification of 33.3 mJ at 355 nm for the Quantel Nd:YAG, the correlation between Q-Switch delay and pulse energy was accurately plotted over the 135 μs to 215 μs domain. A knife-edge test was used to sample the beam diameter near the intended working plane and extending closer and farther from the focal plane. At this point the plano-convex lens used to focus the beam had a focal length 400 nm. The knife edge blocks out vertical sections of the beam in succession in a horizontal scan. The decrease of energy measurement scales with distance across the beam in a manner consistent with a Gaussian beam profile.

The results of the optimization test suggested a pulse energy of 23 mJ be used alongside a beam diameter of 500 microns for a resultant instantaneous power of 22.44 MW/mm^2. This is not far from the value of 26.0 MW/mm^2 resulting from optimization studies by Majewski. The slightly lower energy density combined with a compacted spot size seems to have a mitigating effect on the development of CMAS islands during laser ablation. The risk of glassification of CMAS from exposure to insufficient laser intensity seems to be insignificant, as this phenomenon typically occurs at significantly lower intensities for the 355 nm pulsed YAG system. Examples of the improved spot cleaning with these laser settings in shown in Fig. 25.

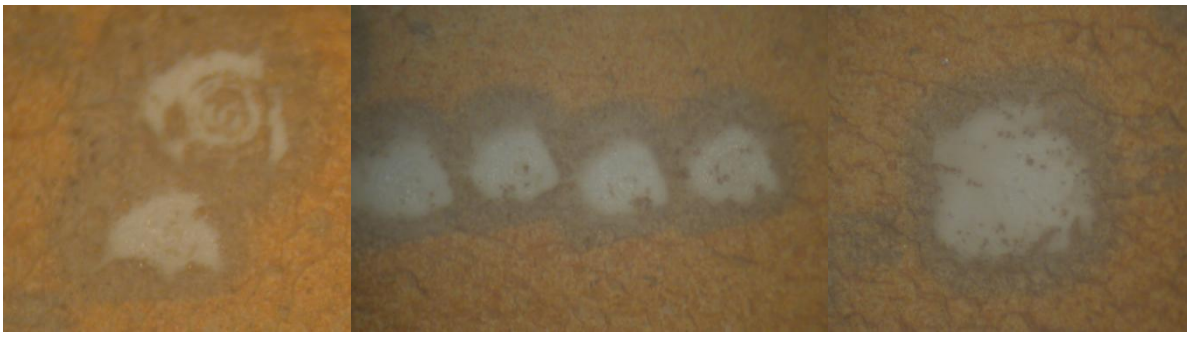

Figure 25: A pre-optimization laser spot shown above a post-optimization spot on the same target (Left) Important to note is the absence of the characteristic ring patterns of CMAS islands in the post-op target, despite the strong probability that CMAS composition is similar for the two spot locations. Four post-optimization spots (Middle) show the consistent advantage of the new operating parameter values for the ablation laser. Finally a 3x3 grid of laser spots demonstrates a preliminary attempt at solving the CMAS pattern issue by translating the ablation point.

Another measure attempted with intent of elimination of CMAS islands was translation of the ablation point. By moving the working plane of the laser beam across the target's surface, the opportunity for standing patterns of higher and lower rates of ablation to develop is greatly diminished. Initial procedures involved an overlapping grid of several ablation craters knitted together to form an elliptical shape. By increasing the number of points in the grid, and staggering the order of ablation in a leap-frog manner, undesired damage to TBC from overlapping spots can be brought to a minimum.

These set of measures to solve the problematic trend of CMAS patterns within ablation craters may be considered sufficient for the intended application. We already assert that CMAS composition varies in its thickness and composition in an unpredictable fashion, however other factors may affect its deposition and accumulation on engine components. Caution suggests that some cases may exist for which the laser operation parameters will again have to be adjusted to achieve the same effect. Throughout the range of CMAS compositions found on the engine-run blades and vanes under testing, the parameter values appear to be robust.

Another method of cleaning CMAS from TBC while minimizing developments of CMAS islands is the continuous motion ablation scan—a more elegant extension of the overlapping grid. By translating the target at a constant velocity while ablating continuously, the development of any pattern of CMAS residue whatsoever is implausible. Also, the issue of overlap relevant to the ablation crater grid method is reduced greatly by dividing the target area into a vastly larger number of overlapping points. This method has been very successful at cleaning CMAS with the minimum of islands, with the additional benefit of cleaning large areas of CMAS from the target surface. This method will be discussed in further depth in chapter 6.

4.3 Improvements to PLPS Operation in Mobile Device

The main areas of concern for the PLPS portion of the mobile NDE system were all rooted in the observation of unexpected stress values. The potential causes of this singular undesirable outcome were the basis for individual changes and investigations to the system. The first possibility was that the blades tested did actually experience bi-axial residual TGO stress values which were higher than in previous stress measurements. If the higher stress values were legitimate, then the stress domain would have to be expanded to account for them and a new set of samples would have to be cycled to failure to construct the new correlation curve.

Another possibility was that bimodal deconvolutions of signals were interpreted by the analysis package as significantly shifted stress values. Bimodal signals have been observed before over cracks in TBC or regions where CMAS constitutes a significant fraction of the PLPS interrogation point. These signals could also originate from a set of peaks with higher than average broadening, as well as saturated signals and waveforms with low signal-to noise ratio. Finally, since the heating of the TGO has a strong effect on the frequency shift with only a slight

temperature differential, there was some concern over the possibility that the excitation laser might be causing a temperature rise in the TGO over extensive measurements.

4.3.1 Increased Probe Area Versatility with New Objective

To address the low signal-to-noise ratio possibility, the collection optics for PLPS were upgraded and carefully aligned to increase the collected signal. The somewhat conveniently mismatched FC/PC connectorized fiberport and microscope objective were replaced with a long working-distance microscope objective and a plano-convex lens for fiber-coupling to the WDM. As a result, the collection efficiency was increased by roughly a factor of five, allowing for a much shorter dwell time per data point with higher signal quality. Additionally, the long-working distance lens sits 35 mm from the target plane, enabling analysis on many more areas than were previously possible, as dictated by the geometry of the turbine blade and vane assemblies.

4.3.2 PLPS Signal Collection Expedited

The effects of noise from standard operation of the spectrometer are most significant for collections at lower integration times, under the assumption that transmitted laser power is below the threshold to induce an intense fluorescence above a sufficient count rate. Figure 26 shows an example of a high-signal intensity measurement at a higher integration time. The signal is de-convoluted into a unimodal set of peaks. Despite the fact that the noise absolute magnitude is higher for this measurement than for the previously displayed bimodal de-convolution scenario, the signal is easier to process, with a signal-to-noise ratio above 20.

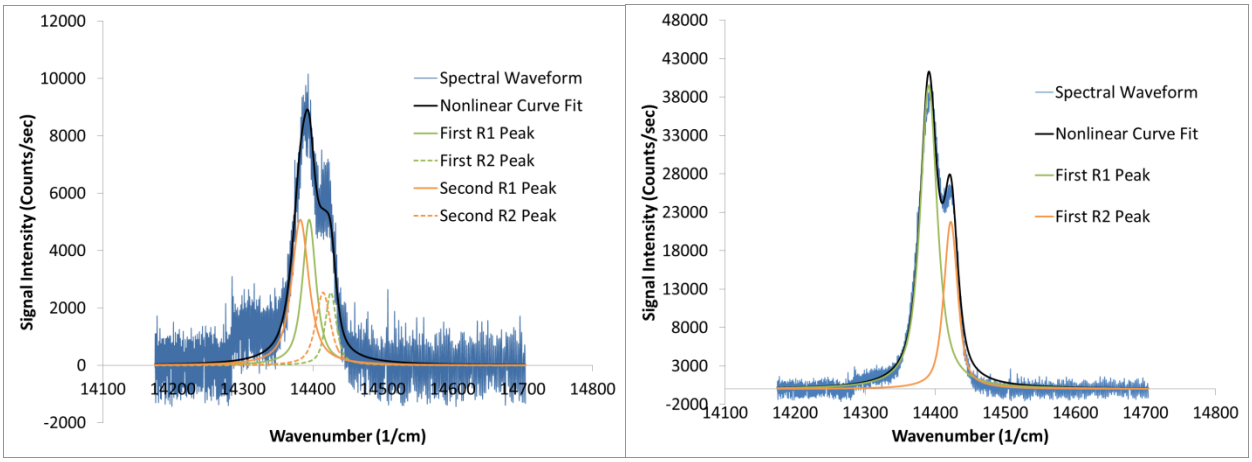

Figure 26: Example of bi-modal deconvolution of low-intensity signal (Left) Compared to a uni-modal deconvolution on a signal with good signal-to-noise ratio (Right). In the bi-modal case, two R2 peaks are taken instead of one, causing a shift in the measured stress. Evident is the low signal to noise ratio, likely forcing the bi-modal deconvolution.

The dark signal for the PLPS spectrometer was measured at various integration times, averaged over 50 measurements at the same conditions as shown in Fig. 27. The background noise is relevant on the pixel array encompassed by the Ocean Optics USB4000 Spectrometer between 650 and 720 nm. The dark signal intensity level was found to scale linearly with integration time. From these tests, the rate of increase for dark signal amplitude of roughly 1000 counts per second is quickly overtaken by the rate of increase of fluorescence with respect to integration time. Thus any negative influence from increased dark signal will be more than compensated for by the associated increase in signal amplitude. The result is signal quality steadily increasing with integration time. This continues until the saturation limit, above which the peaks lose their shape, and a peak center cannot be extracted from the waveform.

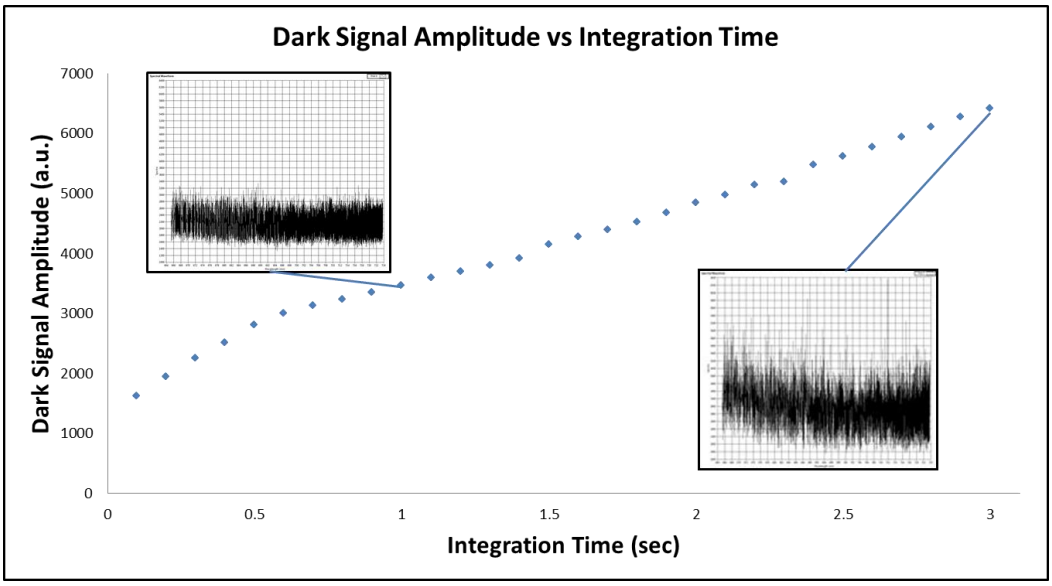

Figure 27: Dark signal amplitude vs. integration time over the range of 0 to 3 seconds in the absence of laser excitation.

A sub-routine was added to the collection software which handles signal saturation by predicting signal amplitude at 90% of the saturation level, and adjusting the spectrometer's integration time accordingly. The optimum operating range lies at least 5% below the saturation limit, but higher than 50% of the limit. Within this domain, any failure to de-convolute fluorescence peaks is a function of the output signal waveform, and not of the spectrometer's operation parameters.

4.3.3 Extended Stress Domain for Engine-Run Blades

Previously, it was shown that stress measurements obtained from engine-run samples sometimes yielded stress values that exceeded the bounds of the stress domain obtained from prior calibration measurements, hence yielding uninformative life-fraction values. This raised a question about the currently employed stress correlation of the turbine blades being tested, and resulted in the necessity of obtaining a new correlation curve for stress and remaining life. Rolls-

Royce has provided coated but unused turbine blades for determination of the zero-life-fraction stress. In ongoing work, Rolls-Royce is preparing several dozen TBC-coated substrate button samples. These will be thermally cycled, and a complete calibration curve will be re-constructed from PLPS measurements on the button samples at every stage throughout successive thermal cycling, until spallation failure. The new stress values for unused blades received from Rolls were examined and these blades have been used to explore possible bias errors that could affect the stress including signal-to-noise ratio.

The unused turbine blades with new TBC were used in the determination of the baseline stress. That is, the residual stress in the TGO immediately after it forms, giving the closest possible approximation of the stress value correlated with 0% life fraction. One of the unused blades was cycled once in a furnace at 1123 ºC for a duration of two hours in order to induce the formation of a TGO layer with sufficient alpha-alumina for a stress measurement. Once the threshold for growth of the oxide layer had been passed, measurements were performed on the blade to confirm the stress value. Though the stress values do not truly correspond to a life-fraction of 0, since some cycling has occurred, the departure from un-cycled conditions is considered negligible, and these first measurements are for all intents to be considered the baseline for stress-life fraction correlation.

Eight trials with 2,500 data measurements each were taken on the blade, at a constant laser power and varying integration times for the PLPS spectrometer. Integration times were modulated from 0.5 seconds to 2.5 seconds, such as to vary the signal-to-noise ratio to address any potential change in the recovered stress due to data quality. The measurements were taken on a 2mm x 2mm area on the upper portion of the tailing edge of the turbine blade's pressure side. The tolerance for positioning of the interrogation point on the turbine blade is considered

negligible with respect to the target area. Moreover, for a blade with no exposure to atmospheric contamination at engine operating conditions, the stress distribution within the blade should not vary significantly as a function of blade location, especially within the narrow domain defined by stepper motor tolerance. Thus we take these measurements a representative average of the local stress values throughout the TGO.

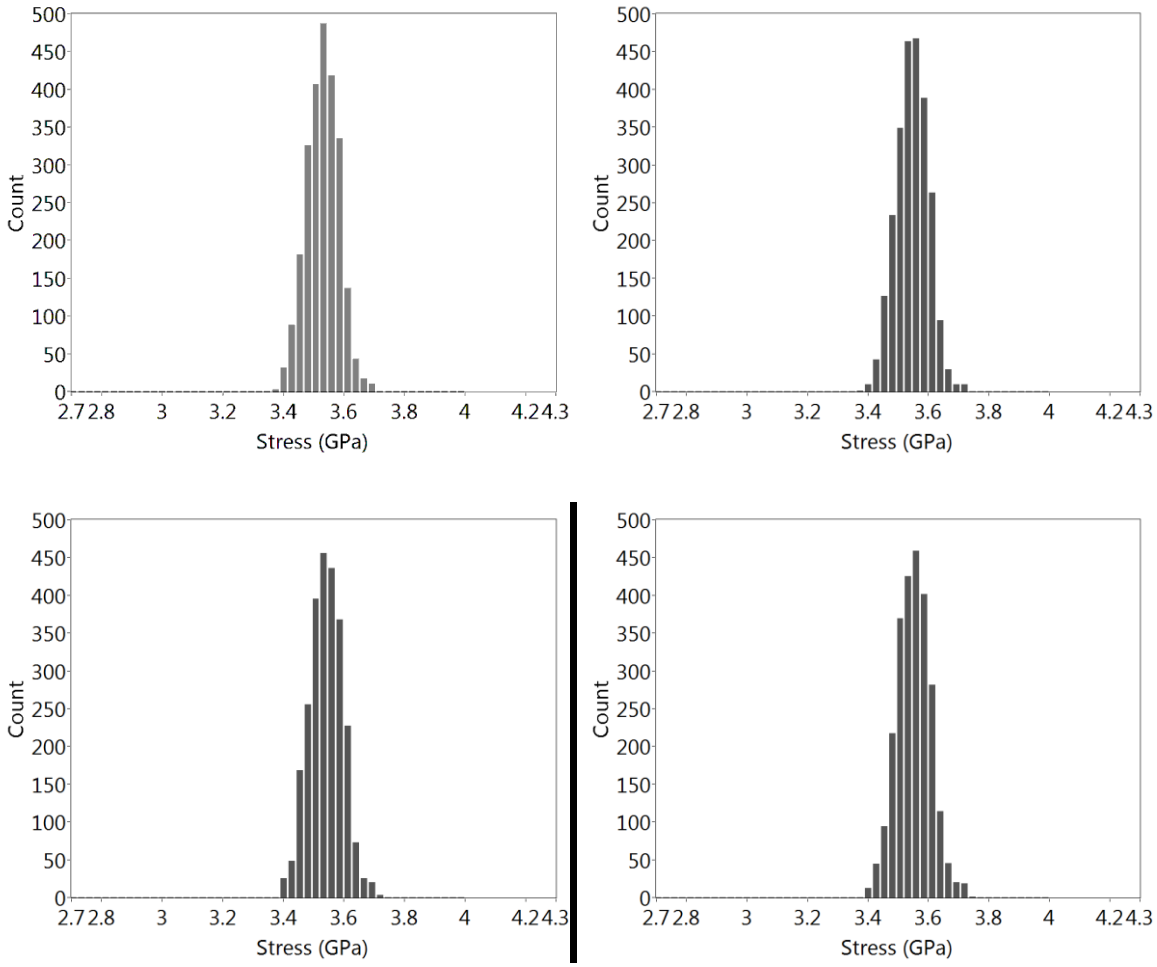

Figure 28: Stress measurements on the cycled blade using various integration times. From left to right: Top row: 0.8 sec, 1.0 sec. Bottom row: 1.5 sec, 2.0 sec. Stress histograms are well-formed, with a consistent center about 3.5 GPa.

A ‘merit value’, adopted from Selcuk, describing the quality of signal fitting was set as the threshold for data retention. The merit value is a discretized metric which compares the collected spectrum with a fitted curve over the same pixel domain, and is calculated as:

$$m = 1 - \frac{\sum_i^n (X_i - E_i)^2}{\sum_i^n (X_i - \bar{E})^2}$$

Where X_i is the intensity of the collected spectrum at the ith pixel, E_i is the calculated intensity from the fitted curve, and $\bar{E}$ is the mean value for the fitted curve. The value varies from 0 to 1, with 1 being the highest possible agreement between signal and curve. The value for acceptable fitting quality may vary based on the data set, but values below 0.95 are rarely considered acceptable. For integration times greater than 0.5 seconds, sufficient signal was obtained such that the PLPS fit to the data passed the merit value and the recovered stress was deemed valid. The histrograms of these stresses are shown in Fig. 28. At lower integration times, i.e. 0.5 seconds and 0.3 seconds, (Fig. 30) the lower signal caused obfuscation of the peak shapes, due to low signal-to-noise. For lower integration times the waveforms lacked distinct definition of peaks and peak separation, as would be expected by a poor signal-to-noise ratio, and were discarded. At lower signal intensity, the signal was interpreted as a bimodal set of peaks. These bimodal peak fits have previously been observed for low quality fits and are typically discarded.

The ‘merit values’ for these low-signal collection samples were homogenous and below the discrimination threshold of 0.975 (which is lenient compared to typical threshold of 0.99). For this reason, no stress values were accepted from the low integration time trials. The measured stresses from the bimodal fits, had they been accepted, were above 4.0 GPa, a value at least 500 MPa over the average values from the higher signal tests. A similar scenario occurred when the signal was too high, and saturation of the spectrometer’s pixels yielded a truncated

peak which could not be properly de-convoluted into peaks. In such cases, though the R2 peak may mathematically match the data, it is shifted heavily to adjust for the poor R1 fit. This effect is evident through dense fluctuations in stress values (Fig. 29). Repeating the measurement with lowered signal intensity causes the reversal of this aberration. For this reason, the results are not considered acceptable, even though the merit value threshold may be satisfied.

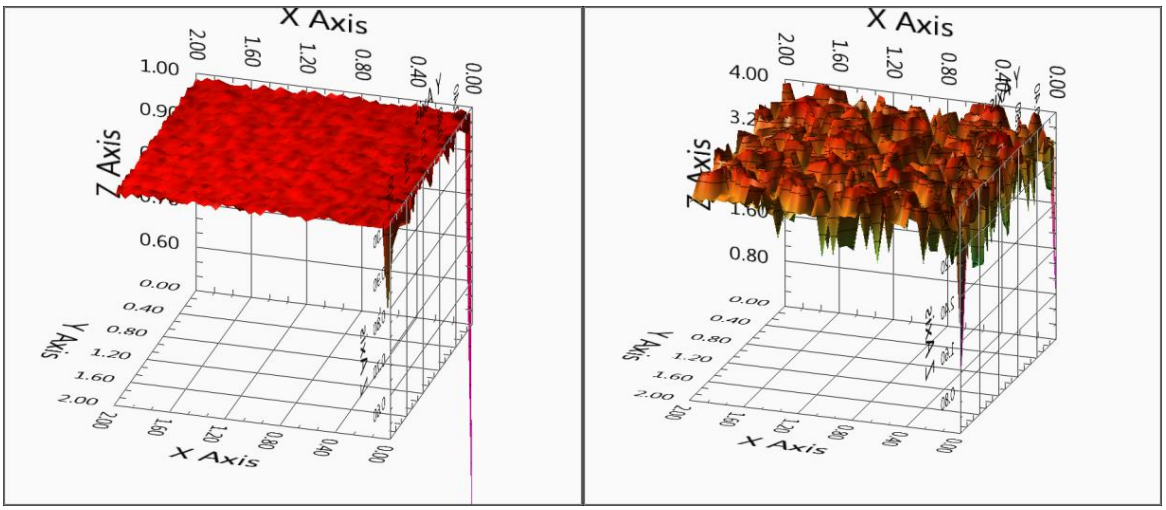

Figure 29: Measurements at integration time of 2.5 sec: Signal Quality (left) and Stress Measurement in GPa (right) Stress values are sporadic, though centered about of 3.6 GPa, with somewhat turbulent signal quality. The X and Y axes correspond to a mapping of the data points over the physical space covered by the raster scan. The units are in mm.

In the case of overly-long integration time causing a uni-modal set of peaks with a higher frequency shift than is physically expected, the count rate is sporadic, causing fluctuations in the stress measurement, and of course, the data points will be of lower quality. Large differences within a single measurement over a target area are not necessarily wrong, but large fluctuations that create a discontinuous stress map with many sharp features are indicative of poor data, especially when the fluctuations correspond with merit value dips.

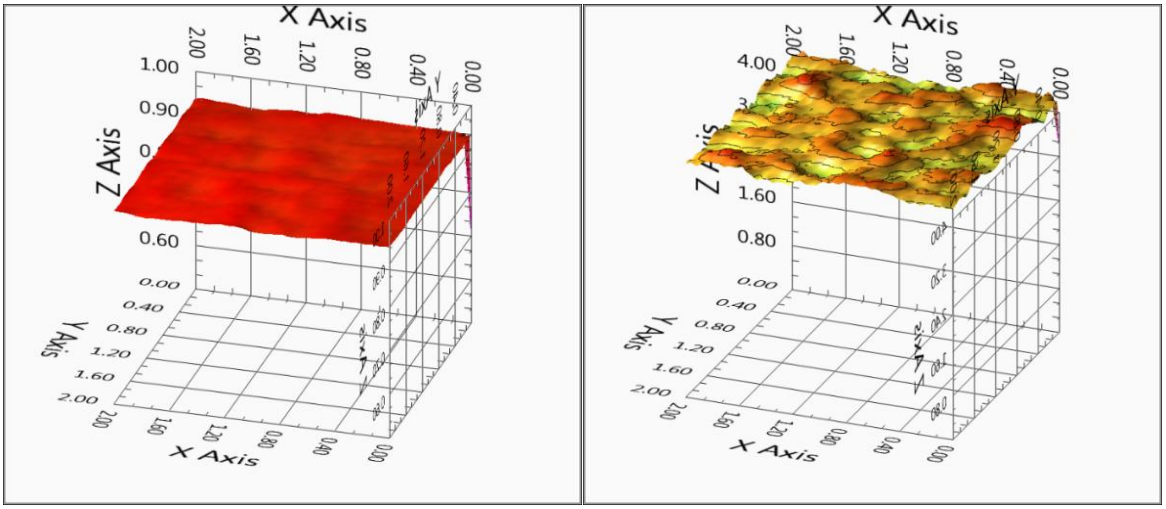

Figure 30: Measurements at integration time of 0.3 sec: Signal Quality (left) and Stress Measurement (right) Note Stress values above 4.0 GPa and merit values considerably below the threshold.

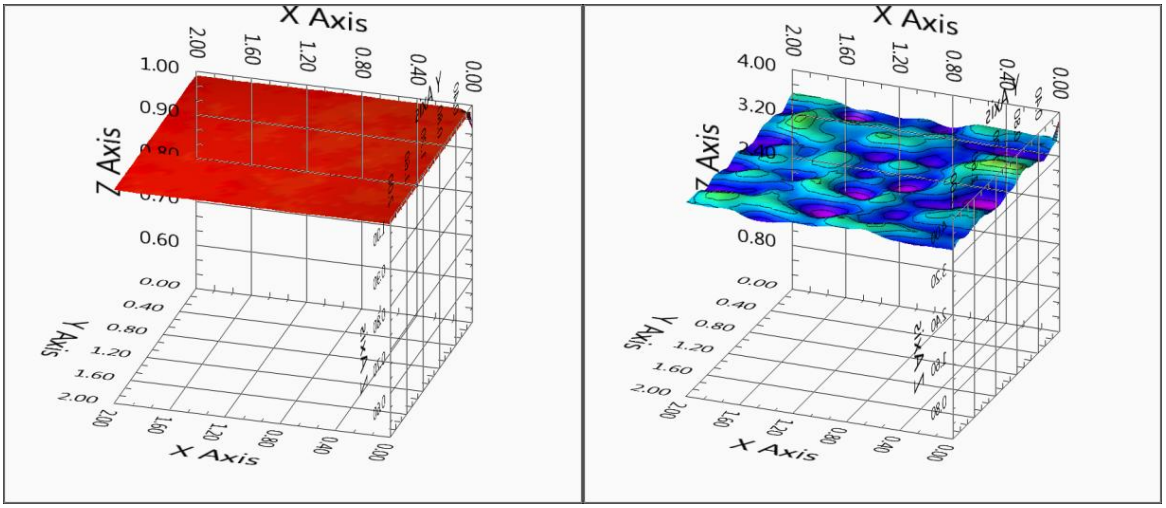

Figure 31 : Measurements at integration time of 1.5 sec: Signal Quality (left) and Stress Measurement (right) Stress values are in the range of 3.3 to 3.6 GPa, with strong agreement in the signal quality

The example shown of the 1.5 second trial, shown in Fig. 31, is representative of high quality data which is obtainable over a relatively broad range of values for several operation parameters. With the effects of CMAS or even the undesirable after-effects of laser ablation,

such consistent data is more difficult to reliably obtain. However, the mean values for engine-run tests reflect an agreement of mean stress that does not depart far from expected values. The challenge is to minimize the deviating effects resulting from signal quality in such a way that preserves the actual stress values. Maximizing signal-to-noise ratio by properly adjusting spectrometer integration time will achieve this end for a sample with a clean surface, such as the provided turbine blade. This can be done easily by ramping the integration time on the spectrometer during an LIF test. The lowest value at which signal will reach an optimal intensity is determined by iteratively comparing the ratio of max intensity gain with noise level increase. With imperfections on the TBC surface such as are imposed by CMAS deposits, or slight alteration of the TBC surface due to laser ablation, distortion of the PLPS waveform is managed by exclusion of data points, to preserve the most accurate representation of the TGO stress. If too many data points are affected, the surface often requires more cleaning; otherwise, excessive ablation may have damaged the TBC surface and measurement is blocked locally.

Table 1: Stress statistics corresponding to zero-life-fraction (new TBC) for different signal integration times.

Integration Time (sec)	Mean Stress (GPa)	Minimum Stress (GPa)	Maximum Stress (GPa)	Data Retention
0.8	3.475	3.310	4.268	99.96%
1.0	3.483	2.705	4.120	99.28%
1.375	3.498	3.343	3.675	99.96%
1.5	3.481	3.329	3.664	99.96%
2.0	3.492	3.336	3.680	100%
2.5	3.607	2.688	4.123	92.55%

The stress of the cycled blade is consistent versus integration time indicating that no bias in the results occurs as long as the signal is sufficiently high and within the saturation limit. Our current merit value threshold filtering method appears to successfully reject the low-signal cases, by rejecting datapoints below a minimum signal fitting quality, e.g. 0.97. From the

measurements with high-quality signal, summarized in Table 1, the average early life stress can be taken to be 3.487± 0.012 GPa. This suggests a meaningfully higher beginning stress for the un-cycled blades than previously seen at 2.38 GPa. Values of 4.0 GPa or higher have been confirmed to be products of poor signal quality, or errors in signal analysis. However, the values obtained from tests with proven high-quality data are to be interpreted as physical, lending more necessity to the re-construction of a life-fraction correlation over an extended stress domain.

4.3.4 Potential Effect of Laser Heating on PLPS

The question of temperature change in the TGO as a function of laser fluence was tested by modulating the laser power over a range of 50 to 200 mW. This was done utilizing beam-splitting optics arranged in combinations to yield various power values. In a separate trial, the diode laser duty fraction was changed to test the effect of average power, though the beam-splitters gave the advantage of controlling both instantaneous and average power. In either case, the spectrometer integration time was adjusted to the power of the excitation laser such as to hold the signal intensity constant, and thus avoid the potential frequency shift from variable signal quality. The power range was chosen to reflect operating parameters that included and exceeded typical operation ranges; greatly below 100 mW, signal is reduced, and near 230 mW, fiber optic components begin to suffer thermal damage. Thus if the diode laser was to cause a thermal effect in the TGO during typical operation at a laser power of ~180 mW with a duty fraction of 0.8, the trend would be apparent over the chosen power range.

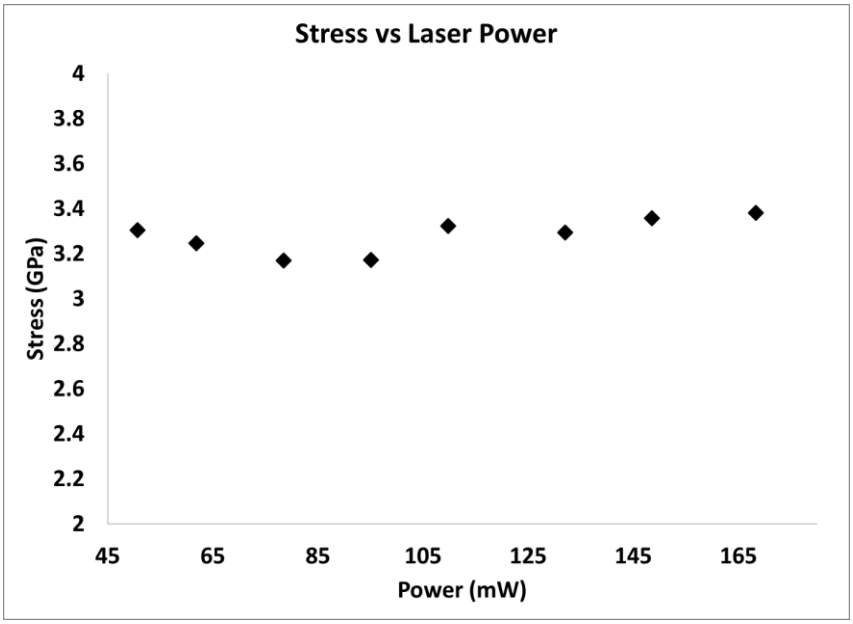

Figure 32: Graph showing the experimental results for the investigation of TGO stress dependence on excitation laser power. Over the full range of the diode laser power within which it was possible to take PLPS measurements, no significant trend in Stress values developed. This implies that any TGO heating is likely not a result of the diode laser.

Over the trials, there was no measureable shift from laser power of 50 mW to 200 mW beyond that of standard deviation, as shown in Fig. 32. The stress values maintained constant at 3.487± 0.012 GPa for the clean, thermally-cycled blade. There was no observed trend in frequency shift which might indicate laser heating was responsible for the higher stress values previously measured. However it is important to note that heating could cause such an effect if the TGO were actually exposed to a sufficient temperature gradient. With the effectiveness of the thermal insulation provided by a thermal barrier coating, it is unlikely that short-term heating at low power would have a measureable impact on the TGO before the heat could be dissipated in the ceramic. But given enough time to drive to steady-state with a high enough temperature difference the TGO temperature could change, especially when denied the additional internal cooling jets which would be in effect during engine operation. For this reason, it is

recommended that this NDE technology be limited in use to situations where the engine components are given sufficient time to cool to ambient temperature.

4.4 Standard-Aero Field Demonstrations

To demonstrate the effectiveness of the mobile NDE system in the field, a series of visits were planned to the Standard Aero testing facility in Alcoa, TN. The testing facility regularly services Rolls Royce engines, and would be an ideal location for implementing the mobile technology. Engine-run turbine blades were provided from an inventory compiled recently from dismounted engines, and remaining life predictions were projected from stress measurements taken with the mobile device. The device's performance was tested in July 2012, upon the full integration of a compact Quantel Nd:YAG laser into the mobile, self-contained system. The second visit occurred in November 2012, after modifications had been made to the system to address performance issues observed during the previous visit.

4.4.1 July 2012 Standard Aero Demonstration

The mobile system was transported via ground shipping from UConn to the Standard Aero testing facility in Alcoa. Nineteen turbine blades were inspected using non-destructive evaluation techniques, as well as a destructive exploratory probe tests. All turbine blades were taken directly out of inventory for engines dismantled during the current maintenance cycle at the facility. Thirteen were chosen for lifetime prediction measurements, as described previously. This was the first field test of the reduced system with a compact Quantel ULTRA Nd:YAG laser with ICE450 combination power supply and pumped coolant reservoir. As such, there were some issues with alignment stability which caused a discontinuity in the target coordinate system. Specifically, repeated misalignment of the PLPS interrogation area with the LIBS crater

necessitated constant readjustment, lengthening the test time significantly. Besides this and other small issues including stepper motor failures, sub-optimal laser operating parameters caused insufficient ablation of CMAS, leaving relatively large areas where PLPS data was corrupted.

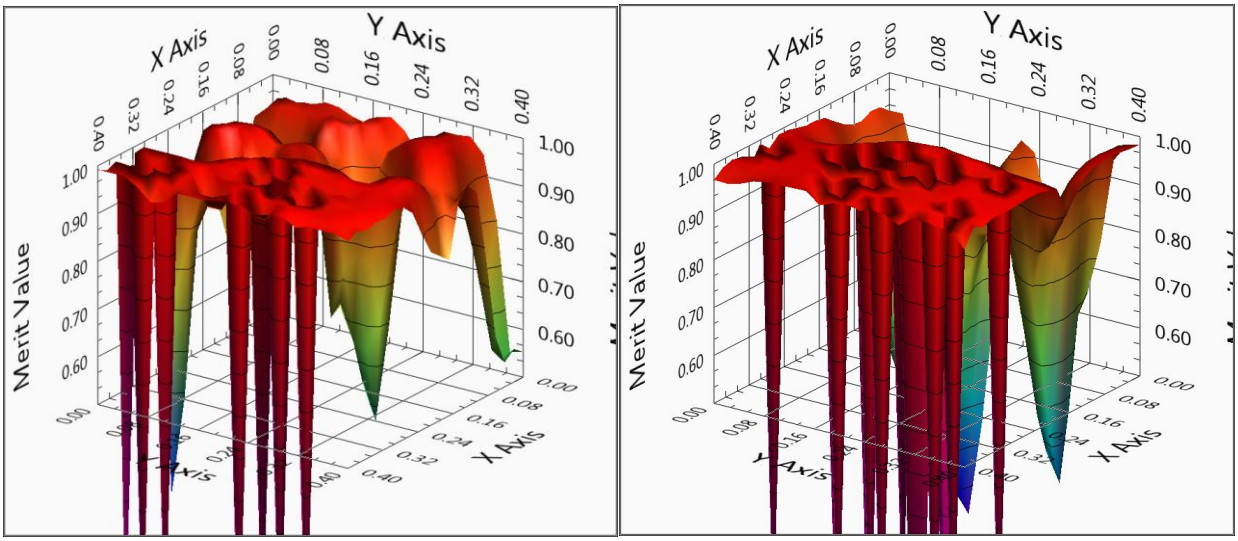

Figure 33: Merit value maps describing the signal fitting quality of waveforms obtained from the PLPS raster scan across the ablation hole. The sharp, negative peaks signal the presence of very poorly fit curves—implying data with low fidelity.

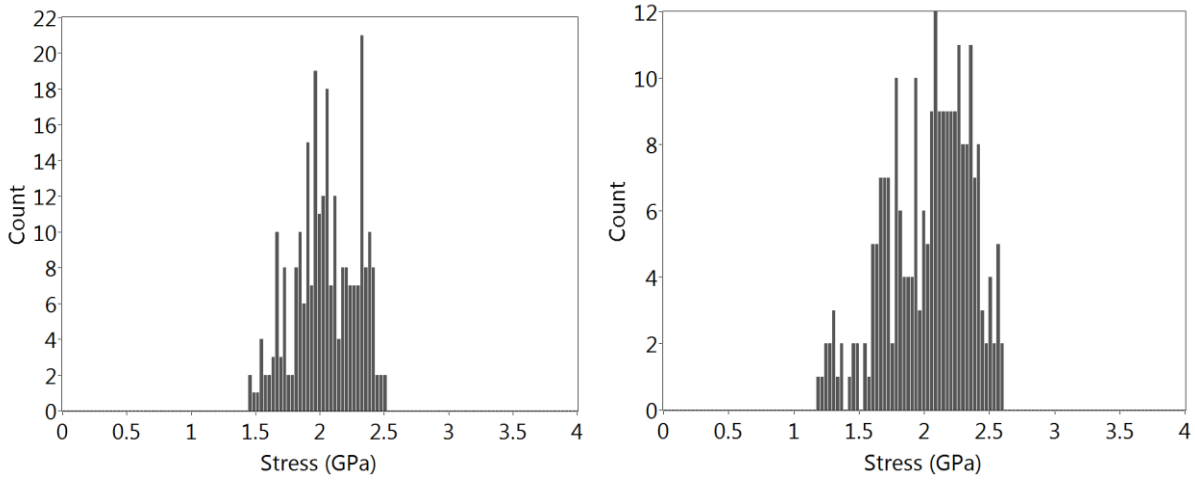

Figure 34: Typical stress histograms from PLPS measurements taken inside ablation craters over engine-run turbine blades

The effect of large CMAS "islands" is visible in Fig. 33, which shows the low signal fitting merit values. These low value peaks correspond well with the presence of CMAS causing bimodal PLPS waveforms or attenuated fluorescence signal. Despite the abundance of contaminant interference, the high resolution raster scans were able to capture a sufficient number of valid stress measurements which were found to be of acceptable quality. The corresponding stress histograms are shown in Fig. 34, and the results are summarized in Table 2.

Table 2: Results from stress measurements taken from turbine blades during the field demonstration in July 2012

Turbine Blade Trial Number	Mean Stress of Blade	Std. Deviation of Histogram	Minimum Stress	Maximum Stress	High Merit-Value Points
1	1.924	0.135	1.554	2.327	56.25 %
2	1.775	0.363	0.880	2.625	93.0 %
3	2.210	0.217	1.526	2.483	100 %
4	1.448	0.388	0.647	2.210	65.33 %
5	1.003	0.237	0.605	1.601	81.77 %
6	1.610	0.379	0.647	2.545	92.88 %
7	1.187	0.251	0.630	1.772	84.0 %
8	1.351	0.388	0.647	2.975	61.0 %
9	1.021	0.114	0.825	1.262	64.88 %
10	1.484	0.562	0.647	2.210	88.0 %
11	1.375	0.367	0.647	2.076	86.22 %
12	2.532	0.294	1.324	2.899	89.33 %
13	2.423	0.268	1.580	2.936	91.0 %

The system was able to safely analyze most of the turbine blades from several different engines, and the exceptions were due largely to those blades which had become damaged due to operational anomalies. For example, one such case involved a blade which had been plastered in finely ground aluminum alloy, which was determined to be the remains of a shredded compressor blade which had broken off during engine operation and was pulled through the entire turbojet. The blades tested displayed a wide variety of average TGO stresses, spanning the stress domain on the previously developed life-fraction curve for EB-PVD coating systems.

4.4.2 November 2012 Standard Aero Demonstration

Upon full implementation of the system upgrades and improvements mentioned in this chapter, a second demonstration was carried out at Standard Aero to revisit the performance of the analysis unit in the field. As before, a number of first-stage turbine blades were pulled from engines undergoing service in the maintenance facility and used as the objects for analysis. Improved PLPS collection and waveform handling was employed to ensure the maximum data retention. Some experimentation with target translation addressed the issue of extremely thick CMAS deposits. Successful measurements were taken from all turbine blades tested when the blades' coatings were in a condition expected from engine wear prior to failure.

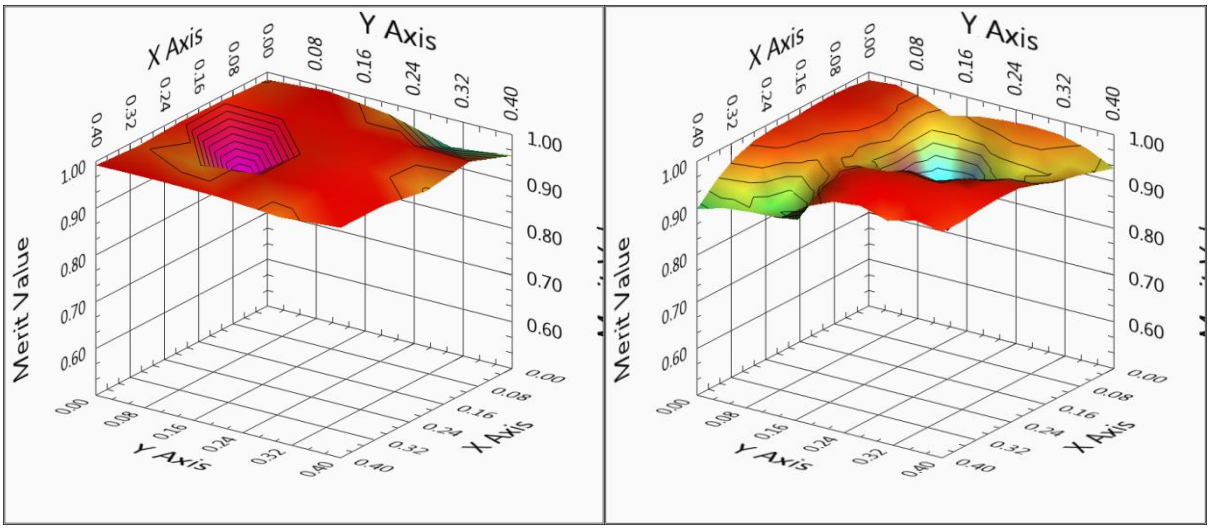

Figure 35: Merit value maps describing the signal fitting quality of waveforms obtained from the PLPS raster scan across the ablation hole. The signal quality experiences some variation, but there are no anomalous points.

The signal fitting quality metric was not constant over the ablation crater, which is consistent for YSZ with variation in the columnar microstructures, a natural condition for EB-PVD applied topcoats, as the example given in Fig. 7, yielding fluorescence capture efficiencies that change point by point. It is also consistent with imperfect CMAS ablation, to the extent that

the somewhat unavoidable occasional CMAS islands remain. However, there were not any zero spikes, resulting from extremely low signal or very clearly bimodal waveforms. The merit value maps for these tests were smoothly continuous without any significant dips or variation, as shown in Fig. 35. This implies the significant interference due to CMAS has been removed from the PLPS measurement as a result of optimized ablation parameters. The stress histograms also reflect this, as in Fig. 36, displaying a smooth distribution of stresses

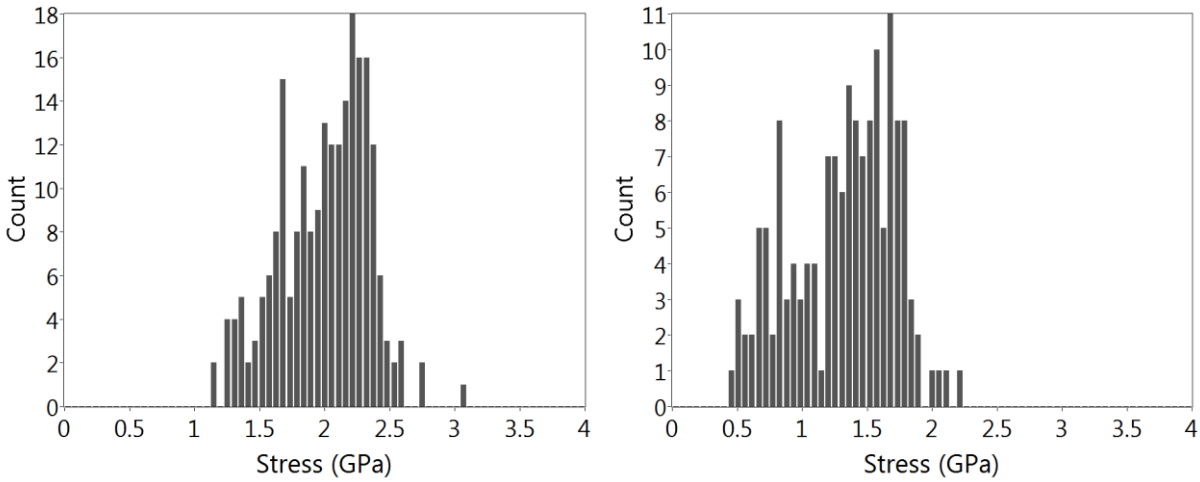

Figure 36: Typical stress histograms from PLPS measurements taken from inside ablation craters on turbine blades analyzed with the upgraded system.

Of the blades which were chosen for standard remaining-life assessment, the data retention was very high, with, on average, over 90% of interrogation points yielding PLPS spectra which were easily deconvoluted into accurate R1 and R2 peaks. Of those points where the merit value threshold was not satisfied, the TGO stress which was extracted from the waveform would have been in accordance with neighboring points. The average life-fraction from a sample blade is shown projected onto the stress-life fraction correlation curve in Fig. 37. With increased success with CMAS ablation, and the cleaner PLPS scans which are made

possible thereby, it may be useful to redefine the merit value constraints. The results from the demonstration of stress measurements are summarized in Table 3.

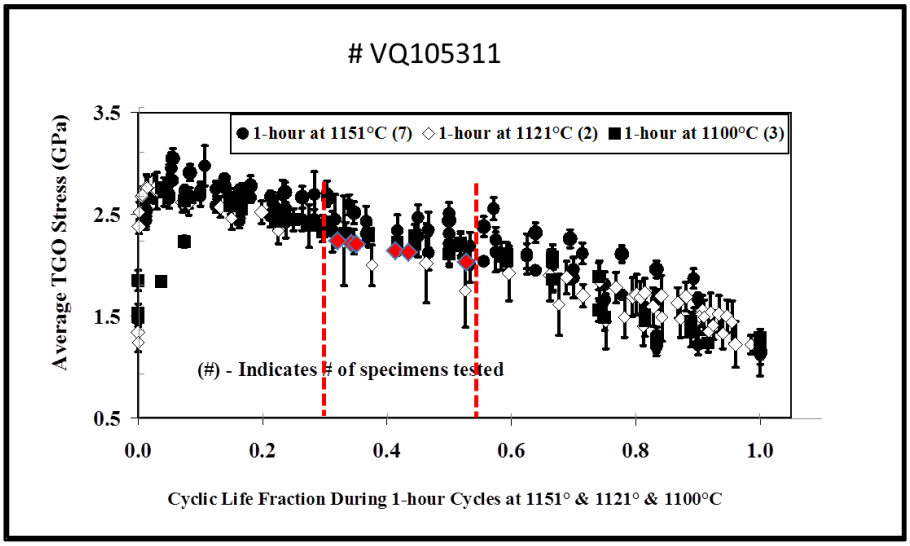

Figure 37 Projection of the results from a single turbine blade onto the life-fraction stress correlation for EB-PVD TBC. Turbine blades from the engines tested during this demonstration follow a stress-life curve which is most closely approximated by the correlation resulting from the 1121°C 1-hour cycle scheme.

Table 3: Results from stress measurements taken from turbine blades during the field demonstration in November 2012

Turbine Blade Trial Number	Mean Stress of Blade	Std. Deviation of Histogram	Minimum Stress	Maximum Stress	High Merit-Value Points
1	1.134	0.416	0.430	2.063	100 %
2	1.409	0.578	0.814	3.085	88.0 %
3	1.564	0.628	0.647	3.104	96.0 %
4	1.489	0.519	0.556	2.214	88.0 %
5	1.102	0.052	0.958	1.214	92.0 %
6	2.037	0.389	1.417	2.487	76.0 %
7	1.725	0.197	1.480	2.458	96 %

As before, transportation of the system from Connecticut by passenger car necessitated the unit be fully disassembled for protection against vibrations experienced during travel. Unloading, assembly and extensive calibration processes collectively make up a preparation time that would not be expected if the device were deployed in regular service. However, due to precautions taken with alignment, setup time was significantly decreased. It does not appear that the instrument is at significant risk of damage through transport, and an even more compact prototype which requires no disassembly for transport could conceivably be constructed.

5 Optical Fiber Components for *in situ* TBC Life Analysis

The prototype unit for thermal barrier coating remaining life analysis, or TRLAT provides the ability to analyze turbine blades and stator vanes from small aircraft engines at an overhaul facility without the need for transporting to a separate laboratory (Lake, 2012). The next stage of development seeks to create a mobile unit with its operation modified to implement optical fibers encased in a borescope, allowing non-destructive evaluation of TBC systems without the need to dismount or disassemble the aircraft engine. To carry out the full diagnostic routine, the CMAS removal via LIBS must be actualized via a flexible waveguide, and the subsequent PLPS measurements must be taken through a fiber bundle. Coherent fiber bundles were added into the PLPS apparatus and used to take PLPS measurements on engine-run turbine blades, as well as thermally cycled TBC-coated button samples. A comparison of the performance of two fiber bundles was made, with the standard PLPS technique as a control. For fiber-implemented LIBS, a number of fiber optic patch cables, and other waveguides such as fused silica rods were tested to achieve a sufficient transmission efficiency for ablation of CMAS. The damage thresholds for fused silica has been characterized for the several types of waveguides investigated in this study.

5.1 Optical Fiber Bundles for PLPS Measurement Scans

Since it is necessary to make PLPS measurements at multiple locations within a single LIBS hole to isolate the signal from any remaining CMAS, the PLPS fiber measurement must permit translation of the focused PLPS excitation laser over the hole. Manipulation of stage positioning controls on the proximal end of the fiber bundle manipulates the location of the excitation laser beam on the plane of the fiber face, as demonstrated in Fig. 38. This controls the

fiber or fibers that transmit the excitation laser, and the focal point is translated accordingly across the focal plane on the distal end of the bundle.

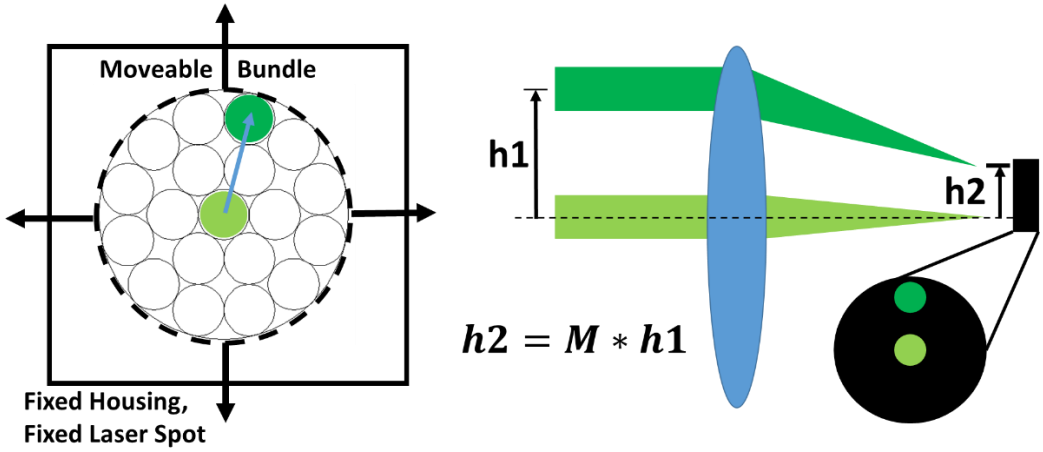

Figure 38: Diagram of translation of bundle face across laser spot, and the corresponding change in interrogation point on the distal end. The magnitude of the spread of points on the target is a function of bundle diameter and objective magnification.

Thus multiple measurements can be taken in a single analysis location without the need to move the borescope which would house the fiber optics. The projected fiber bundle face is focused to the diameter of a LIBS crater, such that the range of motion for the probe point spans the area which has been cleared of CMAS. The same data analysis routine which handles PLPS spectra from the standard method is equally effective on spectra collected through a fiber bundle. The fundamental difference that evolves is the method of translating the interrogation point. A manual 2-D translation stage is currently used for moving the fiber bundle in the plane of its face. However, this setup could be upgraded to include electronically controlled stepper motors to fully automate the process.

5.1.1 Characteristics of Optical Fiber Bundle Types

Of the many types of fiber bundles readily available, two were chosen to investigate performance at high and low limits of fiber size. One was a coherent bundle with 19 fibers of 200 μm diameter. This configuration is a perfect packing for an SMA-905 fiber termination, and provides 19 discrete test spots in a LIBS crater across an area of 1.10 mm diameter, since it is possible to channel the excitation laser into a single fiber. This bundle maximizes transmission of excitation laser while allowing a sufficient number of data points for consistent PLPS measurements. The other was a 30,000 pixel, 790 micron diameter bundle rated for imaging applications. With this bundle, nearly continuous movement of the laser spot is possible, allowing for higher resolution measurement scans. Despite the larger void fraction, compared to the first bundle, transmission is sufficient for excitation of the TGO. Fig. 40 shows the spread pattern and size for the two bundle types along with a 1 mm scale reference.

Both fiber bundles use fused silica fibers with the cladding stripped off to minimize the dead space in the bundle area. The ends are polished to minimize coupling losses, however these bundles suffer from significant back-reflection, as no AR-coating was applied. Thus, despite a dichroic filter with a 685 nm threshold, 532 nm light from the excitation laser on the order of several mW passes on to the spectrometer and affects the PLPS waveform, as shown in Fig. 39. This back-reflection, however does not significantly interfere with the deconvolution of R1 and R2 peaks from TGO fluorescence due to the built-in baseline subtraction of the fitting routine. Reducing the back-reflection may be desirable for the signal-to-noise ratio of fiber bundle PLPS measurements. In low-signal measurements, the obscuring of the waveform due to signal noise can cause inaccurate deconvolutions of R2 peaks, leading to non-physical stress interpretations.

In Figure 39, the effect of baseline subtraction is shown for a chromium fluorescence spectrum collected via 30,000 pixel bundle during PLPS measurements on a factory-condition thermally-cycled turbine blade. Back-reflection from the fiber faces in a bundle may vary significantly, leading to waveform baselines of different curves. The baseline is defined by interpolating between two set spectrometer pixels, corresponding to wavenumbers of 14280 cm^{-1} and 14490 cm^{-1}, thus setting the boundaries for the curve-fitting domain. This domain contains the R1 and R2 chromium peak locations, with a sufficiently large margin to account for the likely spectral broadening. Each pixel intensity value in this domain is then reduced by a corresponding value interpolated between the intensities at the upper and lower boundaries.

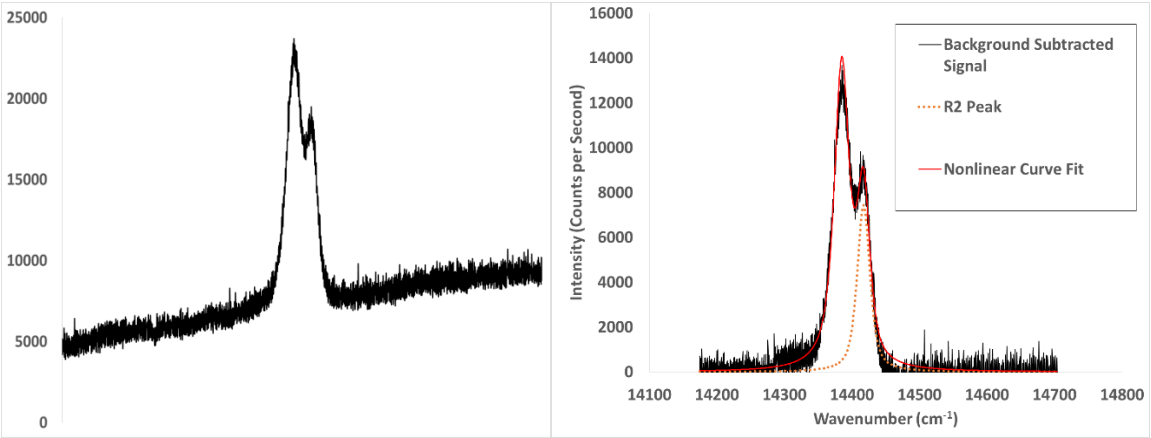

Figure 39: Demonstration of baseline subtraction for fluorescence spectra as applied to fiber bundle PLPS measurements. The collected signal from the 30,000 pixel bundle is shown on the left, with the baseline due to back-reflection, and the resulting pair of deconvoluted R1 and R2 peaks are shown on the right, after baseline subtraction.

Maximizing PLPS signal intensity is key to ensuring that the highest possible percentage of fluorescence collections can be properly deconvoluted into R1 and R2 peaks, and that the TGO stress values calculated incur minimal error. Signal collection was maximized by placing a 690 nm, 30 mW laser diode in place of the fluorescence target as shown in Fig. 16, and adjusting

the lens positions affecting fiber coupling for best signal return. The long-working-distance lens achieved a signal collection efficiency of 80%, and the transmission efficiency of the fiber bundles was on the order of 85%. With ~5% losses for each fiber coupling, the entire system had an effective signal capture efficiency of 61.37%. With a fixed optimal alignment, the fluorescence signal is directly related to excitation laser power.

The 532 nm diode laser from LaserGlo has a continuous wave beam power of up to 260 mW, but when controlled through a DAQ board, the average power is adjustable to as low as 70 mW. Operation at a power level of 157.3 mW caused burn damage when the excitation laser was focused onto a single 200-μm fiber such that the transmission efficiency for a single fiber was reduced to 35%. An 80/20 beam-splitter was installed to reduce the laser exposure experienced by the fiber bundle to 126 mW, a compromise between damage avoidance and TGO excitation. The reduced power allows operation of PLPS measurements without damage to optical fibers. However, even at this operating power, care must be taken to defocus the laser to a diameter of roughly 180 μm. A new fiber bundle was damaged when its fibers crossed the laser's focal plane during alignment, and the resulting efficiencies are shown in Figure 41.

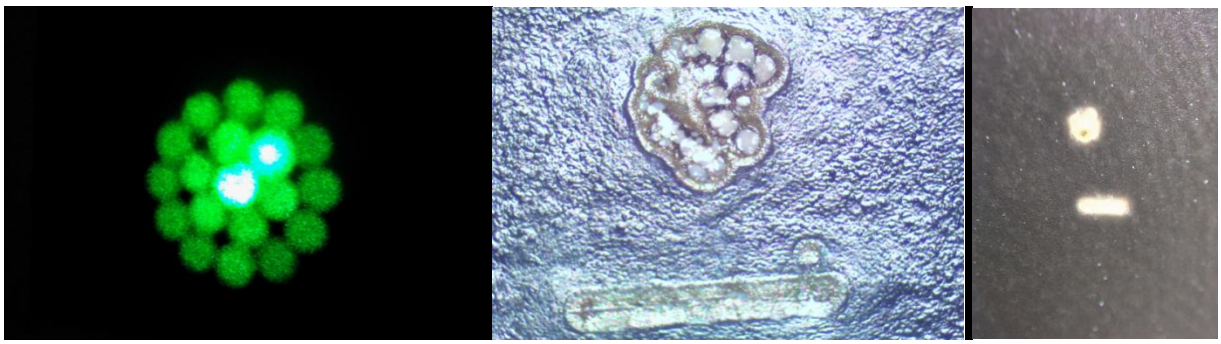

Figure 40: Pattern of 19-fiber bundle projected onto a screen (Left). Burn pattern on photo-sensitive paper showing the spread of interrogation points in the focal plane for a PLPS measurement using the 19-fiber bundle (Middle). The line below the pattern is 1 mm, showing that the measurement area will fill a typical LIBS hole. Burn pattern on photo-sensitive paper demonstrating the focal plane using the continuous fiber (Right).

These minor damages to the fibers have not caused a noticeable obstruction to PLPS measurements, with exception to the one fiber with below 40 % transmission. The effect is felt however, in that the laser power must be increased for low-efficiency fibers to collect signals with sufficient intensity for clear peak deconvolution. No evidence that the burn damage distorts or obscures PLPS signal has been found, as can be judged by the results in section 5.1.2. These damages during alignment were not incurred by the 30,000 pixel fiber bundle, since the proper alignment had been established before it was installed. However, it is expected that it would be at least as vulnerable as the large-fiber bundle, due to similar fabrication materials and its larger void fraction and significantly larger area covered by fiber-air interfaces.

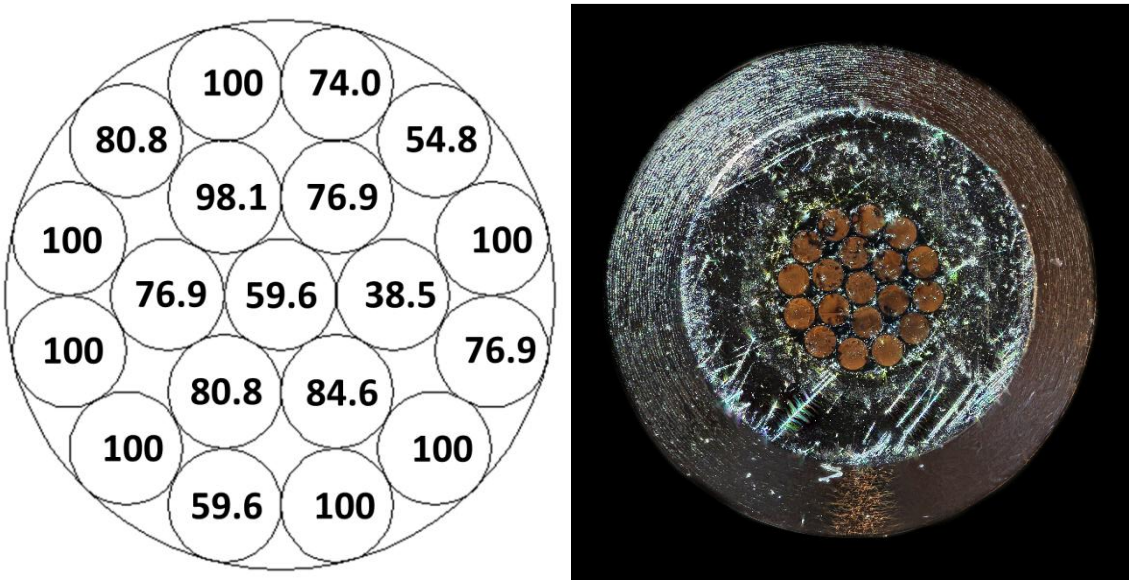

Figure 41: Transmission efficiency for each fiber in a 19-fiber bundle, normalized to 100 %. This fiber bundle was exposed to burn damage from intense focused excitation laser power. The same fiber bundle is shown on the right.

5.1.2 Reliability of Fiber Bundle PLPS Measurements

PLPS scans were performed on several components using both fiber bundles, as well as the standard collection method, to compare performance in stress analysis. A raster scan of 64 points was taken over the investigation area via motor-translated single-fiber measurements. To obtain a comparable stress distribution, a full dataset from both bundles were taken from each of three different locations within the same investigation area. For this comparison, shown in Fig. 42, the excitation laser power was held at a constant for all three collection methods. However, the spectrometer integration time was adjusted to the best performance for each method. For the fiber bundles, that meant a longer integration time to maximize signal strength, and for the standard technique the integration time was kept low to avoid saturating the spectrometer.

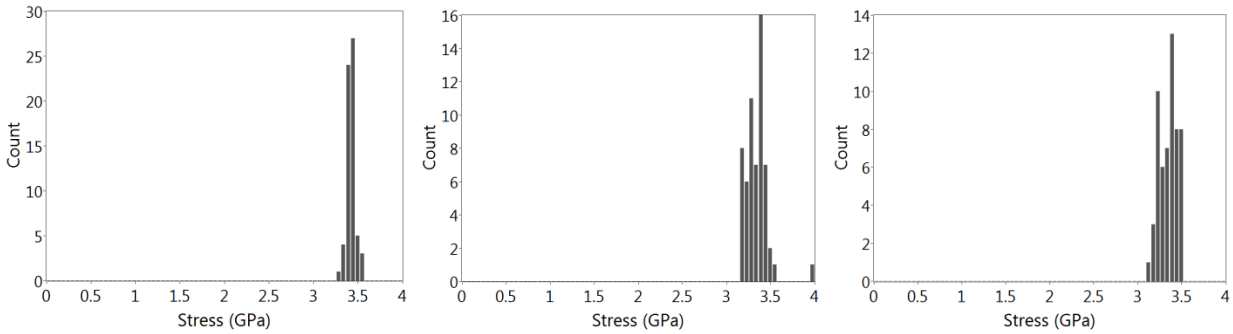

Figure 42: PLPS stress histograms taken from a thermally cycled bare TBC turbine blade. Left to Right: PLPS results from the standard technique, those using the 19-fiber bundle, and those using the 30,000-pixel bundle.

The first sample tested was a thermally-cycled turbine blade which had not been put into service, and hence was free from CMAS deposits. The results from this sample are summarized in Fig. 42, where the average stress measured shows strong agreement between the three trials. A scanning area of 0.36 cm^2 was used to collect the standard measurement data, shown on the left, and the three bundle probe locations were arranged in an equilateral triangle within this area. The

19-fiber bundle and the 30,000 pixel performed comparatively well, with standard deviation of stress values of 0.15 and 0.35, compared to the standard at 0.05. Stress measurements on this blade from previous trials show minimal variation, as in section 4.3.

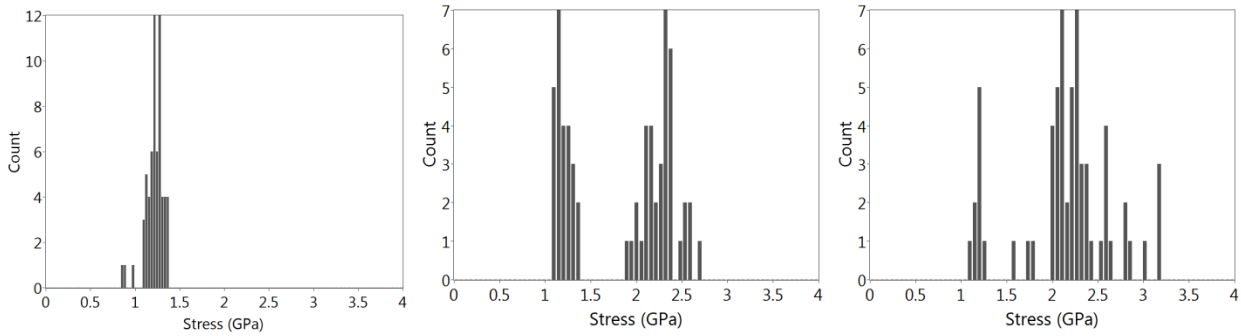

Figure 43: PLPS stress histograms taken from a thermally cycled button sample. Left to Right: PLPS results from the standard technique, those using the 19-fiber bundle, and those using the 30,000-pixel bundle

The second sample was a thermally cycled EB-PVD coated button sample provided by Rolls Royce. The sample had been cycled for 120 hours, as part of an experiment to re-create the stress-remaining life correlation referred to in section 4.3.3. Chromium fluorescence waveforms obtained from this sample approach the lower limit of acceptable signal-to-noise ratio, due to a lower effective TBC transmissivity compared to other samples. The results from this sample demonstrate the effect of this lower transmissivity on the fiber bundles, which have a lower collection efficiency than the single large-core multimode optical fiber used for the standard method. The effect of this condition is apparent in Figure 43.

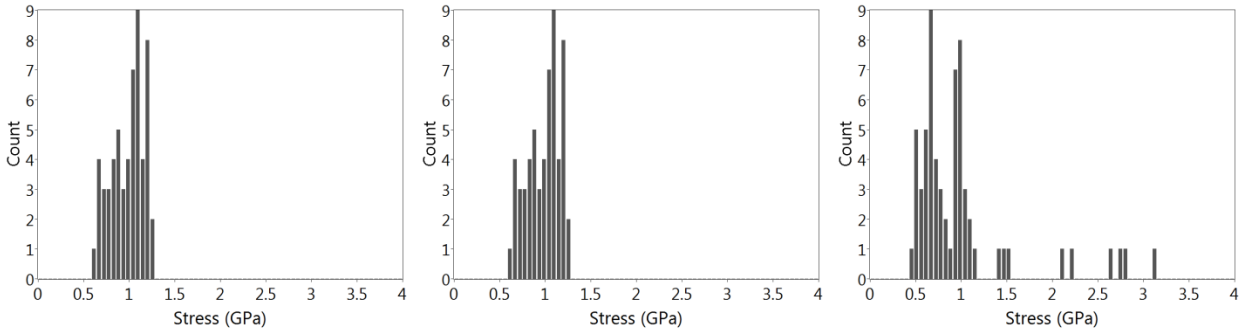

Figure 44: PLPS stress histograms taken from an engine-run turbine blade near failure. Left to Right: PLPS results from the standard technique, those using the 19-fiber bundle, and those using the 30,000-pixel bundle.

The stress histograms obtained from both bundles demonstrate agreement at the accepted value of 1.32 GPa, but also show a non-physical shift to higher stress for many data points. This stress shift is confirmed to be a result of poor signal fitting due to low signal-to-noise ratio, as described in section 4.3.2 and shifted values would normally be excluded by the merit value discrimination. The low merit-value data points are kept here to demonstrate the relative sensitivity of the fiber bundles to poor signal measurements. The 30,000 pixel bundle (far right in Figure 42-44) shows an increased susceptibility to low-intensity signal fitting errors, compared to the 19-fiber bundle, which benefits from increased signal transmission.

The third sample type investigated was an engine-run turbine blade which had been cleaned of CMAS using a scanning LIBS ablation routine, to expose an area of 12 mm^2 to be used as a site for PLPS measurements. An area of 4 mm^2 was chosen from within this ablation site for the raster scan used to obtain the standard method PLPS measurements. As before, three locations within this scan site were used for the measurement locations for both bundles, at each of which equally sized sets of data were taken. Figure 44 shows the results from this turbine blade, which is found to have a compressive TGO stress of 1.01 GPa, placing it in the near-failure regime of the TBC service lifespan.

The stress measurements obtained from the standard method agree well with those from the 19-fiber bundle, with histograms of comparative standard deviation and range. The stress measurements taken from this engine-run blade experience more variation over the scan area than do the factory-condition cycled turbine blade, as well as lower signal intensity. The 30,000 pixel bundle again suffers from higher fitting errors compared to the 19-fiber bundle, a problem which in this case is manifested in multiple high-shifted stress values, as well as a clearly bi-modal stress distribution.

5.2 LIBS Utilizing a Fiber Optic Waveguide

For the borescope adaptation of the current remaining life analysis technology, it is necessary to provide adequate CMAS removal for use in engine-run blades. Modifying the LIBS process to allow optical fiber delivery of pulsed laser power requires a waveguide which will sustain the intense instantaneous power density of the Nd:YAG. Flexibility concerns place a limit on the diameter of such a waveguide, which results in a high operational laser power per unit area. For transmission of UV laser radiation, fused silica waveguides are the best choice, but care must be taken not to exceed the damage threshold. The average power of a pulsed laser with repetition rate on the order of 10 Hz will not pose a problem for fused silica when operating at the pulse energies required for LIBS, but with nanosecond pulse lasers, the instantaneous power becomes a legitimate concern. Damage threshold tests were performed on the fused silica waveguides to determine the maximum pulse energy which could be transmitted. Transmission efficiencies of several waveguides were tested at pulse energies below their damage thresholds.

5.2.1 Fused Silica Waveguide Damage Thresholds

The ability of optical components to withstand laser exposure without suffering optical degradation or structural damage can be quoted several ways. Two of these are the energy density, or fluence, damage threshold, and the instantaneous power density damage threshold. For applications which involve large amounts of laser power, such as laser welding or laser drilling, the average power is of greater concern. This is especially true of long-pulse and continuous wave lasers, which cause thermal damage. For short laser pulses, including the nanosecond scale in our LIBS system, high instantaneous power density causes optical breakdown (Kamensky, et al. 1998). The latter is relevant to failure modes of waveguides to be used for fiber-adapted LIBS experiments, and will be a subject of discussion in these results.

The energy density required for successful CMAS ablation with a 355 nm pulsed laser has been previously determined by Majewski to be in the vicinity of 26.0 mJ/mm^2 using a laser with a pulse duration of 14.0 ns, resulting in a power density of 1.857 MW/mm^2 With the current Quantel Nd:YAG laser used for LIBS, the pulse duration is shorter, at 5.22 ns. Here, the same optimal energy density for CMAS ablation results in an instantaneous power density of 4.98 MW/mm^2, which is, for example, over 7 times greater than the damage threshold for a high-energy pyroelectric energy sensor (ThorLabs ES220C), and over 60 times the damage threshold of the ES120C model in service during this study.

Since the input laser pulse at the proximal end of a waveguide will necessarily be equal to or greater than the energy of the output pulse, the damage thresholds of the waveguides become a concern. Assume a desired ablation spot size of 0.6 mm diameter, a value which is approximate for the updated analysis system. To meet the required energy density for CMAS ablation, the

pulse energy would have to be at least 7.35 mJ. For a nominal waveguide diameter of 1.0 mm, with a cross-sectional area of 0.785 mm^2, this same pulse energy would deliver an instantaneous power of 1.79 MW/mm^2 on the fiber surface.

The instantaneous power density damage threshold of fused silica is quoted on the order of 10^{11} W/cm^2 (Galt, 2013) at least a factor of one hundred higher than the typical instantaneous power for our experimental setup. However, these figures may not be applicable for two reasons: first, the damage threshold is quoted for infrared laser at 1064 nm, whereas our system uses UV at 355 nm. There may be differences in the coupling efficiency of silica molecules with UV laser with infrared laser which translates to higher damage at lower energies with UV? The second reason is that the calculated power density of our laser pulse implies even distribution of the laser energy across the beam area. This would not be true even if the far-field beam energy profile was a smooth Gaussian shape, which is not the case for the Nd:YAG (Refer to Section 4.2). The heavy concentration of beam energy in a small point in the far-field causes the maximum local energy density to significantly exceed the bulk area figure.

In addition to these causes of optical breakdown, surface imperfections and contaminants can initiate breakdown on a surface such as a fused silica fiber, at energies below the damage threshold [citation]. Examples of this could be scratches on the fiber surface, or dust from the ambient atmosphere. Small-grit particles with high hardness, such as alumina, are capable of causing deep scratches in the silica surface. Precautions to be taken for optical fiber surfaces at risk of laser-induced damage include surface cleaning to remove contaminants and if necessary, polishing to reduce surface variations.

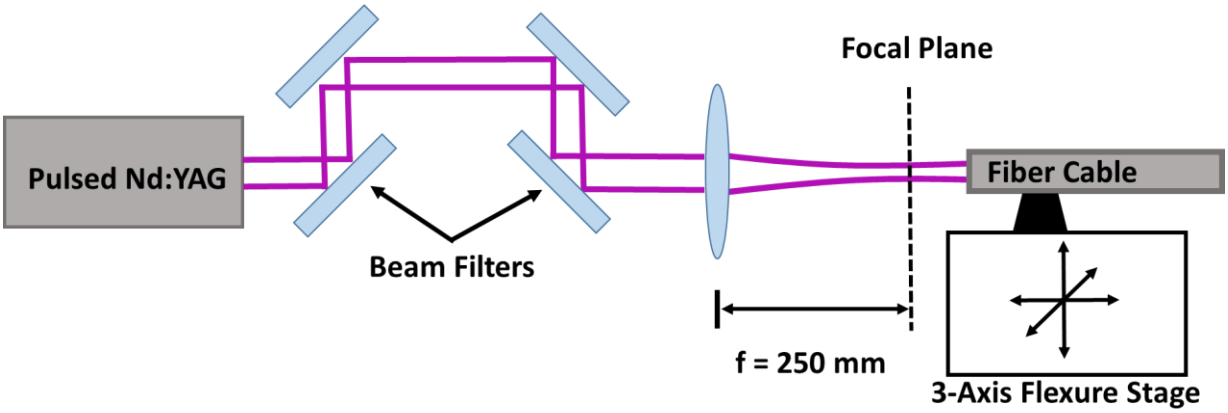

Figure 45: Schematic for fiber coupling a frequency-tripled pulsed Nd:YAG to a large-core fiber optic waveguide.

When coupling the high pulse power laser to a fiber optic, the beam was focused such that its diameter filled the fiber core diameter. A short focal-length plano-convex lens, such as 100 mm, was found to produce atmospheric optical breakdown at the beam waist, when used to focus the laser beam with pulse energy near 20 mJ. A 250 mm focal length plano-convex fused silica lens did not produce atmospheric breakdown within the operating range of laser pulse energy, and was substituted for coupling the pulsed Nd:YAG to fiber optics (Fig. 45). The final consideration for fiber launching was adopted in response to internal focusing of the LIBS pulse within the waveguide. During threshold tests, initial damage was observed behind the fiber face, even at pulse energies which had no damaging effects on the fiber face. The location was found to correspond with the focal plane extended by the focusing lens. To prevent this internal focusing of pulse energy, the beam waist was placed before the fiber face, such that the beam expanded to fill the fiber core diameter, rather than converging.

5.2.2 LIBS Waveguide Performances

The first waveguide tested for laser-induced damage threshold (LIDT) was a 910 μm core diameter fused silica multimode fiber optic patch cable with step index silica cladding giving it a numerical aperture (NA) of 0.22. The cable was SMA 905 terminated on both ends with a standard stainless steel ferrule. This cable was used for the initial trial, with the focal plane of the focused pulsed laser located near the fiber face. Laser power was increased steadily from 2 mJ to 20 mJ, while monitoring for transmission loss. The result was catastrophic failure via dielectric breakdown, as shown in Fig. 46. The previously mentioned precautions would be implemented after this case, and the results here are shown for reference. In this scenario, the power density was sufficient to overcome the damage threshold of the fused silica fiber at its surface.

This same fiber optic cable was stripped of its protective coating and cleaved after the connector ferrule. No damage had been experienced beyond this point and the remainder of the fiber was intact. The cleaved surface was ground flat using an abrasive diamond blade Dremel attachment to remove macro-scale irregularities and any running cracks. This method replaces the typical procedure of diamond-scribing under tension, due to the large diameter of the fiber. The resulting surface was further prepared via mechanical polishing with a series of successively finer grit silicon-carbide lapping sheets, ranging from 1000-grit to 2500 grit. After treatment with the silicon-carbide sheets, another sequence of polishing was performed using fiber-polishing sheets with grit size ranging from 12 microns to 0.3 microns. The surface was then cleaned of abraded debris with methanol-soaked lens-cleaning tissue.

After the new surface had been prepared, the fiber cable was tested for transmission efficiency, having taken all the aforementioned precautions to prevent surface damage. The pulse

energy was increased from 3.9 mJ to 14.54 mJ, at which the transmission efficiency dropped immediately, and after 120 laser pulses, the optical fiber suffered complete transmission loss. The damage to the fiber was observed to be at the fiber-cladding interface, and not in the fiber core itself. The location of the damage was where the expanding laser beam would be expected to make its first reflection from the cladding.

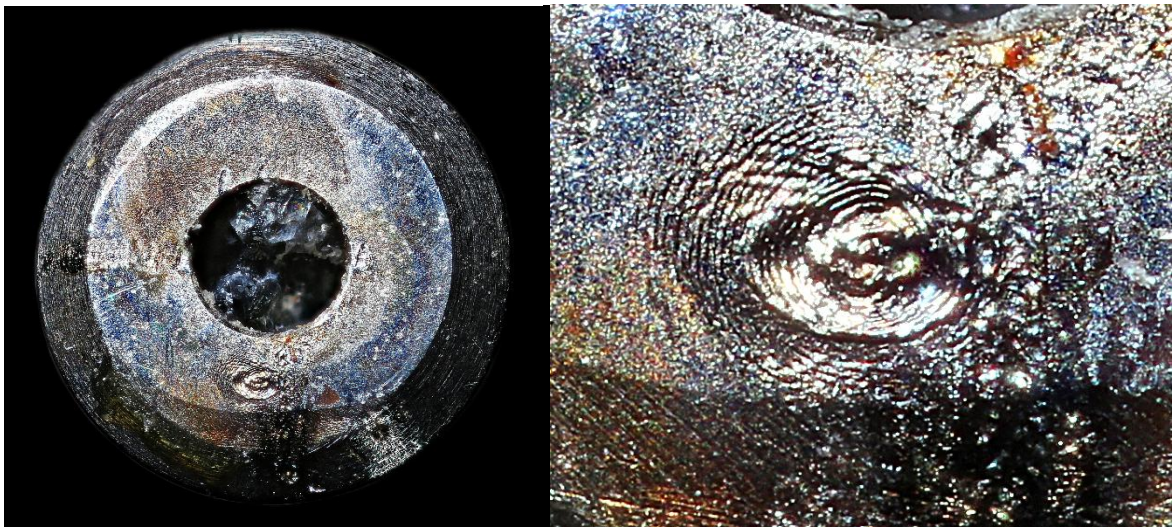

Figure 46: Damaged 910 micron diameter single silica fiber after thermal shock damage from pulsed Nd:YAG (Left) The beam profile of the pulsed laser is evident in the zoomed image on the right, with the damage concentrated in the center.

Figure 47 describes the transmission efficiency for the step-index fused silica fiber cable, and its breakdown between 13 and 15 mJ. The apparent discontinuity of transmission efficiency near a pulse energy of 6 mJ is an artifact of the energy sensor used, and has no bearing on the trend line. The maximum safe pulse energy for this fiber type that can be determined from this test is 12.4 mJ, but to avoid damage from long-term exposure, a value of 10.25 mJ is used. With this pulse energy, the necessary energy density for CMAS removal can be achieved by focusing the beam to a spot of 0.7 mm in diameter.

A second large-core step index fiber was obtained for transmission tests. This silica-silica fiber had a core diameter of 1.0 mm, and was rated on a "best effort basis" by a LEONI representative for a power density of 780 MW/cm^2. The high power rating was facilitated by high-power-rated SMA connectors, with copper ferrule heat sinks and an air gap buffer to prevent direct damage to the fiber core. This fiber optic cable rated for high pulse energy was subjected to an energy ramp damage threshold test, as with the previous fiber cable. Total transmission loss occurred near a pulse energy of 14 mJ, with no visible damage to the fiber surface. The protective coating was stripped off to expose the cladding layer and the only damage found was inside the fiber, several centimeters behind the copper ferrule.

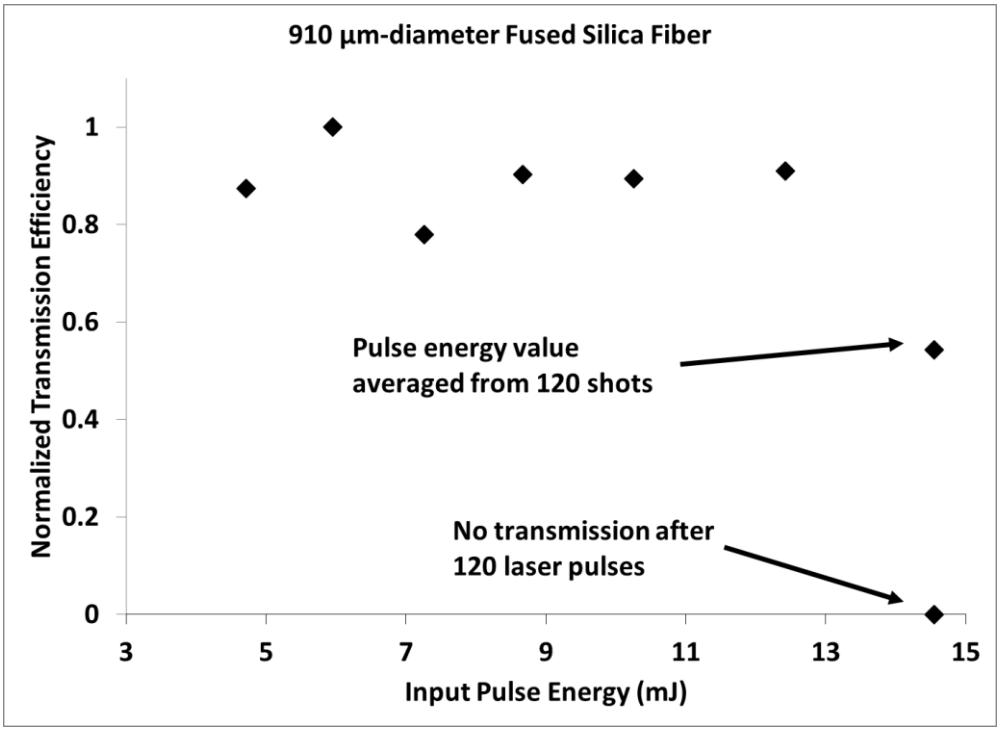

Figure 47: Transmission efficiency trend for 910-micron diameter step-index fiber optic patch cable with pulsed 355 nm laser. Efficiency drops sharply at a pulse energy of 14.5 mJ, and after 120 pulses, the transmission is immeasurably low.

The translucent nature of the cladding allowed optical inspection of the damage at the interface, which was structured in a thin ring spanning the circumference of the fiber. Again, as with the 910-micron diameter fiber, the location of the ring was not far from where the beam might be expected to reflect off of the cladding-core interface. No damage was observed to the remainder of the fiber. Returning to the same pulse energy of 14 mJ and exposing the fiber to prolonged laser fluence, additional damage rings appeared along the length of the fiber. In some cases the rings were thin, as with the initial damage, and in others they extended for several millimeters. Still the surface of the fiber was undamaged, suggesting that for step-index silica fibers such as these, the limiting factor on pulse energy transmission involves some thermal effect at the cladding-core interface.

Hollow waveguides fabricated from clear fused quartz were investigated as potential alternatives to the step-index silica-cladded fibers. The tubes tested had inner diameters ranging from 1.0 mm to 2.0 mm, with wall thicknesses of either 0.5 mm or 1.0 mm. These were tested to attempt circumvention of damage to the LIBS waveguide by exploiting air as the optical medium. When exposed to laser radiation, these quartz tubes allowed the loss of the majority of beam energy, and it is conjectured that the bulk of transmitted energy came from photons whose trajectory passed straight through the annulus without redirection. Hollow waveguides have been successfully used in the past for high pulse-energy transmission (Matsuura, Parry) but the capillary tubes had been treated with an internal dielectric or metallic coating.

Large diameter clear fused quartz rods were also investigated as a lossy waveguide alternative for fiber LIBS. The implication was that despite losing energy along the length of the waveguide, the pulse energy on the distal end would be sufficient for laser ablation. Rods of 1 mm and 2 mm diameter were subjected to transmission and damage threshold tests. The

transmission was lossy, with the efficiency decreasing as a function of waveguide length. Optical inspection during a dark-room test showed continuous leakage of UV light along the entire length of the waveguide (Fig. 48). The maximum energy transmitted was found to be 78.66% at low pulse energies near 1 mJ for a 30 cm section of the 2 mm diameter rod. However, transmission decreases as a function of waveguide length, and with an 85 cm section of the same rod, no measureable transmission was found at that pulse energy.

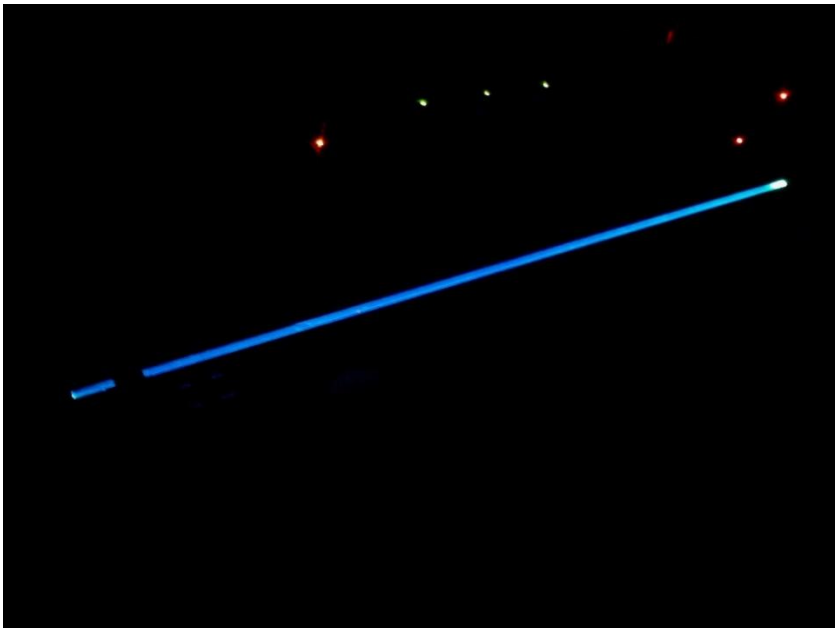

Figure 48: UV leakage from a 30 cm section of a clear fused quartz rod in a dark room

The damage threshold for the clear fused quartz was observed at a pulse energy of 16.71 mJ. After several seconds of exposure at this energy, optical breakdown was initiated at the polished surface of the rod. The quality of the polish has a limiting effect on the laser intensity that can be transmitted without surface damage. The exposure was allowed to continue, and the surface of the clear fused silica rod was ablated away at a steady rate. The depth of the ablation crater was allowed to reach several millimeters, at which point the rod was inspected for

structural damages (Fig. 49). Optical inspection showed no damages to the rod beyond the deepest extent of the ablation crater. The fiber was cleaved and re-polished after the damaged portion, and transmission tests showed no loss in performance. This suggests that the solid rod may have the operational benefit of its lack of damage propagation.

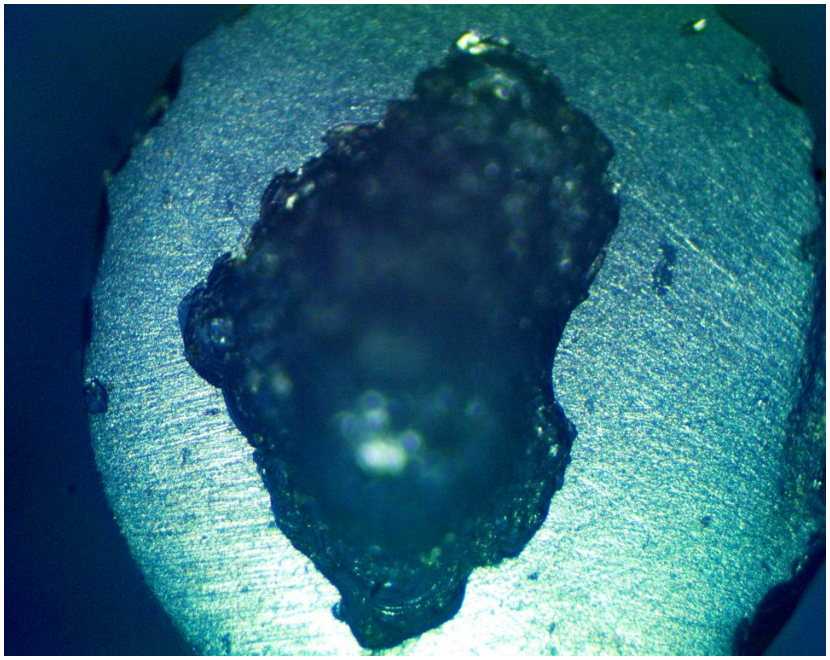

Figure 49: Optical microscope photograph demonstrating the ablation crater in a clear fused quartz rod after exposure to 355 nm laser with intensity exceeding the rod's damage threshold.

By focusing the beam to an extremely small point (~0.2 mm) it may be possible to concentrate the transmission energy from the solid clear fused quartz rod to induce plasma formation on a CMAS target. The indices of refraction for air and silica imply a numerical aperture of 0.689, which makes collimation somewhat difficult to achieve within the range of UV lenses readily available. If flexibility of the waveguides remains an important feature, then the large-core hollow waveguides and clear-fused quartz rods will need to be replaced with more flexible alternatives. The step-index fibers with doped silica cladding were shown to have a lower damage threshold, but significantly higher transmission. With transmission of over 10 mJ

of energy, it seems very possible that target ablation is possible using one of these step-index optical fibers.

To achieve the necessary energy density for ablation on the LIBS waveguide distal end, a lens combination for collimation and focusing of the beam should be attached to the fiber. Depending on the waveguide chosen, the NA of the output beam (0.22 for step-index fiber optic cable, 0.69 for uncladded silica waveguide) will dictate the optics to be used. For the fiber optic cable, a 35 mm focal length plano-convex UV lens will collimate the output beam at an approximate diameter of 2 cm. From that point, the beam can be reduced in diameter to 0.2 mm by a 7 mm focal length lens. Alternatively, fused silica half-ball lenses or graded-index (GRIN) lenses, available in diameters of 1.0 mm, 1.5 mm and 2.0 mm, can be attached directly to the fiber cable for collimation and focusing. A custom microscope objective for the borescope, such as one proposed for coherent anti-Stokes Microscopy (Rim, 2010) would greatly facilitate the fiber-based LIBS process, while providing integration with the PLPS fiber bundle.

6 Laser Ablation Thermal Barrier Coating Removal

Efficient removal of CMAS from the surface of the TBC topcoat has been achieved utilizing laser ablation with depth control provided by real-time spectral recognition of the coating system's constituent species. Extending this same method to remove the YSZ topcoat would provide an alternative to methods such as chemical dissolving. The key advantage to a laser ablation coating removal scheme is the ability to retain the bond coat layer, thus conserving materials such as platinum, and reducing the labor and time required for re-coating. The variation of TBC thickness over the surface of a coated substrate necessitates an adaptive ablation based on identification of the shallowest layer to be preserved, in this case the bond coat. A catalogue of LIBS spectra for each species in the coating system provides the necessary references to distinguish between these layers, and application of single value decomposition methods to these spectra serves to create a distinct spectral transition at the interface depth. Implementing a threshold composition level for bond coat allows a continuously scanning ablation routine to uncover the desired sub-layer without causing undue damage.

6.1 Orthogonal POD Modes for LIBS Spectra

As shown in section 4.1, the advantages to a set of orthogonal modes representing the constituent species of a LIBS sampling over simple cross-correlation include more consistent and meaningful representations of a sample's chemical composition. For removing CMAS from TBC topcoat, this method improves the completeness of CMAS ablation, but for locating a narrow layer of bond coat underneath hundreds of microns of YSZ, it may make the difference between obtaining a measureable signal or not. Orthogonal modes representing the coating system's species are obtained from a large data set of low-noise LIBS spectra. A single LIBS sampling will provide sufficient information about the species' spectrum, however there will be some

obfuscating effect from the system noise levels. If sensitivity to noise is significant, then blocking out all ambient light during collection is one precaution that has been taken, but improving the signal-to-noise ratio for a representative LIBS spectrum requires the averaging of multiple collections.

6.1.1 Coating Species LIBS Spectra

For LIBS collection from a single sample, the sample was translated at constant velocity across a preset target area while the focused laser spot remained fixed. Collections over a 1 cm^2 area of a chemically pure sample of TBC were taken for the YSZ reference, as negligible variation in the LIBS spectrum is observed between samples of the same topcoat. The same procedure was employed for obtaining an averaged reference of CMX-4 super-alloy from a bare stator-vane. A bond coated turbine blade was subjected to several dozen individual LIBS measurements. The thickness of the bond coat is small enough that in order to avoid contamination of the signal with that of the underlying super-alloy, only the spectra resulting from the first laser pulses of each sampling were used. These spectra are shown in Fig. 50.

6.1.2 Proper Orthogonal Decomposition of LIBS Spectra

As briefly discussed in Section 2.5, POD for a dataset will choose orthogonal modes such that the least squared difference between each mode and a corresponding datum is minimized. These orthogonal modes in a linear combination weighted by their respective mode constants for a given snapshot will completely represent every spectrum vector in the data set. The behavior of POD modes are dependent on the manner in which they are developed. One method is to leave the POD modes unconstrained, and allow them to be developed naturally from the analysis of the

data set to be decomposed. This will ensure that the POD modes obtained from a true basis for the span of the vector space in question (in this case, an array of LIBS spectra as develops during a drill through TBC). The unconstrained modes will be orthogonal to each other in the basis, and guarantee a perfectly satisfied representation of the data set.

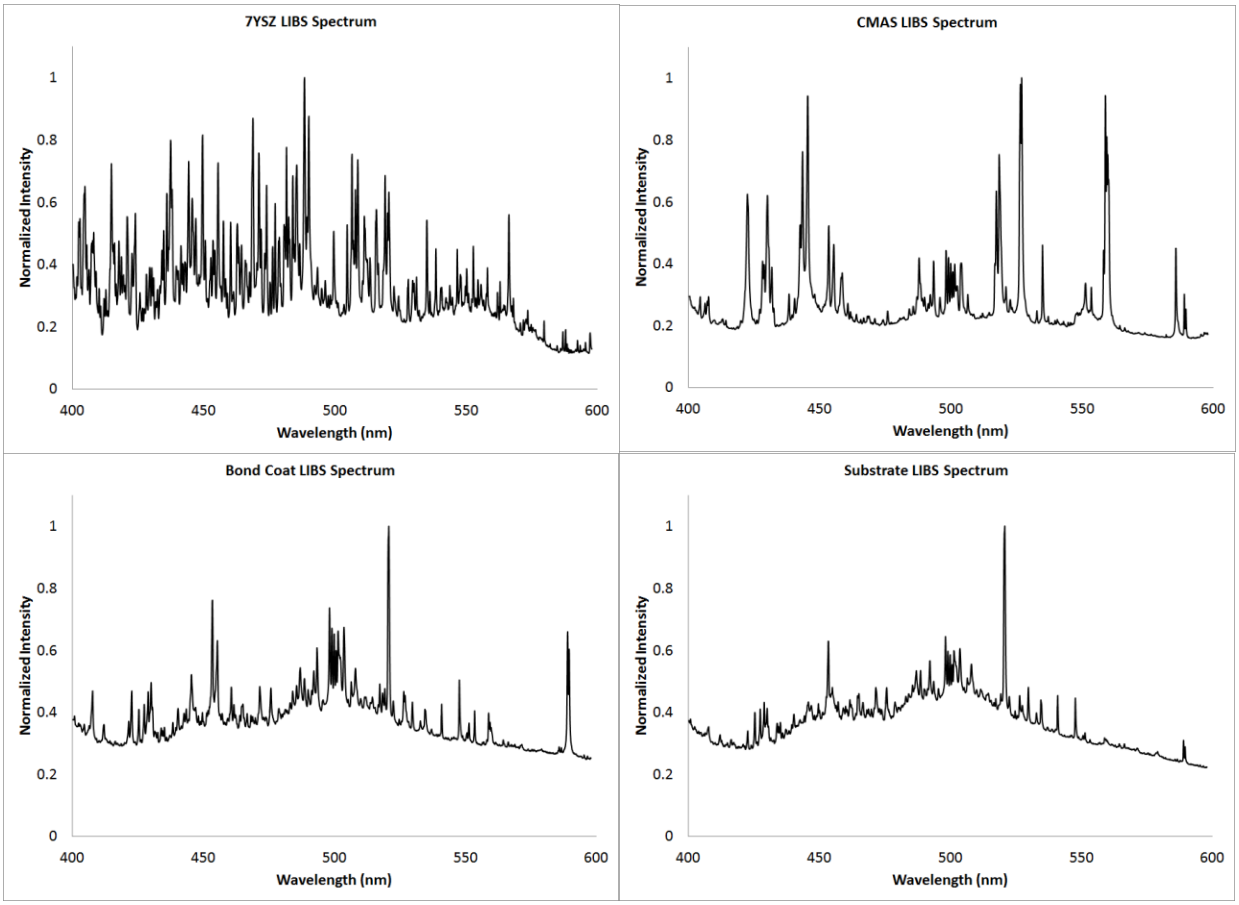

Figure 50: High signal-to-noise ratio reference LIBS spectra for coating system species. 7YSZ topcoat (Top-left) is characterized by numerous Zirconia peaks. CMAS (Top-right) is dominated by Calcium and Magnesium oxide, with some Alumina contribution. The Bond Coat (Bottom-left) and the CMX-4 substrate (Bottom-right) are distinguishable mostly by the differences in relative intensities of alumina and nickel peaks.

However, with unconstrained modes, it is possible for physical representation to suffer, especially if certain species are small in regards to their total contribution integrated over the length of the data set. In this case, one mode may represent a mix of two layers in the TBC

system making physical interpretation of the data difficult. Since the bond coat contributes very little to the total variance of a data set from LIBS drilling, it tends to be represented in the POD decomposition mixed with other modes such that it is necessary to choose another method.

This alternative method develops modes from a data set composed of many pure sample LIBS spectra, with equal representation from each species for which an orthogonal mode is desired. These modes are then 'forced' into the POD routine for deconvolutions of LIBS signal, guaranteeing the representation of each species. It must be taken into account that the singular value corresponding to each mode shape is determined by the contribution of that mode to the entire variance of the data set. In order to ensure that each species is given equal consideration, the data sets of reference spectra for each species must be of equal size. These data sets were compiled from the averaged reference spectra discussed in Section 4.1.1, and included 100 spectrum vectors each of CMAS, YSZ, bond coat and superalloy. This provided four mutually orthogonal modes to represent all of the species of concern in the TBC system.

For TBC removal trials, the spectral contribution of CMAS is negligible at the depth at which the bond coat is found. In this scenario, it is not beneficial to include CMAS into the weighting of the POMs used for interface recognition. Reducing the data set to include only YSZ, bond coat and superalloy samples can allow for more accurate representation of the LIBS spectra in the vicinity of the YSZ-bond coat interface. This owes to the fact that though the POMs obtained have a one-to-one correlation with the species spectra, regardless of which species are included the reference data set, the relative mode energies for deconvolution of LIBS spectra during drilling may change with POMs formed in different ways. The data set of references for POM formation are chosen based on empirical performance.

6.2 Ablation Drilling Stop Criterion

The challenges associated with locating the Bond Coat during a laser ablation drill are three-fold. The first issue lies in the fact that for a given laser pulse intensity, the transition peaks for a resulting emission spectrum are far lower in intensity for bond coat than for YSZ, due in part to LIBS efficiency of those species, and also perhaps to the structure of bond coat. On average, the maximum LIBS signal intensity for metallic compounds such as the CMX-4 Super-alloy or a (Ni,Pt)Al bond coat are lower than that of YSZ by a factor of at least two. The second issue lies in the spatial characteristics of the developing ablation crater as a result of the Nd:YAG beam profile. In the quasi-far-field regime, this profile retains some of the concentric rings of alternating high and low energy density, as shown in Chapter 4, as a high concentration develops near the profile center. The significance of this profile is the uneven ablation across the crater diameter which, after several hundred pulses, exposes the bond coat while the majority of the ablation crater is still within the topcoat volume. This has the effect of masking the small area of uncovered bond coat with the majority of YSZ signal which is itself more intense per volume. The third consideration involves the non-zero correlation between constituent species' LIBS spectra, and is addressed by replacing the Pearson's correlation coefficient method with a POD method for obtaining representative mode shapes for each species.

6.2.1 Threshold Algorithms

An early attempt to apply a dynamic stop criterion for TBC ablation focused solely on the substrate signal, and made no attempt to preserve the bond coat, since the bond coat interface was not distinguishable. The cross-correlation between the LIBS spectra and a reference substrate spectrum was subjected to a running average over 50 pulses, and a baseline subtraction defined by the average r-value for substrate during the TBC ablation region of the drill, where r-

value is the cross-correlation coefficient defined in section 2.2.3. A window was defined to capture the rate of change of the cross-correlation coefficient, with the window's width determining the accuracy of the ablation technique. When at least 70% of the points in the window expressed a monotonic increase in the r-value rate of change, the threshold condition was considered satisfied, the application of this algorithm is demonstrated in Fig. 51.

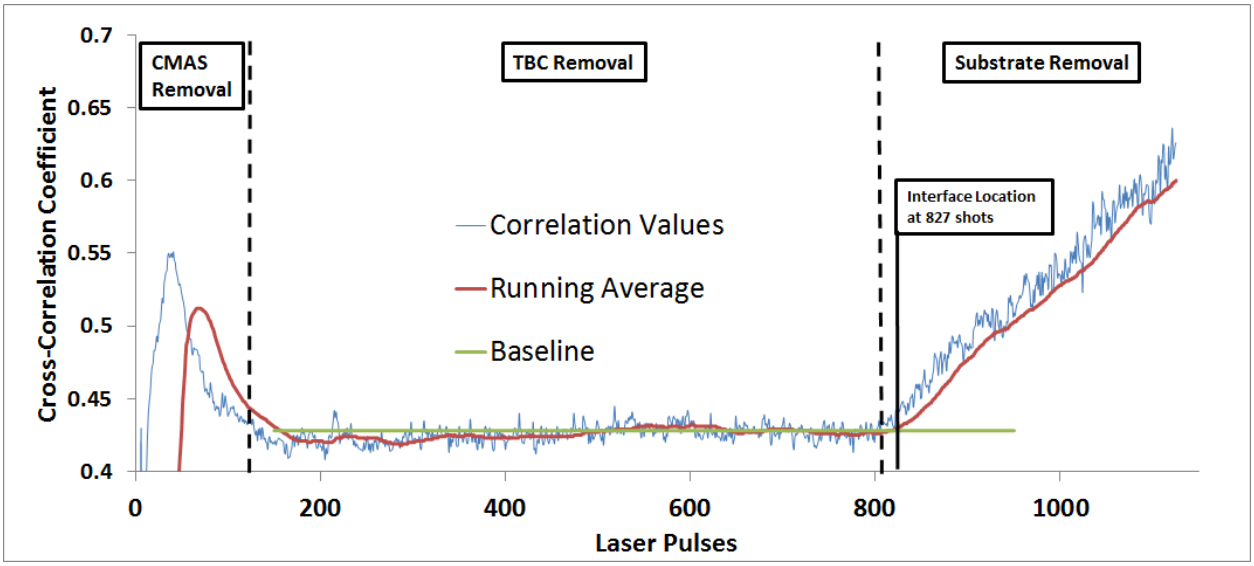

Figure 51: Visualization of a LIBS drilling sampling in terms of the Pearson's correlation coefficient for super-alloy substrate. Shown is the r-value (blue) the smoothed curve of the same (red) and the TBC-region baseline (green). The location where the threshold algorithm would cease ablation is denoted by a vertical solid line.

This method was relatively consistent for a number of drills taken over the surface of a turbine blade, however the depth control would still vary significantly on other samples. This was owed to the specifically tuned, and arbitrary, set of stop criteria employed. With a set of POD modes representing each species, it was possible to determine a robust threshold for bond coat signal. This is partially due to the now predictable behavior of species' mode constants as a function of drilling depth. As would be expected on a TBC-coated button sample, the YSZ composition is near 100% until the topcoat/bond coat interface, where it begins to decline. The

length and slope of this decline is caused by the quasi far-field beam profile of the Nd:YAG laser used for LIBS. The threshold limit is a bond coat mode constant of 1.5%, a value which was found to consistently remain above the noise levels, while providing as early a stop condition as possible. Using this limit, the detection of bond coat occurs ~20 pulses before that of the super-alloy by the same method, suggesting credibility of the technique.

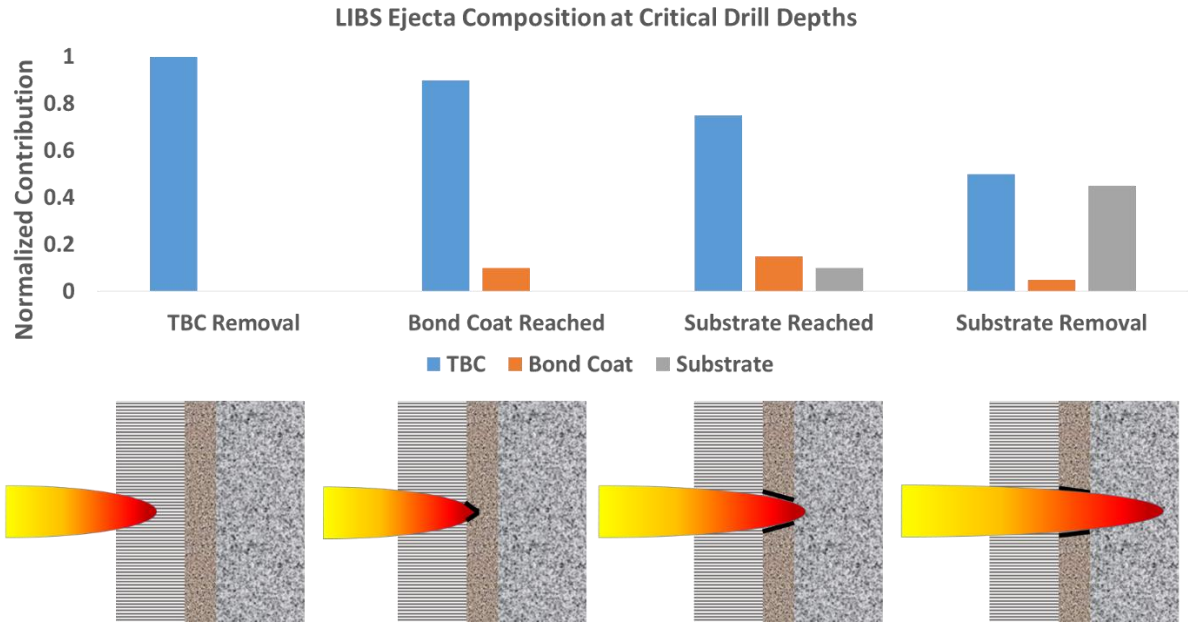

Figure 52: Physical interpretation of LIBS spectra as species concentration in the ejecta, and the corresponding crater shape. The beam profile is shown in terms of the amount of laser power incident on the target in each horizontal section.

Fig. 52 describes the effects of a Gaussian far-field beam profile on the LIBS spectra obtained during a drilling trial. The drilling rate decreases radially from the center of the ablation crater, such that crater depth as a function of radius becomes increasingly steep. The most obvious effect is that the contribution of YSZ to the LIBS spectra remains high until well after penetration into the superalloy substrate. The second effect is that the bond coat signal should

appear as a curve, broadened by the fact that it is similarly still exposed to laser radiation after it has been surpassed by the crater center, as shown by the black lines in the figure.

Another bond coat identification routine was developed by choosing the species reference spectra data set for POM formation to include only YSZ and bond coat. A second pair of modes were formed from a dataset of only YSZ and superalloy. This means that the superalloy and bond coat modes would not be orthogonal with respect to each other, but since the goal is to cease ablation before substrate is reached, this is unimportant. Figure 53 shows the mode profiles for the YSZ-bond coat and YSZ-superalloy pairs over the duration of a LIBS drill through TBC into the substrate. The behavior of the two pairs is similar, since the bond coat and superalloy share strong overlap in their nickel-aluminide composition.

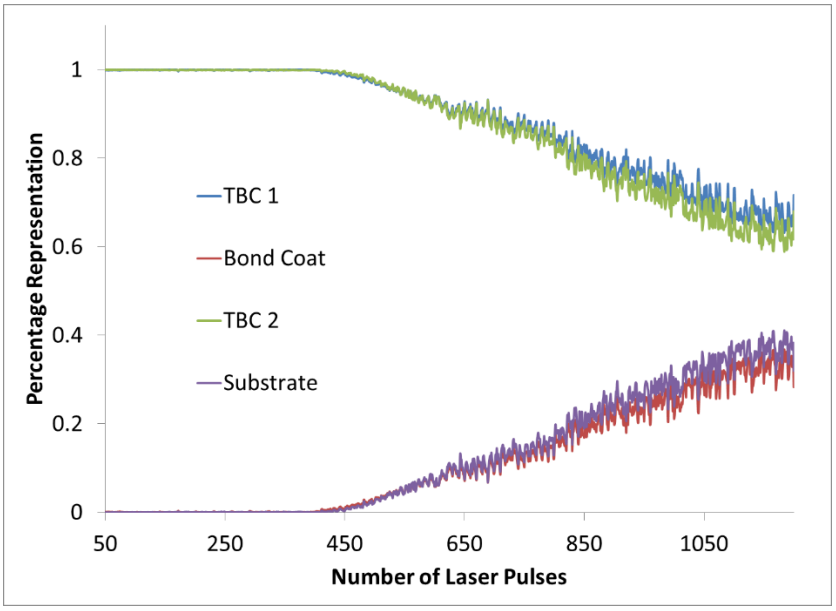

Figure 53: Mode constants for two sets of POD modes, one set which were developed from YSZ and bond-coat sample sets and another developed from YSZ and super-alloy sample sets. Clearly visible is the interface region where substrate is first exposed.

The reason this two-mode method shows promise is that although the bond coat and substrate mode profiles are similar, the bond coat mode consistently appears before the substrate mode during TBC removal. The discrepancy ranges from 20 to 40 laser pulses, with typical rates of increase for mode energies of 2.5×10^{-4} $shot^{-1}$. The locations of the appearance of the bond coat mode and the superalloy mode are designated by a threshold energy of 1.5 %. A typical result is shown in Fig. 54, from the same TBC drilling trial shown in Fig. 53.

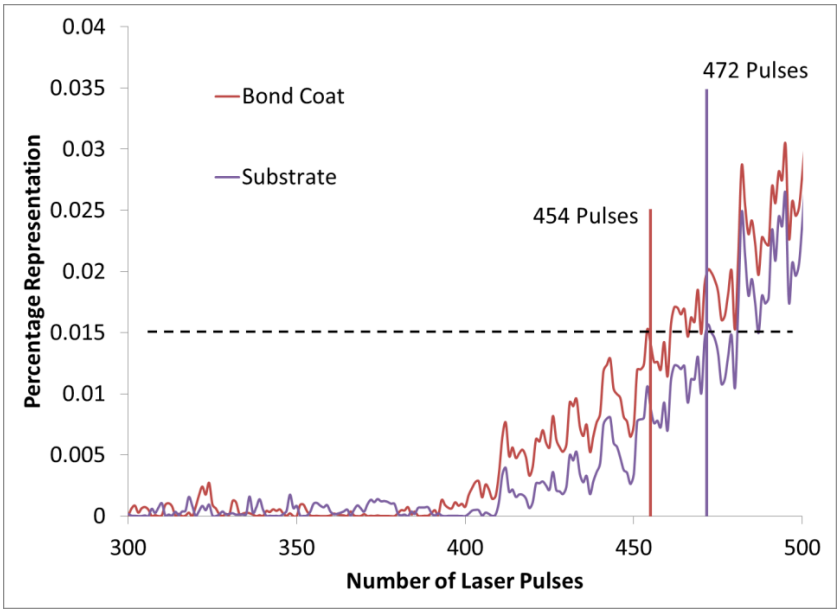

Figure 54: Comparison of the rise of the mode constants for bond coat and for super-alloy. Though the modes are visibly not independent of each other, the 1-to-1 correspondence between mode and species is maintained. The earlier rise for the bond coat may be indicative of discrimination between bond coat and substrate.

6.2.2 TBC Removal Drill Tests

Using the algorithmic stop criteria set based on the nickel mode profile, a series of craters were drilled into the coating of two different blades to determine ablation control consistency; the results are tabulated below. The projected overshoot column is a rough estimate of the

discrepancy between the location of the interface and the actual depth at the moment the stop condition is satisfied. A positive value for this metric denotes an overshoot, while a negative value denotes premature stoppage. Since the exact location of the bond coat is indeterminate until confirmation of its accuracy can be made, a proposed location was made by inspection of the mode profile over a full drill. The point at which the mode energy begins a monotonic increase in its averaged value was taken as the nominal interface location, and the difference between this nominal location and the stopping point dictated by the mode energy threshold was calculated as a percentage of the entire drill duration. The results for drilling tests utilizing this stop criteria set are summarized in Table 4 and Table 5.

Table 4: Drilling tests performed on the first of two turbine blades using the correlation curve fitting ablation control.

Trial #	Depth at Stop Condition (Pulses)	Drill Duration (Seconds)	Projected Overshoot
1	903	45.15	5.54%
2	1017	50.85	7.87%
3	1047	52.35	19.10%
4	992	49.6	10.08%
5	1124	56.2	16.01%
6	1236	61.8	7.28%
7	1167	58.35	8.57%
8	1077	53.85	16.71%
9	1061	53.05	6.60%
10	1310	65.5	3.82%
11	1180	59.0	2.54%
12	1310	65.5	2.29%

For the two turbine blades tested using the substrate-based algorithm, the TBC thickness varied relatively little in the chordwise direction extending from the trailing edge. An average thickness of 1100 laser pulses appears representative of the system under current operating conditions. The collective effectiveness of the stop criteria is repeatable and stable, with

exception to instances where system noise overtakes the signal. This noisy effect is greatly diminished with use of the POD modes, as shown in Fig. 53, due to the cleaner mode profiles.

Table 5: Drilling Tests performed on the second of two turbine blades using the correlation curve fitting ablation control.

Trial #	Depth at Stop Condition (Pulses)	Drill Duration (Seconds)	Projected Overshoot
1	1029	51.45	11.66%
2	917	45.85	-21.81%
3	1083	54.15	2.77%
4	1080	54.0	2.78%
5	1086	54.3	2.76%
6	1113	55.65	0.90%
7	1249	62.45	2.40%
8	1059	52.95	-9.44%

For the trials using the stop criterion described by Fig. 53, 54, drills on a TBC-coated coupon were terminated using the bond coat mode energy threshold of 1.5% of the spectral composition. As before, the physical bond coat interface is unknown, so the success of the stopping criterion was gauged by proximity of the ablation stoppage depth to a nominal interface location determined by inspection of the mode profile. A typical result is illustrated in Fig. 55. The inset graph shows a zoomed subset of the drill development where the mode energy threshold is first exceeded. The majority of these trials resulted in ablation stoppage at a consistent depth, suggesting recognition of the bond coat interface. In trial 5 and trial 6, fluctuations in the noise levels caused premature drilling stoppage, near 240 laser pulses, too far short of the average value for the other runs to be consistent with an interface location. The results for these trials are summarized in Table 6.

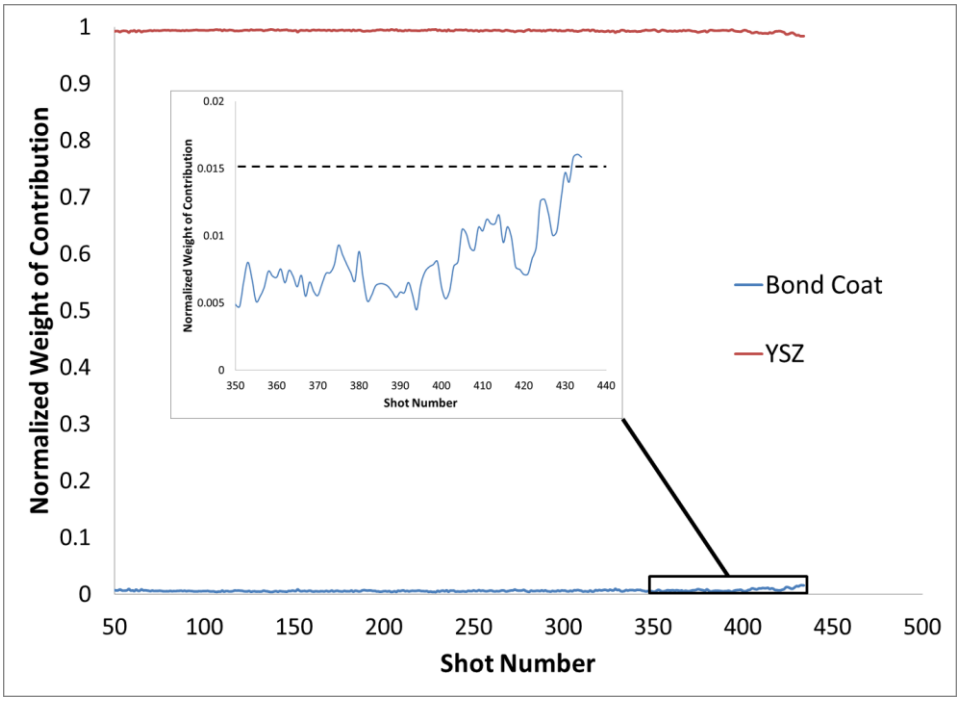

Figure 55: Example drilling profiles of the mode energies for YSZ (red) and bond coat (blue) until stoppage was imposed by the automated stop condition. At this time, it is difficult to distinguish between the stop location and the interface location.

Table 6: Drilling Tests performed on button sample using bond coat mode energy threshold for ablation control

Trial #	Interface location (pulses)	Drill Duration (seconds)	Outcome
1	389	19.45	Success
2	411	20.55	Success
3	400	20.0	Success
4	416	20.80	Success
5	246	12.30	Premature
6	233	16.65	Premature
7	412	20.60	Success
8	417	20.85	Success
9	411	20.55	Success
10	419	20.95	Success
11	410	20.50	Success
12	405	20.25	Success

6.3 Continuous Ablation

The effective laser-ablation removal of TBC is contingent on the ability to ablate evenly over a large area, while maintaining adaptive depth control. The near complete coverage of a turbine blade's pressure side is a short-term goal to demonstrate the plausibility of the application. Location of the bond-coat interface in real time utilizing a quasi-physical fixed threshold stop criterion allows for expansion of the drilling technique. The single crater drilling method was expanded by overlapping a series of craters to form a trough, as shown in Fig. 56. The overlap fraction needs to be greater than 50 % to create a solid line without border oscillations, however, to avoid ridges of overlap burning, the overlap must be even larger. Taking the limit as over-burn approaches zero requires an infinitely dense line of craters.

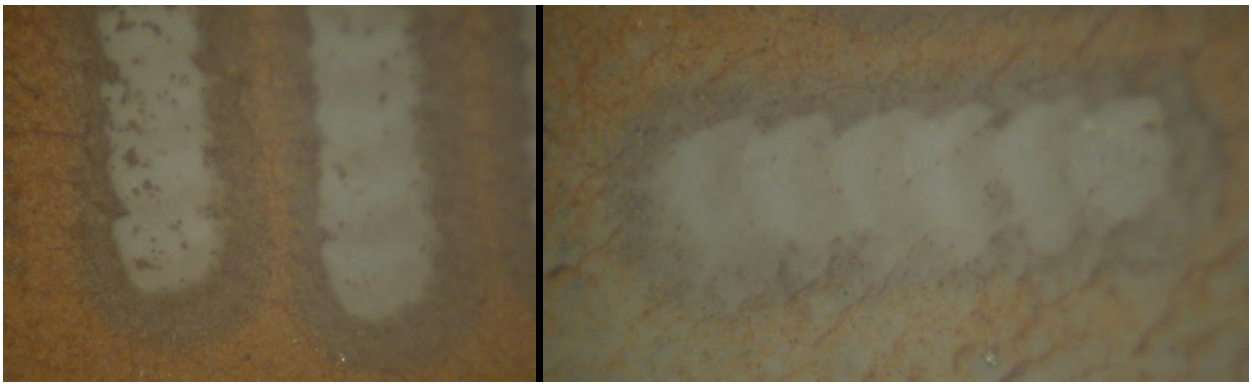

Figure 56: Examples of overlapping LIBS craters for CMAS removal, Apparent in the left photograph is the over-burn condition in the right column. The effect manifests itself as troughs and crests in the TBC depth as a function of position along the length. The other issue, demonstrated by the right photograph, is the oscillatory borders typical of using less than 50% overlap.

Since this is clearly not a time-efficient method for cleaning, the solution becomes a function of evenly wearing down each point in the trough. This is approached by the continuous translation of the target during ablation, as the focused ablation laser beam is held at a fixed location. The Nd:YAG laser's repetition rate of 20 Hz is matched against a target velocity of

0.80 mm/s, yielding a laser exposure rate of 25 pulses/mm for each scan. A mechanical shutter closes over every point which has passed the stop condition, preventing additional ablation. The very minimal over-burn effects from one line are quickly washed out by the next, and the result is a very clean removal along one dimension, as shown in Fig. 57. Two-dimensional scans are achieved by carefully overlapping line scans, a measure made necessary by over-burn encountered during 2-D scans introduced in Chapter 4.

The two-dimensional continuous scans were performed on CMAS-covered turbine blades, to quickly determine any problems which would propagate when the drill extended deeper through TBC. The patterns tested included several shapes for scanning the laser across the surface named raster scans, snake scans, frame scans and a figure eight designed to optimally clean a large single spot. In every case the cause of over-burn is due to excessive dwell during transition between motor controls. This dwell has a minimum duration of hundreds of milliseconds, limited by the USB event sequencing protocol in Windows, as well as the difficulty in true parallel handling of tasks in LabVIEW. To overcome this over-burn, a mechanical shutter can be employed to pause ablation during the transitional period. Regardless, the method of overlapping lines works remarkably well for CMAS removal, and may be sufficient for initial evaluation of the potential for TBC removal.

6.3.1 CMAS Removal

The precursor to testing the ability to remove TBC topcoats via laser ablation was to test the same for CMAS removal. The single-crater cleaning necessitated for PLPS measurements is tightly constrained for the best performance on a variety of CMAS. Extending this to the ability to clean a large region was made possible by altering the constraint parameters. As described in

section 4.1.2, the original depth control for CMAS removal was based on the derivative of a logarithmic fit of the Pearson's correlation coefficient between the captured spectra and a sample spectrum for YSZ. Relaxing the stop condition was achieved by increasing the derivative cut-off value to above the typical operational value of 0.007 $shot^{-1}$, as implemented by Lake.

Using the logarithmic fit brings with it a great deal of inconsistency when applying the ablation routine to samples with different CMAS deposits. The variation of thickness and composition of CMAS, as well as its hardness, depends on factors which can be considered unpredictable from the perspective of a maintenance facility. For some instances, the stop condition performed extremely well, in terms of even cleaning, and for other instances, the CMAS removal was uneven and incomplete.

Despite the variability of CMAS consistency and composition, the reference spectra composed from thousands of LIBS samplings is robust in terms of representing CMAS from a range of sources, each with their own unique blend. Using the orthogonal modes composed from POD analysis of YSZ and CMAS sample sets, it is possible to set a fixed stop condition for cleaning which performs equally well for each sample of CMAS. What enables this is the fact that the signal intensity from various specimens of CMAS, as measured by a fixed LIBS system, is nearly invariant, due to the domination of CaO and MgO signals. Thus a fixed composition threshold is applicable, since the end-state is the only important outcome, and any path-dependent effects which would derail a logarithmic fit are rendered irrelevant.

The scanning Results for CMAS removal using continuous scanning laser ablation in parallel with LIBS spectra deconvolution are promising. Ablation is very even across the treated section and any residual CMAS islands are sparsely spaced, with maximum diameters on the

order of 200 microns. This is in contrast to single-crater LIBS holes which can have large CMAS residual patterns. The rate of CMAS islands for continuous scanning and single crater methods is apparent in Fig. 57, which shows examples of both on a single engine-run turbine blade. PLPS measurements taken from within such holes are unimpeded by CMAS interference, and easily achieve high-quality TGO fluorescence signal, as the results in Section 5.1.2, for example.

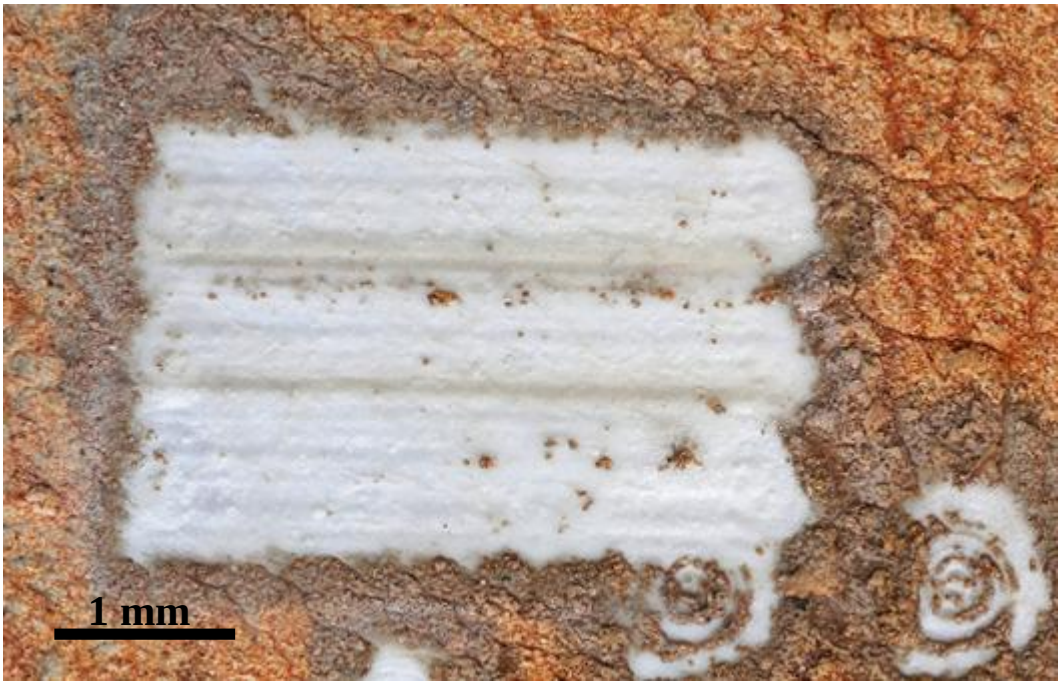

Figure 57: Demonstration of continuous 1-D LIBS ablation scans for CMAS cleaning of an engine-run turbine blade. The issues of over-burn and under-lap are minimized. The bottom right corner shows a few single-crater LIBS craters, and the CMAS residual patterns which interfere with PLPS measurements.

6.3.2 TBC Removal

To implement this continuous ablation technique for a method of TBC removal, it is necessary to take into account effects of the current beam profile which cannot be alleviated with manipulation of the operation parameters, as is the case with CMAS cleaning. The quasi far-field domain which is implemented for LIBS ablation causes the concentration of a large portion of

the pulse energy into a small region near the beam's center. Because the majority of the beam energy is distributed elsewhere, it may not be feasible to exploit this concentration in a productive manner, as the result is inevitably uneven ablation profiles.

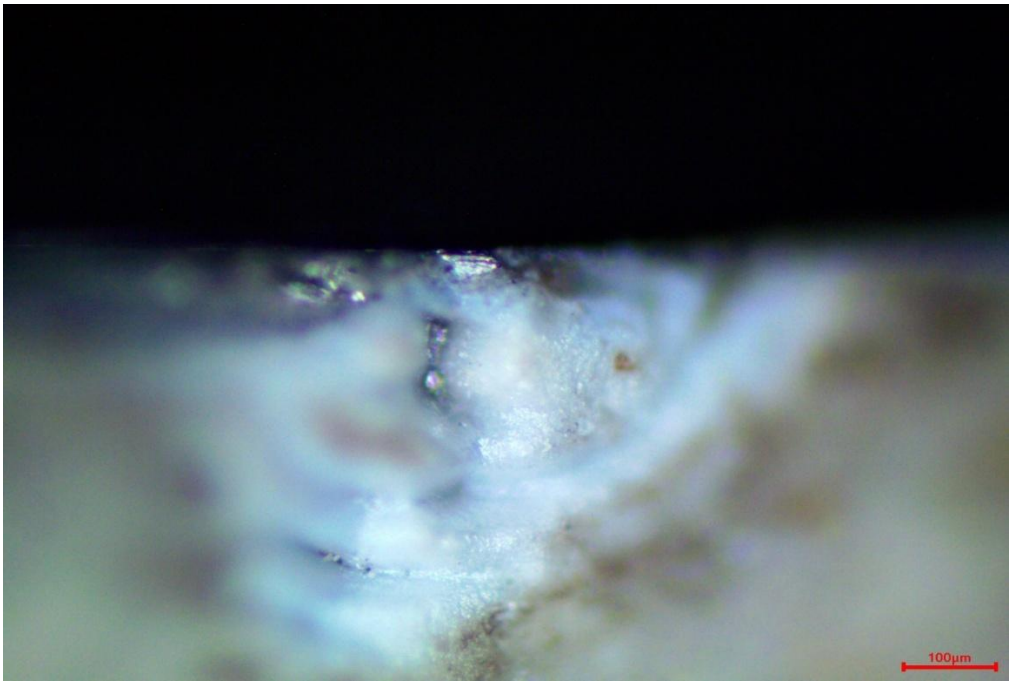

Figure 58: Optical microscope photograph of a turbine blade sectioned through the diameter of a TBC removal ablation crater. The microscope is focused to the center of the hole, and the depth from the TBC surface to the interface is evident. The region of high-concentrated pulse energy (shown in the center of the ablation crater) is on the order of 50 microns in diameter. Other regions of complete and incomplete TBC removal are evident.

The developing ablation crater profile deposits energy unevenly, demonstrated in Fig. 59, causing the formation of residual TBC structures within the crater center. By the time bond coat, or even the substrate is reached, the topcoat has not been worn down very much in some areas. Translating the target in the aforementioned scanning LIBS drill eliminates the variability of ablation rate in one dimension. This uneven drilling is clear in Figure 58, which shows the effect on drilling that high concentration of beam energy on the centerline has.

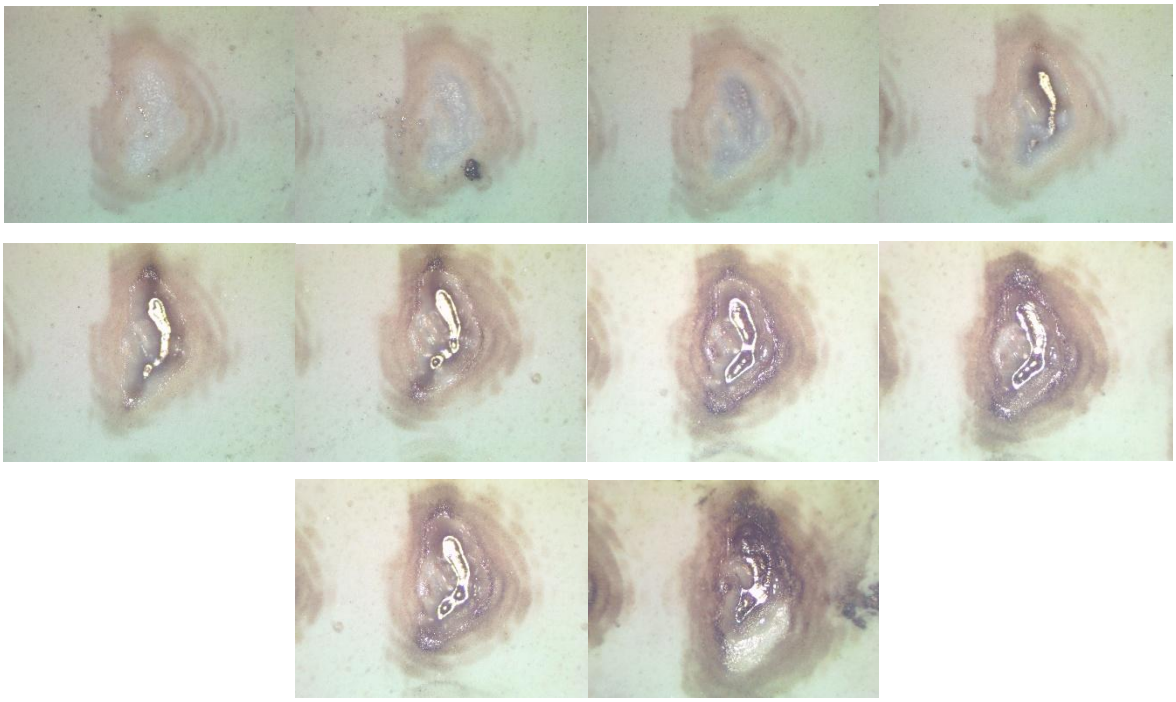

Figure 59: Development of ablation crater with depth during a drill through TBC: Top left to bottom right, ablation craters in a TBC-coated button sample after 100, 200, 300, 400, 500, 600, 700, 800, 900 and 1000 laser pulses. For the topcoat thickness of the sample tested here, the complete ablation of TBC occurs between 300 to 400 laser pulses at the deepest point of the crater.

Using the preferred method of orthogonal mode energy threshold as the stoppage criterion, continuous ablation scan trials were run on a TBC-coated button sample, with intent of exposing a large section of bond coat. As with the CMAS removal described earlier in this chapter, a mechanical shutter closed over areas which had exceeded the threshold for ablation stoppage, preventing additional ablation. The target was translated at a constant velocity of 0.8 mm/s while the ablation laser ran at 20 Hz, using a pulse energy of 20 mJ. These TBC removal scanning trials are shown in Fig. 60

Figure 60: Ablation troughs after scanning LIBS drilling is employed to remove TBC from a coated button sample of relatively constant TBC thickness. The width of the band of exposed bond coat is approximately 0.4 mm.

6.3.3 Scaling with Laser Power

From the drilling tests described in Section 6.3.2, an estimate may be placed on the rate of TBC removal. A single scan from these trials sweeps out an area of approximately 2.0 mm^2, clearing TBC of thickness on the order of 200 microns. The time to clean a line of 5 mm in length at an average laser power of 400 mW was 405 ± 12 seconds. This yields the laser ablation TBC removal rate of 9.88 x 10^{-4} mm^3/s. The Nd:YAG pulsed laser used for this trial has specifications sufficient for efficient single-crater CMAS removal facilitating the PLPS measurements needed for a coating lifetime analysis. A more powerful laser, designed for laser cutting or drilling, would be able to achieve much higher ablation rates. For example, the

Symphotic Tii LS-2147A/2 can provide a 300 mJ pulse at 355 nm, at a repetition rate of 10 Hz. The resultant average power of 3.0 W would yield a TBC removal rate of 7.41 x 10^{-3} mm^3/s. Which corresponds to an area removal rate of 3.70 10^{-2} mm^2/s for a TBC of 200 microns thickness. Table 7 lists some typical pulsed Nd:YAG frequency-tripled lasers. The models shown are from the recent Lotis Tii laser catalog.

Table 7: Typical specifications and pricing for mid-range pulsed Nd:YAG laser.

Model Number	Pulse Energy at 355 nm	Pulse Duration	Repetition Rate	Max Average Power	Price
LS-2134UT	55 mJ	7-8 ns	1-15 Hz	825 mW	$29,400
LS-2137U	160 mJ	6-7 ns	1-10 Hz	1.60 W	$35,500
LS-2137U-UV3	210 mJ	6-7 ns	1-10 Hz	2.10 W	$38,300
LS-2134T	60 mJ	14-16 ns	1-15 Hz	900 mW	$29,250
LS-2145T	90 mJ	14-16 ns	1-10 Hz	900 mW	$32,600
LS-2137/3-20	90 mJ	16-18 ns	1-20 Hz	1.80 W	$42,300
LS-2137/3	120 mJ	16-18 ns	1-10 Hz	1.20 W	$34,900
LS-2147/3-20	140 mJ	16-18 ns	1-10 Hz	1.40 W	$45,900
LS-2147/3	170 mJ	16-18 ns	1-10 Hz	1.70 W	$38,200

Though relatively low-cost, these nanosecond-pulsed lasers have very low average power in comparison to the industrial lasers used for welding and drilling. However, two constraints on the system largely necessitate a pulsed UV laser. The first is that short, high-intensity pulses are necessary to initiate the dielectric breakdown for plasma formation. The second reason is that the discriminating power of the LIBS spectral analysis is tuned to the UV-A absorption bands for the TBC species. A larger nanosecond-pulsed UV laser, or an array of synchronized lasers could be used to provide a higher average power. Care must be taken that the ablation spot does not become too large, so the mechanisms in place to prevent substrate damage remain functional. A high average-power kilo-Hz pulsed laser can achieve an average power on the order of 30 W, while maintaining all other requirements for laser ablation TBC removal.

Conclusion

The optimization efforts for the mobile technology developed by Lake have addressed sources of measurement error or difficulties in data collection, in response to system performance during a field demonstration. Orthogonal modes in place of reference spectra cross-correlation for species identification provides a more consistent and physically meaningful method for ablation control. Operation parameters for the LIBS system were optimized for the even removal of CMAS for single-crater cleaning. The collection efficiency of PLPS measurements has been increased, permitting faster measurements with higher agreement. Stress measurements on thermally cycled factory-condition turbine blades has shown conclusively that the TGO stresses experienced by engine components can exceed the domain of the current life fraction-stress regression correlation. It was shown that the higher stresses were not caused by laser heating, and are physically meaningful. The system has since been demonstrated at a maintenance facility, and was found to perform sufficiently well.

Optical fiber bundles have been integrated into the PLPS methodology, permitting the acquisition of stimulated TGO fluorescence from components within a mounted engine, utilizing a bore-scope device. A fiber bundle composed of 19 fibers of 200 μm diameter, as well as a 790-diameter fiber bundle filled with 30,000 pixels were tested and used for stress measurements. PLPS trials on engine-run turbine blades, along with thermally cycled factory-condition blades and coated button samples demonstrate measurements taken via fiber bundle to be consistent with those taken with a standard PLPS technique. Several fused-silica components were tested as potential waveguides for the borescope-adapted LIBS method. Damage thresholds for step-index silica optical fibers with doped silica cladding were found at a pulse energy of 14 mJ with a 5.22 ns pulse of 355 nm laser. Transmission efficiencies for the different waveguides were

investigated, leading to the conclusion that fused silica rods or hollow tubes are not feasible without a metallic or dielectric coating.

An extensive collection of LIBS spectra for the constituent species of coating systems produced high signal-to-noise ratio reference spectra, improving the distinction of species recognition. In addition, orthogonal modes were developed from the repository of reference spectra to significantly improve species recognition during LIBS-controlled drilling. Based on these orthogonal modes, stop criteria were developed, capable of consistently halting laser ablation during TBC removal. The most promising stop criterion is based on a threshold for the bond coat mode energy, ostensibly due to bond coat interface recognition. A scanning ablation scheme was perfected for CMAS removal, capable of cleaning large areas of TBC for subsequent PLPS measurements. This same scanning technique was adapted for TBC removal by implementing the bond coat mode energy stop criterion. Using this technique, it was possible to place an estimate on the rate of TBC removal as a function of laser power. The Quantel Nd:YAG used in this experiment can remove YSZ topcoat at approximately 9.88×10^{-4} mm^3/s, yielding a correlation of removal rate to laser power of 2.47×10^{-3} $mm^3/W\text{-}s$. Based on this figure, it is possible to speculate on the practicality of laser-ablation for TBC removal by scaling the results to higher power lasers, and performing a cost-benefit analysis.

Future work should focus on completing the fiber-implemented LIBS technique, especially for obtaining the necessary energy density on target for plasma formation. It will need to be determined whether spatially filtered LIBS signal will remain plausible or if a temporal filter must be employed. In addition, more elegant methods for bond coat interface recognition may yield better discrimination power than the current scheme, and physical confirmation will be important for evaluating the accuracy of any such trials. In another arena of concern, successful

PLPS measurements for remaining life analysis of Trent XWB vanes are highly desirable, and an effort should be made to extract chromium fluorescence signal from the intense erbium dopant fluorescence. Measures should be taken to identify regions on the vane where the ratio of erbium fluorescence to chromium fluorescence is minimized, and to implement techniques which will facilitate stress measurements. Finally, with the possibility of application for helicopter blades suffering from CMAS attack, it may be useful to perfect a system for cleaning cooling holes using a rigid or flexible LIBS waveguide to transmit ablation energy.

References

Anglos, D. (2001). Laser-Induced Break-down Spectroscopy in Art and Archaeology. *Applied Spectroscopy*, 186A-205A.

Atkinson, A., Selcuk, A., & Webb, S. J. (2000). Variability of Stress in Alumina Corrosion Layers Formed in Thermal-Barrier Coatings. *Oxidation of Metals, Vol. 54*, 371-384.

Barbini, R., Colao, F., Fantoni, R., Lazic, V., Palucci, A., Capitelli, F., & van der Steen, H. J. (2000). Laser induced breakdown spectroscopy for semi-quantitative elemental analysis in soils and sediments. *Proceedings of EARSeL-SIG-Workshop LIDAR.* Dresden/FRG.

Braue, W. (2009). Environmental stability of the YSZ layer and the YSA/TGO interface of an in-service EB-PVD coated high-pressure turbine blade. *Journal of Material Science,* 1664-1675.

Cha, J., Zhang, J., Gurbani, S., Cheon, G. W., Li, M., & Kang, J. U. (2012). Gene transfection efficacy assessment of human cervical cancer cells using dual-mode fluorescence microscopy. *Optical Society of America*.

Chapter 7: Thermal Barrier Coatings (TBCs). (2007). In S. Bose, *High-Temperature Coatings* (pp. 155-232). Elsevier.

Chatterjee, A. (2000). An introduction to the proper orthogonal decomposition. *Current Science Vol. 78 Special Section: Computational Science*.

Chen, X. (2006). Calcium-magnesium-alumina-silicate (CMAS) delamination mechanisms in EB-PVD thermal barrier coatings. *Surface & Coatings Technology*, 3418-3427.

Christensen, R. J., Lipkin, D. M., & Clarke, D. R. (1996). Nondestructive evaluation of the oxidation stresses through thermal barrier coatings using Cr3+ piezospectroscopy. *Applied Physics Letters*.

Clarke, D. R., Christensen, R. J., & Tolpygo, V. (1997). The evolution of oxidation stresses in zirconia thermal barrier coated superalloy leading to spalling failure. *Surface and Coatings Technology*, 94-95.

Feeny, B. F. (2002). On Proper Orthogonal Co-Ordinates as Indicators of Modal Activity. *Journal of Sound and Vibration*, 805-817.

Galt, S., Sjoberg, M., Quiroga-Teixeiro, M. L., & Hard, S. (2003). Optical breakdown in fused silica and argon gas: application to Nd:YAG laser limiter. *Optical Society of America*.

Gao, L., Zhou, H., Thrall, M. J., Li, F., Yang, Y., Wang, Z., . . . Wong, S. T. (2011). Label-free high-resolution imaging of prostate glands and cavernous nerves using coherent anti-Stokes Raman scattering microscopy. *Optical Society of America*, 915-926.

Gell, M., Sridharan, S., & Wen, M. (2004). Photoluminescence Piezospectroscopy: A Multi-Purpose Quality Control and NDI Technique for Thermal Barrier Coatings. *International Journal of Applied Ceramic Technology*.

Han, S., & Feeny, B. (2003). Application of Proper Orthogonal Decomposition to Structural Vibration Analysis. *Mechanical Systems and Signal Processing*, 989-1001.

Hélie, D., Gouin, S., & Vallée, R. (2013). Assembling an endcap to optical fibers by femtosecond laser welding and milling. *Optical Society of America*.

Hughes, M., Chang, T. P., & Yang, G.-Z. (2013). Fiber bundle endocytoscopy. *Optical Society of America*.

Kamensky, V. A., Scripachev, I. V., Snopain, G. E., & Pushkin, A. A. (1998). High-power As-S glass fiber delivery for pulse YAG:Er laser radiation. *Applied Optics*, 5596-5599.

Kerschen, G., & Golinval, J. C. (2002). Physical Interpretation of the Proper Orthogonal Modes Using the Singular Value Decomposition. *Journal of Sound and Vibration*, 849-865.

Kramer, S., Yang, J., & Levi, C. G. (2006). Thermochemical Interaction of Thermal Barrier Coatings with Molten CaO-MgO-Al2O3-SiO2 (CMAS) Deposits. *Journal of the American Ceramics Society*, 3167-3175.

Kuhn, A., French, P., Hand, D. P., Blewett, I. J., Richmond, M., & Jones, J. D. (2000). Preparation of fiber optics for the delivery of high-energy high-beam-quality Nd:YAG laser pulses. *Applied Optics*.

Lake, J. L. (2012). Thermal Barrier Coating Analysis of Remaining Life and Contaminant Composition. University of Connecticut.

Lentjes, M., Dickmann, K., & Meijer, J. (2005). Controlled laser cleaning of artworks with low resolution LIBS and linear correlation analysis. *ICALEO Congress Proceedings: Laser Microfabrication Conference.*

Liang, Y. C. (2002). Proper Orthogonal Decomposition and its Applications- Part 1: Theory. *Journal of Sound and Vibration*, 527-544.

Lu, Z., Myoung, S.-W., Jung, Y.-G., Balakrishnan, G., Lee, J., & Paik, U. (2013). Thermal Fatigue Behavior of Air-Plasma Sprayed Thermal Barrier Coating with Bond Coat Species in Cyclic Thermal Exposure. *Materials*, 3387-3403.

Majewski, M. S., Kelley, C., Hassan, W., Brindley, W., Jordan, E. H., & Renfro, M. W. (2011). Laser induced breakdown spectroscopy for contamination removal on engine-run thermal barrier coatings. *Surface & Coatings Technology*, 4614-5619.

Majewski, M. S., Kelley, C., Lake, J., Renfro, M. W., Hassan, W., Brindley, W., & Jordan, E. H. (2012). Stress measurements via photoluminescence piezospectroscopy on engine run thermal barrier coatings. *Surface & Coatings Technology*, 2751-2758.

Matsurra, Y., Tsuchiuchi, A., Noguchi, H., & Miyagi, M. (2007). Hollow fiber optics with improved durability for high-peak-power pulses of Q-switched Nd:YAG lasers. *Optical Society of America*.

Matsuura, Y., & Naito, K. (2010). Flexible hollow fiber bundle for infrared thermal imaging. *Optical Society of America*.

Miller, J., Yu, X.-B., Yu, P. K., Cringle, S. J., & Yu, D.-Y. (2011). Development of a fiber-optic laser delivery system capable of delivering 213 and 266 nm pulsed Nd:YAG laser radiation for tissue ablation in a fluid environment. *Optical Society of America*.

Mohri, S., Kasai, T., Abe, Y., Shi, Y.-W., Matsuura, Y., & Miyagi, M. (2002). Optical properties of end-sealed hollow fibers. *Optical Society of America*.

Padture, N. P., Gell, M., & Jordan, E. H. (2002). Thermal Barrier Coatings for Gas-Turbine Engine Applications. *Review: Materials Science*.

Parry, J. P., Shephard, J. D., Thompson, M. J., Taghizadeh, M. R., Jones, J. D., & Hand, D. P. (2007). Optical fiber array for the delivery of high peak-power laser pulses for fluid flow measurements. *Optical Society of America*, 3432-3438.

Pasquini, C., Cortez, J., Silva, L. M., Gonzaga, S., & Gonzaga, F. B. (2007). Laser Induced Breakdown Spectroscopy. *Journal of Brazilian Chemistry Society*, 463-512.

Pollock, T. M., & Tin, S. (2006). Nickel-Based Superalloys for Advanced Turbine Engines: Chemistry, Microstructure and Properties. *Journal of Propulsion and Power*, 361-374.

Rim, C.-S. (2010). The Optical Design of Miniaturized Microscope Objective for CARS Imaging Catheter with Fiber Bundle. *Journal of the Optical Society of Korea*, 424-430.

Selcuk, A., & Atkinson, A. (2002). Analysis of the Cr3+ luminescence spectra from thermally grown oxide in thermal barrier coatings. *Materials Science and Engineering A335*, 147-156.

Sneizewski, J., Le Maoult, Y., & Lours, P. (2008). In Situ Thermal Gradient Controlled Investigation of Spallation-Experimental Design and Preliminary Results. *Material Science Forum Volumes*, 595-598.

Ulrich, R., & Prettl, W. (1973). Planar Leaky Light-Guides and Couplers. *Applied Physics 1*, 55-68.

Vaßen, R., Jarligo, M. O., Steinke, T., Mack, D. E., & Stover, D. (2010). Overview on advanced thermal barrier coatings. *Surface & Coatings Technology*, 938-942.

Wen, M. (2005). Failure Mechanisms and Mechanisms-Based Life Predictions For Electron Beam Physical Vapor Deposition Thermal Barrier Coatings. University of Connecticut.

Wen, M., Jordan, E. H., & Gell, M. (2006). Remaining Life Prediction of Thermal Barrier Coatings Based on Photoluminescence Piezospectroscopy Measurements. *Journal of Engineering for Gas Turbines and Power*.

Wen, M., Jordan, E., & Gell, M. (2006). Analysis of localized damage in EB-PVD/(Ni,Pt)Al thermal barrier coatings. *Surface & Coatings Technology*, 5193-5202.

Xie, L., Sohn, Y., Jordan, E. H., & Gel, M. (2003). The effect of bond coat grit blasting on the durability and thermally grown oxide stress in an electron beam physical vapor deposited thermal barrier coating. *Surface and Coatings Technology*, 57-66.

Yilmaz, O., Miyagi, M., & Matsuura, Y. (2006). Bundled hollow optical fibers for transmission of high-peak-power Q-switched Nd:YAG pulses. *Applied Optics*, 7174-7178.

Zhang, C., & Chen, C. (2011). Failure mechanism of thermal barrier coatings by electron beam physical vapor deposition (EB-PVD) under thermomechanical coupled loads. In *Thermal Barrier Coatings* (pp. 215-241). Woodhead Publishing.

Zhao, H., Yu, F., Bennett, T. D., & Wadley, H. N. (2006). Morphology and thermal conductivity of yttria-stabilized zirconia coatings. *Acta Materialia 54*, 5195-5207.

Zhao, X., & Xiao, P. (2006). Residual stresses in thermal barrier coatings measured by photoluminescence piezospectroscopy and indentation technique. *Surface & Coatings Technology*, 1124-1131.

Zhao, X., & Xiao, P. (2007). Focus effect of photoluminescence piezospectroscopy and its influence on the stress measurement of thermally grown oxide in thermal barrier coatings . *Scripta Materialia*, 683-686.

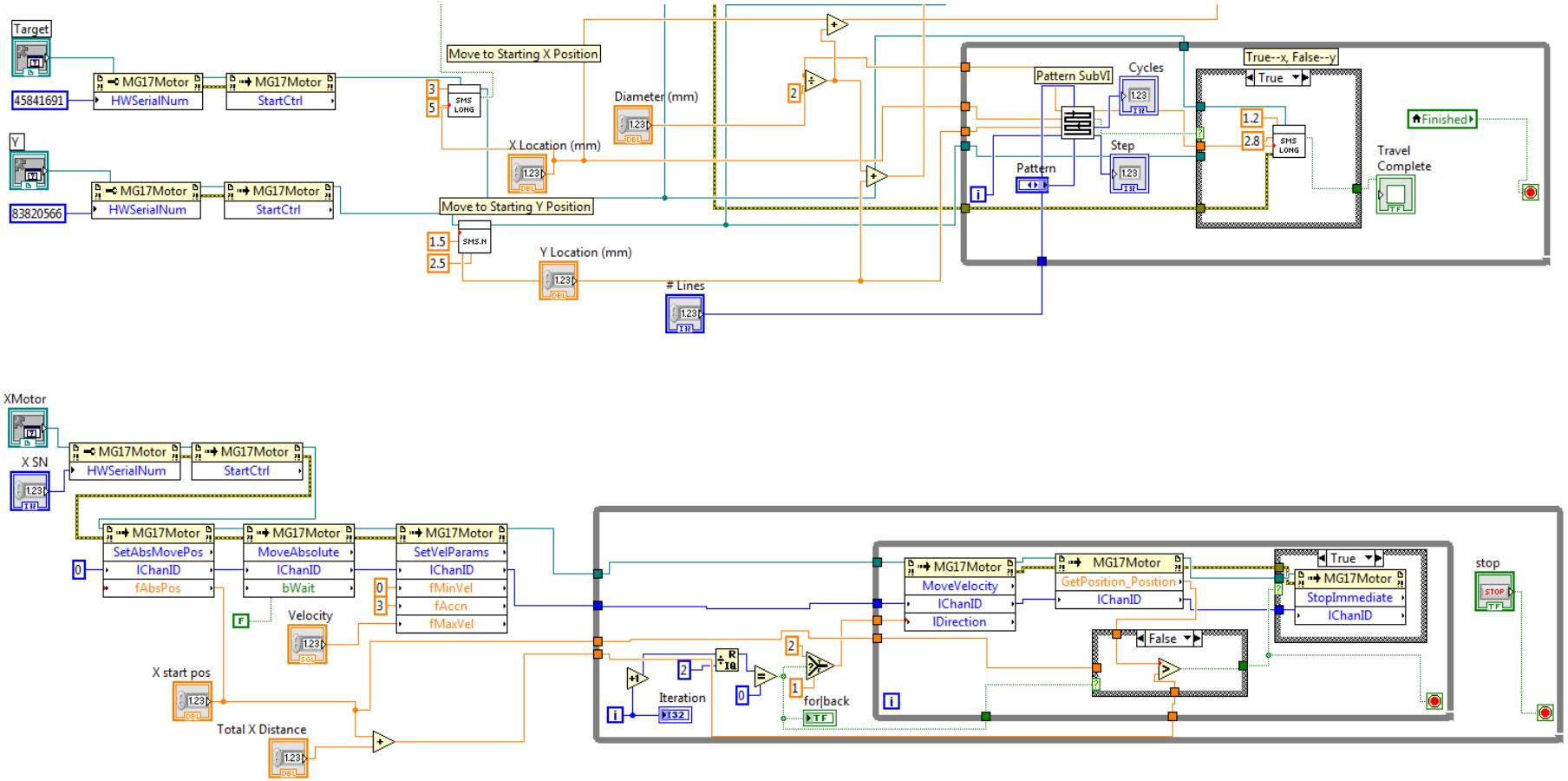
Target
45841691
MG17Motor
HWSerialNum
MG17Motor
StartCtrl
Y
83820566
Move to Starting X Position
Move to Starting Y Position
X Location (mm)
Y Location (mm)
Diameter (mm)
Lines
Pattern SubVI
Cycles
Pattern
Step
True--x, False--y
True
Travel
Complete
Finished
XMotor
X SN
SetAbsMovePos
MoveAbsolute
SetVelParams
IChanID
fAbsPos
bWait
fMinVel
fAccn
fMaxVel
Velocity
X start pos
Total X Distance
Iteration
for|back
MoveVelocity
IDirection
GetPosition_Position
StopImmediate
False
stop

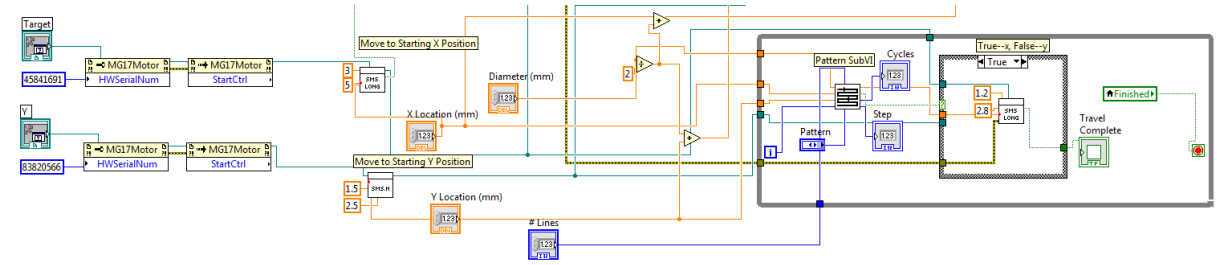
Target
45841691
MG17Motor
HWSerialNum
MG17Motor
StartCtrl
Y
83820566
Move to Starting X Position
Move to Starting Y Position
X Location (mm)
Y Location (mm)
Diameter (mm)
Lines
Pattern SubVI
Cycles
Pattern
Step
True--x, False--y
Travel Complete
Finished

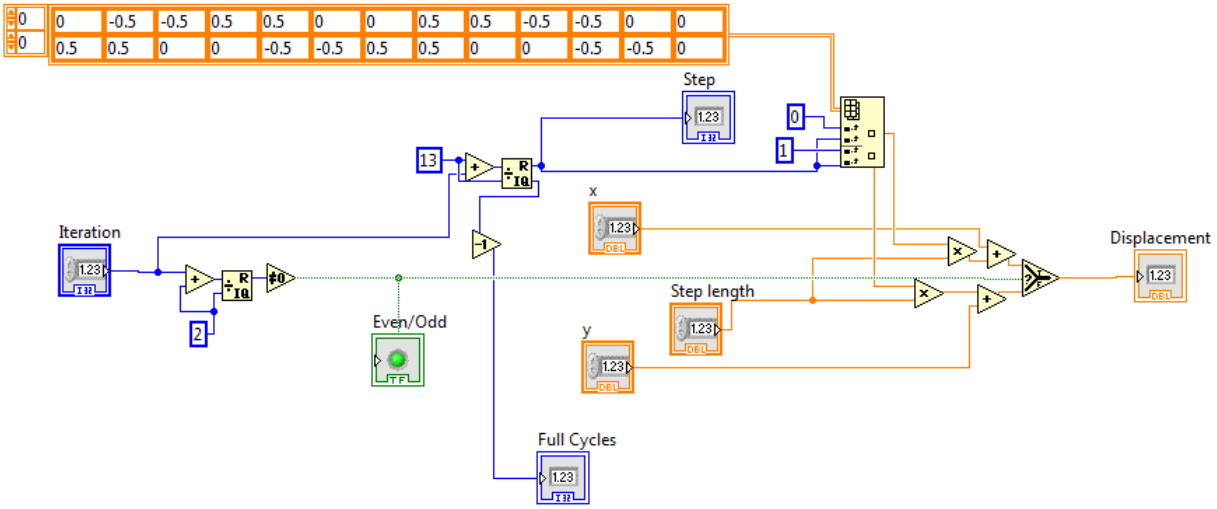
0 0 -0.5 -0.5 0.5 0.5 0 0 0.5 0.5 -0.5 -0.5 0 0
0.5 0.5 0 0 -0.5 -0.5 0.5 0.5 0 0 -0.5 -0.5 0
Step
Iteration
x
Displacement
Step length
Even/Odd
y
Full Cycles

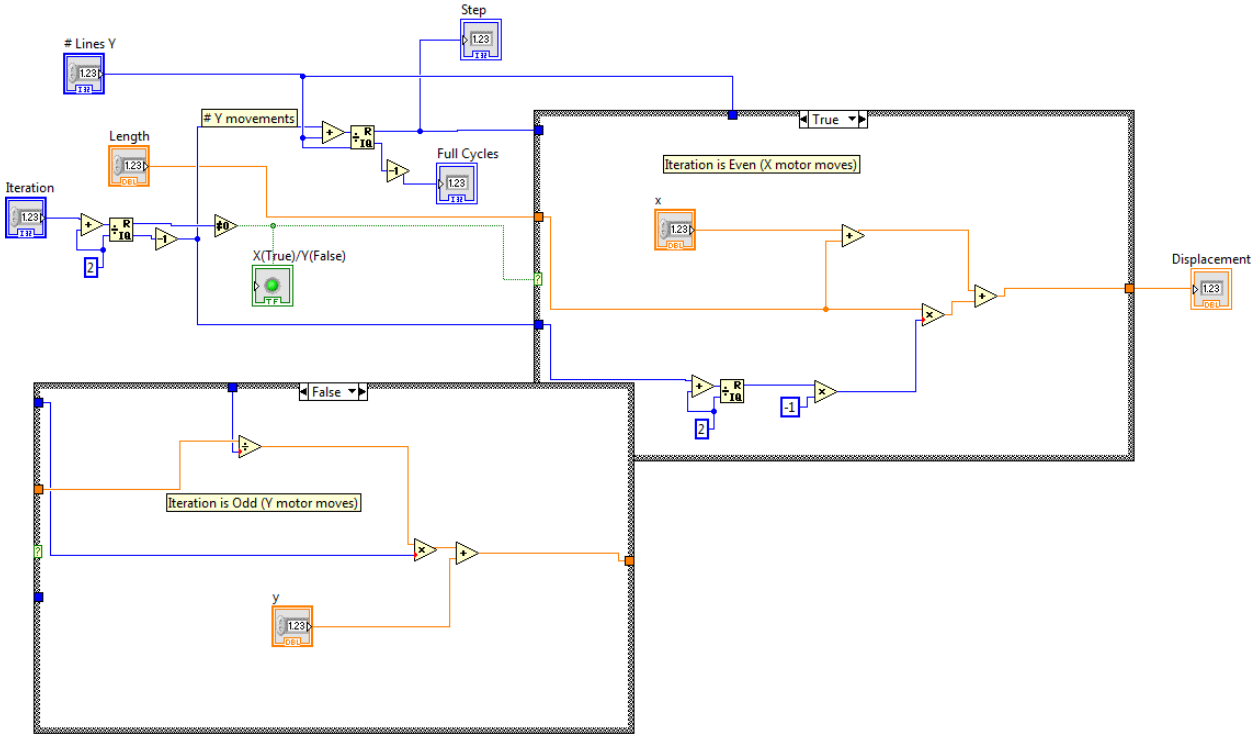
Lines Y
Step
Y movements
Length
Full Cycles
Iteration
X(True)/Y(False)
True
Iteration is Even (X motor moves)
x
Displacement
False
Iteration is Odd (Y motor moves)
y